Springer Theses
Recognizing Outstanding Ph.D. Research

Rasmus Y. Brogaard

Molecular Conformation and Organic Photochemistry

Time-resolved Photoionization Studies

Springer

Springer Theses

Recognizing Outstanding Ph.D. Research

For further volumes:
http://www.springer.com/series/8790

Aims and Scope

The series "Springer Theses" brings together a selection of the very best Ph.D. theses from around the world and across the physical sciences. Nominated and endorsed by two recognized specialists, each published volume has been selected for its scientific excellence and the high impact of its contents for the pertinent field of research. For greater accessibility to non-specialists, the published versions include an extended introduction, as well as a foreword by the student's supervisor explaining the special relevance of the work for the field. As a whole, the series will provide a valuable resource both for newcomers to the research fields described, and for other scientists seeking detailed background information on special questions. Finally, it provides an accredited documentation of the valuable contributions made by today's younger generation of scientists.

Theses are accepted into the series by invited nomination only and must fulfill all of the following criteria

- They must be written in good English.
- The topic should fall within the confines of Chemistry, Physics, Earth Sciences and related interdisciplinary fields such as Materials, Nanoscience, Chemical Engineering, Complex Systems and Biophysics.
- The work reported in the thesis must represent a significant scientific advance.
- If the thesis includes previously published material, permission to reproduce this must be gained from the respective copyright holder.
- They must have been examined and passed during the 12 months prior to nomination.
- Each thesis should include a foreword by the supervisor outlining the significance of its content.
- The theses should have a clearly defined structure including an introduction accessible to scientists not expert in that particular field.

Rasmus Y. Brogaard

Molecular Conformation and Organic Photochemistry

Time-resolved Photoionization Studies

Doctoral Thesis accepted by the
University of Copenhagen, Denmark

Springer

Author
Dr. Rasmus Y. Brogaard
Department of Chemical Engineering
SUNCAT Center for Interface Science and Catalysis
Stanford University
Stanford, CA 94305
USA

Supervisors
Dr. Klaus B. Møller
Department of Chemistry
Technical University of Denmark
Kgs. Lyngby
Denmark

Dr. Theis I. Sølling
Department of Chemistry
University of Copenhagen
Copenhagen
Denmark

ISSN 2190-5053 ISSN 2190-5061 (electronic)
ISBN 978-3-642-29380-1 ISBN 978-3-642-29381-8 (eBook)
DOI 10.1007/978-3-642-29381-8
Springer Heidelberg New York Dordrecht London

Library of Congress Control Number: 2012937644

© Springer-Verlag Berlin Heidelberg 2012
This work is subject to copyright. All rights are reserved by the Publisher, whether the whole or part of the material is concerned, specifically the rights of translation, reprinting, reuse of illustrations, recitation, broadcasting, reproduction on microfilms or in any other physical way, and transmission or information storage and retrieval, electronic adaptation, computer software, or by similar or dissimilar methodology now known or hereafter developed. Exempted from this legal reservation are brief excerpts in connection with reviews or scholarly analysis or material supplied specifically for the purpose of being entered and executed on a computer system, for exclusive use by the purchaser of the work. Duplication of this publication or parts thereof is permitted only under the provisions of the Copyright Law of the Publisher's location, in its current version, and permission for use must always be obtained from Springer. Permissions for use may be obtained through RightsLink at the Copyright Clearance Center. Violations are liable to prosecution under the respective Copyright Law.
The use of general descriptive names, registered names, trademarks, service marks, etc. in this publication does not imply, even in the absence of a specific statement, that such names are exempt from the relevant protective laws and regulations and therefore free for general use.
While the advice and information in this book are believed to be true and accurate at the date of publication, neither the authors nor the editors nor the publisher can accept any legal responsibility for any errors or omissions that may be made. The publisher makes no warranty, express or implied, with respect to the material contained herein.

Printed on acid-free paper

Springer is part of Springer Science+Business Media (www.springer.com)

Parts of this thesis have been published in the following journal articles: **In the thesis itself the papers will be referred to by their Roman numerals**

I *Initial Dynamics of The Norrish Type-I Reaction in Acetone: Probing Wave Packet Motion*
R. Y. Brogaard, T. I. Sølling, and K. B. Møller, *J. Phys. Chem. A* **2011**, *115*, 556.

II *Pseudo-Bimolecular [2+2]cycloaddition Studied by Time-Resolved Photoelectron Spectroscopy*
R. Y. Brogaard, A. E. Boguslavskiy, O. Schalk, G. D. Enright, H. Hopf, V. A. Raev, P. G. Jones, D. L. Thomsen, T. I. Sølling, and A. Stolow, *Chem. Eur. J.* **2011**, *17*, 3922.

III *The Paternò-Büchi Reaction: Importance of Triplet States in The Excited-State Reaction Pathway*
R. Y. Brogaard, O. Schalk, A. E. Boguslavskiy, G. D. Enright, A. Stolow, V. A. Raev, E. Tarcoveanu, H. Hopf, and T. I. Sølling, *Phys. Chem. Chem. Phys*. **2012**, doi:10.1039/C2CP40819H.

IV *Real-Time Probing of Structural Dynamics by Interaction between Chromophores*
R. Y. Brogaard, K. B. Møller, and T. I. Sølling, *J. Phys. Chem. A* **2011**, *115*, 12120.

Outline

Chapter 1 Introduction and motivation of the project in the field of ultrafast photochemical reaction dynamics.
Chapter 2 This chapter introduces central concepts in the description of photochemical reactivity and how it can be probed experimentally using femtosecond time-resolved spectroscopy.
Chapter 3 Review of the time-resolved probing method of photoionization and discussion of the analysis and interpretation of experimental results.
Chapter 4 Introduction of the theoretical framework applied in the present work to simulate time-resolved photoionization signals.
Chapter 5 Presentation of our results from a simulation of ultrafast dynamics in the initial step of the Norrish Type-I reaction in acetone and comparison of the simulated and experimental signals.
Chapter 6 Description of the setups used to conduct femtosecond time-resolved photoelectron spectroscopy and mass spectrometry experiments.
Chapter 7 Results obtained in Ottawa from femtosecond time-resolved photoelectron spectroscopy experiments on a [2+2]cycloaddition between two ethylene units connected to a [2.2]paracyclophane scaffold.
Chapter 8 This chapter discusses experimental results obtained from an investigation of the Paternò-Büchi reaction using the same molecular scaffold and experimental setup as in Chap. 6.
Chapter 9 Illustration of a simple way of probing structural dynamics by interaction between chromophores using time-resolved ion photofragmentation spectroscopy. The experimental results were obtained in Copenhagen.
Chapter 10 The last chapter summarizes the experimental and computational results presented in the thesis and discusses their significance for future research.

Supervisors' Foreword

When dealing with femtoseconds we are dealing with the time scale of molecules. It has been recognized for around two decades that very valuable information on chemical dynamics can be obtained in experimental and theoretical frameworks where the femtosecond time resolution is a key. This thesis digs deeper into the world of femtochemistry from a combined theoretical and experimental perspective. Not from a standard angle with standard methods, but always with a novel perspective on the problem at hand. In gas-phase studies using femtosecond time-resolved spectroscopy one faces two major limitations: Firstly, the reactions under study have to be unimolecular and, secondly, there is not a one-to-one correspondence between signal and structure. The thesis seeks to address both issues and it was found that one can gain insight into bimolecular reactions, or at least pseudo bimolecular reactions, by placing the reacting units on a molecular scaffold right in a position where they can react with each other. This circumvents any issues related to the directionality of the internal energy—when no prior change of conformation is needed for the reaction to occur the chemical bonds will start to form more or less simultaneously after the excitation and as a result the bond forming process can be studied in its own right without the complication of preceding conformational processes where the reactive conformation only is visited on a statistical basis. There is no doubt that this way of performing femtosecond time-resolved studies of bimolecular reactions will inspire further work not only within the field of femtochemistry but also it will be an integral part of future studies of ultrafast dynamics in biological systems such as peptides and DNA where conformational dynamics is key.

Quite apart from the investigation of the dynamics associated with bond formation in bimolecular reactions the conformational dynamics of radical cations have been addressed. Often it is ambiguous whether pump-probe studies with ionizing probe actually address the dynamics of neutral or ionic systems but we have found the ideal system where a well-defined population of excited-state radical cations is formed by resonant ionization through an intermediate Rydberg state. The population of radical cations moves in a synchronous motion. The idea is that it is initiated by the ionization in one end of the molecule to induce an

interaction with the other end. Such a setup opens the possibility of an advanced investigation of the torsional dynamics that is specifically initiated by the interaction between two select sites in a molecule—something that can prove very valuable, not only in its own right, but also in cases where pseudo bimolecular arrangements of the reactants are not possible. Additionally, insights such as this probably will call for a revision of previous experiments using time-resolved photoionization, given that this thesis shows that it is quite feasible to form ions already with the pump to induce interesting dynamical features. We really enjoyed reading the thesis and we are sure it will inspire a broad spectrum of scientists. We strongly encourage everybody to take a good look at it!

Kgs. Lyngby, Denmark — Klaus B. Møller
Copenhagen, Denmark — Theis I. Sølling

Preface

Give a man a fish and he will eat for a day.
Teach a man to fish and he will eat for a lifetime.
Chinese Proverb

This thesis has been submitted to the Faculty of Science, University of Copenhagen, as a partial fulfillment of the requirements to obtain the PhD degree. The work presented here was carried out at the Department of Chemistry in the years 2008–2011 under the joint supervision of Klaus B. Møller, Technical University of Denmark, and Theis I. Sølling, University of Copenhagen.

Acknowledgements

I have by now spent more than five years working in the field of ultrafast photochemical reaction dynamics. Thanks to a fruitful collaboration between my supervisors I have been fortunate to be able to make efforts and experiences in both theoretical and experimental directions. I am sincerely grateful to Theis and Klaus for their commitment and for giving me opportunities and support that I believe few PhD students will encounter.

During my PhD studies I was fortunate to have the opportunity to stay 11 months in the Molecular Photonics Group lead by Albert Stolow at the Steacie Institute for Molecular Sciences in Ottawa. I will always remember this as a scientific experience that compares to nothing. I am sincerely grateful to Albert for letting me join his lab and the rest of the group for being friendly and inspiring colleagues. Albert strongly encouraged me to acquire some hands-on laser experience, which resulted in a project of rebuilding a picosecond amplifier system. After many late and frustrating hours in the lab the project succeeded. For that I owe Rune Lausten a big thank for teaching me the "do's and dont's" of lasers and

nonlinear optics and for good times in the lab. Whereas the project did not result in any publications, it more importantly gave me experience that has proven invaluable for the rest of my lab work. Thanks to Michael Schuurman from the Theory group at Steacie I got the opportunity to perform quantum dynamics simulations while in Ottawa and I would like to thank Michael for patiently answering all my questions, benefiting little from it himself. Oliver Schalk and Andrey Boguslavskiy tirelessly worked with me in the basement at Steacie, even on late Fridays getting difficult experiments to work. I sincerely appreciate their commitment and had a lot of fun with Oliver and Andrey in the lab.

Special thanks go to Henning Hopf and his group at University of Braunschweig, Germany, for a fruitful collaboration involving the paracyclophanes. Their impressive synthetic skills were crucial for the success of our experiments.

As a PhD student you quickly realize that experiments rarely work the first time, and the experiments planned in collaboration with Søren Keiding, Aarhus University, was not an exception. Limited time excluded a second try during my project, but I am grateful to Søren and Jan Thøgersen for their hospitality, and I hope for the experiment and the collaboration to be successful. I thank Christer Bisgaard for kindly sharing his experiences and giving great advice on the experimental setup in Copenhagen. During many years Steen Hammerum has had a significant influence on my education at the Department of Chemistry. As few scientists possess the same lucidity as Steen, our fierce scientific discussions have without doubt made me a better chemist, which I am truly grateful for. A major thank to Anne Stephansen for volunteering to proofread the thesis.

Last, but certainly not least, I would like to thank Martin Rosenberg, Thomas Kuhlman and all of you from "Massekælderen" who over the years have contributed to a thriving scientific and social environment that I have enjoyed ever since I started as a bachelor student.

Collegium Domus Regiæ, October 26, 2011 Rasmus Y. Brogaard

Contents

Abbreviations

[X,Y′]	A pump–probe process involving *X* photons of the pump and *Y* photons of the probe pulse
AIMS	Ab Initio Multiple Spawning
amu	Atomic mass unit
CI	Conical intersection
CW	Continuous wave
DAS	Decay-associated spectrum
DBP	1,3-dibromopropane
DMIPA	*N*,*N*-dimethylisopropylamine
fs	Femtosecond(s)
fwhm	Full-width at half maximum
GEM-V	Pseudo-gem-divinyl[2.2]paracyclophane
GEM-VF	Pseudo-gem-vinylformyl[2.2]paracyclophane
HF	Hartree-Fock
HOMO	Highest occupied molecular orbital
IC	Internal conversion
IFG	Independent first generation
IP	Ionization potential
ISC	Intersystem crossing
IVR	Intramolecular vibrational energy redistribution
LUMO	Lowest unoccupied molecular orbital
MCP	Microchannel plate
MECI	Minimum-energy CI
ns	Nanosecond(s)
PARA-V	Pseudo-para-divinyl[2.2]paracyclophane
PARA-VF	Pseudo-para-vinylformyl[2.2]paracyclophane
PB	Paternò-Büchi
PES	Potential energy surface
ps	Picosecond(s)
QMD	Quantum molecular dynamics
REMPI	Resonance enhanced multiphoton ionization

SA*N*-CAS(*m*,*n*)	SA-CASSCF calculation in which *N* states are averaged using an active space of *m* electrons in *n* orbitals
SA-CASSCF	State-averaged complete active space self-consistent field
TBF	Trajectory basis function
TOF	Time of flight
TRMS	Time-resolved mass spectrometry
TRPES	Time-resolved photoelectron spectroscopy
TRPF	Time-resolved ion photofragmentation

Part I
Ultrafast Photochemistry

Chapter 1
Introduction

The key difference between photochemistry and thermal chemistry is that the former is initiated in an excited electronic state. The topographies of the excited-state potential energy surfaces (PESs) are often fundamentally different from that of the ground state. This property makes photochemical reactions very interesting from the point of view of the preparative chemist, since it means that products not (easily) available from thermal reactions can be made using photochemistry (see e.g. Refs. [1–6]). With sunlight being an abundant source of energy, but also potentially dangerous to many organisms, evolution of nature tailors the photochemical reactivity to make the best out of every photon. A greater understanding of the mechanisms of photochemical reactivity opens possibilities for making new compounds, but also for protecting existing ones from sunlight damage.

Whereas the fundamentals of ground state thermal reactions are by now quite well understood, the situation is different for photochemical reactions where the conceptual framework is still being developed. The advent of ultrafast lasers played a crucial role in this development, since it paved the way for experiments with a time-resolution high enough to follow nuclear motion. Ahmed Zewail was a pioneer in these fs time-resolved spectroscopy experiments and was awarded The Nobel Prize in Chemistry 1999 [7]. Since then, the field has developed rapidly and numerous studies of ultrafast phenomena in physics, chemistry and biology have been conducted. This thesis deals with ultrafast photodynamics of organic molecules and the following section serves to motivate and define the project within that area.

1.1 Motivation: Molecular Conformation and Photochemistry

Every photochemical reaction starts by the same event: absorption of light by a chromophore in the molecule. Understanding ultrafast photochemistry is to understand the charge and energy flow through the molecule from this initial event to the occurrence of bond formation, dissociation or isomerisation resulting in the products.

R. Y. Brogaard, *Molecular Conformation and Organic Photochemistry*,
Springer Theses, DOI: 10.1007/978-3-642-29381-8_1,
© Springer-Verlag Berlin Heidelberg 2012

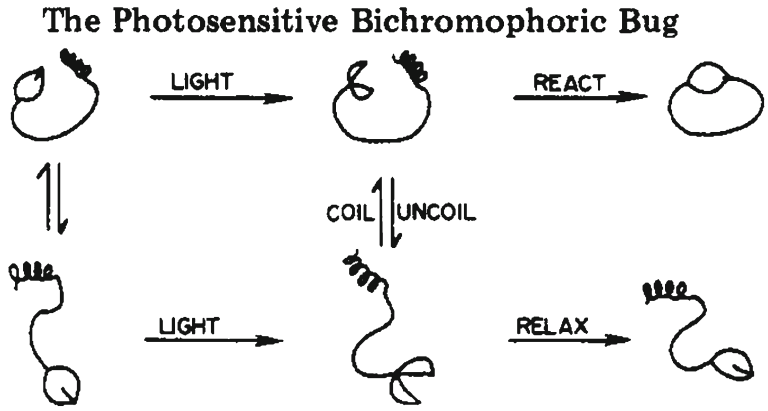

Fig. 1.1 The dynamics of the bichromophoric bug as introduced by Wagner. Extracted from scheme II of Ref. [8]

Within that scope the efforts in this project have been focused on large-amplitude nuclear motions and molecular conformation changes with the aim of understanding how and to what extent they affect ultrafast dynamics and reactivity in organic photochemistry. The aim of the project is to put down yet another stone or two on the path towards the ultimate goal of achieving a set of rules of thumb of what photochemical reactivity (if any) to expect from a given case based on molecular structure and electronic character of the excited state. Our experimental approach for shedding light on these issues is to investigate the species in a molecular beam in which they are isolated from external perturbations such as that of a solvent. We study the dynamics of the isolated species using fs time-resolved photoionization (see Chap. 3) as a probing scheme.

Already early on Wagner appreciated that the interplay between conformational dynamics and reactivity is fundamentally different in chemistry of excited states as compared to the ground state [8]

> Rates at which electronically excited states react chemically are often as fast as rates at which they undergo conformational change. The competition between these quite different processes produces several intriguing effects that are not possible in ground-state chemistry.

Although by now this statement should probably be refined in the sense that excited-state reactions are (most often) at least as fast as conformational changes, it is still very relevant to current research in photochemistry in general and to this project in particular. Wagner attacked the problem in a fashion very similar to the approach of this project (Chap. 9) and earlier work from Femtolab Copenhagen [9, 10] by studying bifunctional molecules in which two chromophores are separated by an alkyl chain. He described these molecules by the very appealing analogy of the "photosensitive bichromophoric bug" shown in Fig. 1.1. When struck by light, the bug's head will attempt to eat its tail. He conducted research on several such bugs

using different chromophores as heads and tails thereby answering questions about the interplay between conformation and excitation energy transfer [11, 12].

Whereas the bugs were mainly used to study the interaction between the chromophores, a vast amount of research is focused on the opposite problem of using a known interaction to probe molecular conformation. Probably the most well-known example of this strategy is the use of Förster resonance energy transfer between chromophores incorporated in biomolecules such as DNA strands as a probe of the molecular conformation [13]. Among the ultrafast spectroscopies two-dimensional infrared (2D-IR) experiments [14, 15] are one of the most general ways of probing structural dynamics using interaction between chromophores. Being conceptually very similar to 2D-NMR spectroscopy of nuclear spin transitions, [16, 17] a 2D-IR experiment is sensitive to (the time-evolution of) couplings between IR chromophores. Since the magnitude of these couplings depend on the distance between and relative orientation of the chromophores, a 2D-IR experiment can provide information about changes in molecular structure occurring on an ultrashort time scale. While 2D-IR experiments are quite involved, we have in this project conducted a much simpler, although not as general, experiment using the interaction between chromophores for real-time probing of ultrafast conformational changes in 1,3-dibromopropane.

References

1. Gilbert, A., Baggott, J.: Essentials of Molecular Photochemistry. Blackwell Scientific Publications, Oxford (1991)
2. Horspool, W.M., Song, P.-S. (eds.): CRC Handbook of Organic Photochemistry and Photobiology. CRC Press, Boca Raton (1995)
3. Bach, T.: Synthesis **5**, 683–703 (1998)
4. Abe, M.: J. Chin. Chem. Soc. **55**, 479–486 (2008)
5. Hoffmann, N.: Chem. Rev. **108**, 1052–1103 (2008)
6. Turro, N.J., Ramamurthy, V.J.C.: Modern Molecular Photochemistry of Organic Molecules. University Science Books, Scaiano (2010)
7. Zewail, A.H.: Angew. Chem., Int. Ed. **39**, 2586–2631 (2000)
8. Wagner, P.J.: Acc. Chem. Res. **16**, 461–467 (1983)
9. Brogaard, R.Y., Sølling, T.I.: J. Mol. Struct. THEOCHEM **811**, 117–124 (2007)
10. Rosenberg, M., Sølling, T.I.: Chem. Phys. Lett. **484**, 113–118 (2010)
11. Wagner, P.J.: Klán, P.: J. Am. Chem. Soc. **121**, 9626–9635 (1999)
12. Vrbka, L., Klán, P., Kríz, Z., Koca, J., Wagner, P.J.: J. Phys. Chem. A **107**, 3404–3413 (2003)
13. Lakowicz, J.R.: Principles of Fluorescence Spectroscopy, 3rd edn. Klyuwer Academix, Dordrecht (2006)
14. Tokmakoff, A., Fayer, M.D.: Acc. Chem. Res. **28**, 437–445 (1995)
15. Mukamel, S.: Annu. Rev. Phys. Chem. **51**, 691–729 (2000)
16. Wüthrich, K.: NMR of Proteins and Nucleic Acids. Wiley, New York (1986)
17. Ernst, R.R., Bodenhausen, G., Wokaun, A.: Principles of Nuclear Magnetic Resonance in One and Two Dimensions. Clarendon Press, Oxford (1987)

Chapter 2
Aspects and Investigation of Photochemical Dynamics

This chapter starts by reviewing concepts that form a versatile means of describing nuclear motion and electronic structure changes during a photochemical reaction. This is followed by an introduction of a framework capable of describing how such ultrafast photodynamics can be probed experimentally. Rather than extensively reproducing formulas [1], the intention is to highlight and qualitatively discuss selected issues relevant to this project. As such, this chapter serves as a reference for the rest of the thesis.

2.1 Photochemical Reaction Mechanisms

As of yet, the amount of literature on mechanistic photochemistry in general and ultrafast dynamics in particular is enormous. Some well-written examples can be found in Refs. [2–8] and this section is intended to be an extract of those works. Unless otherwise stated only singlet electronic states are dealt with in the following.

2.1.1 The Photochemical Funnel

In 1935 Eyring [9], Evans and Polanyi [10] clarified the nature of the transition state and defined the reaction path of a ground state (thermal) chemical reaction. Today the basic mechanistic concepts are familiar to any chemist: being a first-order saddle point on the ground state PES, the transition state is the maximum along a single well-defined (although potentially complex) reaction coordinate connecting the reactants and products as local minima on the PES.

In photochemical reactions the picture is not as clear: although excited-state product formation has been observed [11, 12], most often the chemical transformation occurs in structures for which an excited-state PES is energetically close to or

R. Y. Brogaard, *Molecular Conformation and Organic Photochemistry*,
Springer Theses, DOI: 10.1007/978-3-642-29381-8_2,
© Springer-Verlag Berlin Heidelberg 2012

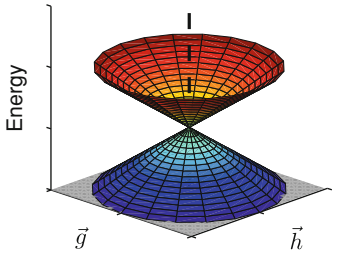

Fig. 2.1 Sketch displaying two PESs against the gradient difference ($\vec{g}$) and derivative coupling ($\vec{h}$) nuclear displacement coordinates spanning the *branching space* (*gray*) that defines a conical intersection. These coordinates lift the degeneracy of the surfaces linearly, while it is maintained in the *seam space* consisting of the nuclear displacement coordinates orthogonal to the branching space (represented by the *dashed line* through the cone)

degenerate with the ground state PES [13, 14]. The most common type of intersection of PESs is the conical intersection (CI), which is often called a photochemical 'funnel' [8, 15], through which reactions can happen. As such, CIs play the same decisive role for the mechanism in photochemical reactions as transition states do in ground state reactions; the first direct experimental support of this statement was recently obtained by Polli et al. [16] The intersection is named conical because the intersecting PESs form a double cone when displayed against the two *branching space* coordinates, called the *gradient difference* ($\vec{g}$) and the *derivative coupling* ($\vec{h}$), as shown in Fig. 2.1. Mathematically, the coordinates are defined as [13]

$$\vec{g} = \frac{\partial(E_2 - E_1)}{\partial \mathbf{R}} \qquad \vec{h} = \langle \phi_1 | \frac{\partial \hat{H}}{\partial \mathbf{R}} | \phi_2 \rangle \tag{2.1}$$

in which $\mathbf{R}$ represents the nuclear coordinates, E_1 and E_2 are the PESs of the $|\phi_1\rangle$ and $|\phi_2\rangle$ states, respectively, and $\hat{H}$ is the Hamilton operator. This illustrates a fundamental difference between a CI and a ground state transition state in terms of the 'reaction coordinate space'. At a CI this space is spanned by the two branching space coordinates rather than the single reaction coordinate defining the ground state reaction. As a consequence, while passage through a transition state in the ground state leads to a single product, passage through a CI can lead to two or more products depending on the number of accessible valleys on the ground state PES [13]. The reaction paths taken are determined by the topography of the PESs at the CI [14, 17–19] as well as the velocities of the nuclei along $\vec{g}$ and $\vec{h}$, as discussed below.

Note that while the branching space coordinates lift the degeneracy of the PESs linearly, it is maintained in the rest of the nuclear displacement coordinates (at least to first order). Thus, there will be another CI at a structure slightly displaced along any of the latter coordinates, called the *seam space*. In a nonlinear molecule containing N atoms the dimension of the seam will be $3N - 6 - 2 = 3N - 8$, which means that in a three-atom nonlinear molecule the seam is a line. This clearly shows that,

already for small molecules, there is another increase in complexity as compared to the ground state reaction with one well-defined transition state: the photochemical reaction can occur through an infinite number of 'transition states' along this line. This complexity is reduced when one considers the lowest-energy structure within the seam, the minimum-energy CI (MECI): analogously to the minimum-energy path in the ground state, one might think that in a photochemical reaction the molecule follows a minimum-energy path in the excited state between the Franck–Condon structure and the MECI. While this is an appealing and intuitively simple picture, it is not always capturing the most important pathway leading to the photochemical reactivity. Therefore it is in some cases necessary to embrace the complexity and take into account a whole range of CIs [20].

2.1.2 Non-Adiabatic Dynamics

The reason for the importance of CIs and for their naming as *funnels* is that internal conversion (IC), nonradiative transition from one electronic state to another of the same spin multiplicity, is extremely efficient at a CI. This means that the process is very competitive towards other (non-reactive) decay channels such as electronic transitions involving a change of spin multiplicity or emission of a photon.

Another way of stating that the rate of nonradiative transition is high is that the coupling between the electronic states is large. Since it is important to appreciate why this is so, the following serves to remind the reader of the origin of the coupling by discussing the scenario sketched in Fig. 2.2. When PESs are well separated, the coupling between the movement of the nuclei and the electrons can be neglected and their interaction assumed adiabatic. In other words, the electrons are assumed to move infinitely fast, instantaneously adapting to the electric field from the nuclei. But when the transition frequency corresponding to the energy difference between the PESs becomes comparable to the frequency of the changing electric field from the moving nuclei, the electrons can no longer keep up. Their interaction with the nuclei is now non-adiabatic: nuclear movement can induce electronic transitions, converting kinetic into potential energy or vice versa. This nonradiative transition occurs on the timescale of the nuclear motion and is therefore ultrafast. Because it is a consequence of a non-adiabatic interaction between the nuclei and the electrons, such a transition is classified as non-adiabatic and the effect mediating it is termed non-adiabatic coupling.

In a quantum mechanical description, it is the nuclear kinetic energy operator that is responsible for the coupling between two adiabatic states. Therefore, the non-adiabatic coupling operator [21] that determines the transition probability between the states includes the derivatives with respect to nuclear position of both the electronic and nuclear part of the wave function. The former derivative is a measure of the extent of electronic character change when the nuclei are moved, from which it can be appreciated that in regions of high non-adiabatic coupling, the electronic character depends heavily on nuclear displacement. Therefore the coupling

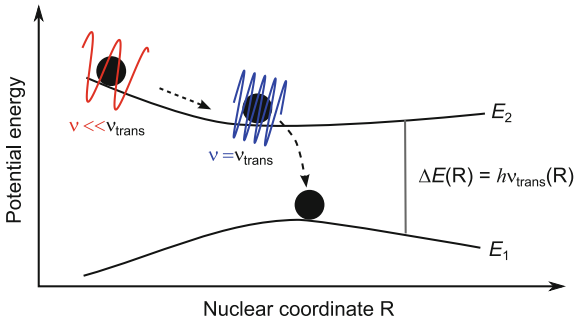

Fig. 2.2 Sketch illustrating the phenomenon of non-adiabatic dynamics. When the PESs E_1 and E_2 are far apart, the interaction between the electrons and nuclei is adiabatic. But when the nuclei have gained speed and encounter a region where the PESs are close, the rate of change of the electric field from the nuclei is comparable to the transition frequency ν_{trans} between the PESs. This means that the interaction between nuclei and electrons is non-adiabatic: nuclear motion can induce a nonradiative electronic transition

diverges to infinity at a CI but more importantly remains large in the vicinity of the intersection. This means that IC is efficient in all molecular structures within that vicinity. Whether a structure can be considered in 'the vicinity' depends not only on the static PESs but also on the velocity of the nuclei, when the molecule passes by the CI. Thus, the CI is a convenient concept of a reaction funnel in the description of photochemistry, but in reality the funnel also includes structures in the surroundings of the CI. In short, the (minimum-energy) CI should not be considered the holy grale of photochemistry: if at any time the speed of the nuclei causes their electric field to change at a rate comparable to the transition frequency between the PESs, non-adiabatic dynamics will occur (and have just the same potential for leading to photochemical reactions as CIs do). In fact, in diatomic molecules the PESs of two states of the same symmetry cannot intersect [22], but non-adiabatic dynamics can still happen in regions where they come close, called avoided crossings. Even in polyatomic molecules avoided crossings can occur, but they are not as frequent as CIs [23]. This can be appreciated by considering the cone shown in Fig. 2.1 and making a cut that does not go through the center of the cone. In this cut the PESs will exhibit what looks like an avoided crossing, but does not classify as a *true* avoided crossing, since in the latter case there is not a CI nearby.

The photodissociation of NaI investigated by Zewail and coworkers is a classical example of non-adiabatic dynamics in general and electronic transition at an avoided crossing in particular [24–26]. The PESs of the ground and first excited states are displayed in Fig. 2.3: as can be seen, there is an avoided crossing between the PESs near an internuclear distance of 7 Å. In this region the electronic character of the states–ionic or covalent bonding–changes dramatically as a function of internuclear distance, and the experiment was able to probe the non-adiabatic dynamics of the photodissociation following electronic transition between the first excited state and the ground state [24, 25].

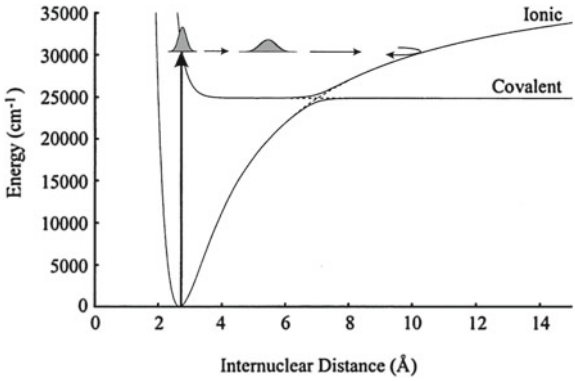

Fig. 2.3 The PESs of the ground and first excited states of NaI. Near the avoided crossing around 7 Å the electronic character of the states–ionic or covalent bonding–is heavily dependent on the internuclear distance. When this region of the PESs is encountered non-adiabatic coupling induces an electronic transition followed by photodissociation. Figure 1 in Ref. [26]

2.1.3 Intersystem Crossing

This chapter is focused on excited singlet states, since these are optically active and IC between such states is often much faster than intersystem crossing (ISC); the electronic transition between states of different spin multiplicity. The reason is that whereas IC is induced by the non-adiabatic coupling, it is (generally) the interaction between the spin and the orbital angular moment of the electrons, the spin-orbit coupling, that induce ISC. In many organic molecules not containing heavy atoms this coupling is weak, corresponding to a low rate of ISC compared to IC. But through a series of studies El-Sayed [27–29] discovered that in cases where the transition occurs from a (n, π^*) to a (π, π^*) state or vice versa, the rate is significantly increased. These transitions are often observed in carbonyl compounds, and this thesis will present experiments on such a compound (Chap. 8) in which ISC even outcompetes IC to the ground state. Readers interested in a thorough review of the physics of ISC are referred to the discussion by Turro et al. (pp 146–156, Chapter 3 in Ref. [8]).

2.1.4 Ultrafast Reactivity

The fact that ultrafast reactivity is closely linked to non-adiabatic dynamics can be appreciated by considering that not only the change of electronic character, but also the velocity of the nuclei determines the magnitude of the non-adiabatic coupling and thereby the probability of electronic transition. Although it is not the complete picture, some intuition can be gained from the Landau–Zener model (see Ref. [30] for Zener's original paper) of radiationless transitions; Desouter-Lecomte and Lorquet derived the following one-dimensional expression for the transition probability between two adiabatic electronic states I and J [31]

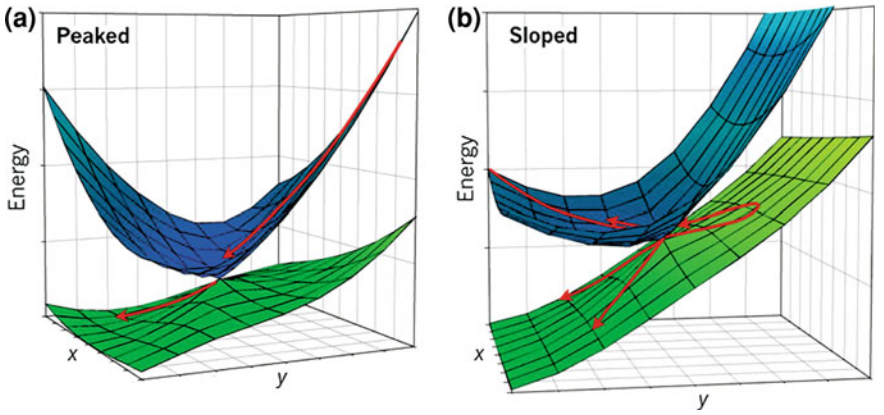

Fig. 2.4 Illustration of the course of non-adiabatic dynamics at two different types of CIs, classified according to their topography in the branching space (x, y). **a** the nuclear trajectories are directed toward the CI, resulting in a very efficient electronic transition. **b** the net rate of electronic transition is decreased due to an increased probability of nuclear trajectories returning from the lower to the upper PES, as illustrated by the upper *red arrow*. Figure 1 in Ref. [19]

$$P_{IJ} = \exp[-(\pi/4)\xi] \qquad \xi = \frac{\Delta E(\vec{q})}{\hbar|\dot{\vec{q}}||\vec{\lambda}_{IJ}(\vec{q})|} \tag{2.2}$$

where ξ is called the Massey parameter. ΔE is the energy difference between the PESs of the two states, the overdot indicates the time derivative and $\vec{q}$ is a nuclear displacement vector parallel to $\vec{\lambda}_{IJ}$, the non-adiabatic coupling between the states

$$\vec{\lambda}_{IJ} = \langle \phi_I | \frac{\partial}{\partial \vec{q}} | \phi_J \rangle \tag{2.3}$$

which is parallel to the derivative coupling $\vec{h}$ [13]. In the framework of Eq. (2.2) the transition probability increases with decreasing energy difference and is one at a CI. Importantly the transition probability also depends on the product between the speed along $\vec{q}$ and the magnitude of the non-adiabatic coupling. Therefore the largest transition probability is obtained if the nuclei move parallel to $\vec{h}$. Considering the case of a molecule approaching a CI this means that not only should the speed of the nuclei be large, the velocity should also have a component along $\vec{h}$ for a transition to occur. The larger the magnitude of this component, the greater the probability of the transition. The role of the CI as a funnel in a photochemical reaction can now be further elaborated. The CI acts as a filter in the position-momentum phase space: the magnitude and direction of $\vec{\lambda}_{IJ}$ determines the velocity distribution of events leading to electronic transition and thereby photochemical reaction. But the magnitude of $\vec{\lambda}_{IJ}$ generally increases with decreasing energy difference, why movement along the gradient difference $\vec{g}$ will also influence the transition probability (although this is not contained in the one-dimensional Landau–Zener model). If, as shown in Fig. 2.4a,

the topography of the PESs at the CI directs the molecule to that favorable region of the phase space, the transition probability is very high or in other words the electronic transition is ultrafast: within a single vibrational period [32]. Such a CI topography is classified as *peaked* [19]. On the other hand, if the topography is such that the center axis of the CI is tilted, Fig. 2.4b, the CI is classified as *sloped* [19]. The net rate of transition is expected to be decreased at a sloped CI, because of an increased probability of nuclear trajectories crossing back from the lower to the upper PES. Whereas the transition probability at a CI increases with the speed along the branching space coordinates, experimental results obtained by Lee et al. [33] lead them to suggest that increased speed along the seam space coordinates can in fact decrease the transition probability at a sloped CI. Hence, the rate of IC at a sloped CI is governed by the relative speeds of the nuclei along the branching and seam space coordinates, respectively.

Summing up the above in a less rigorous way, very efficient electronic transitions are mediated by passage through (the vicinity of) a CI when specific nuclear degrees of freedom are activated. Because of the high efficiency ultrafast reactivity cannot be described by a kinetics model that is inherently statistical (although often this is actually what is done when experimental data is fitted!). This places ultrafast photochemical reactivity in sharp contrast to a thermal reaction in the ground state in which the probability of passing through the transition state is low, making ground state reactions well described by kinetic models such as Eyring, Evans and Polanyis transition state theory mentioned above. The non-statistical nature of ultrafast photochemical processes is what makes them so exciting, and in the quest to understand how the absorbed photon energy is distributed among electrons and nuclei, much can be learned about fundamental chemical problems.

2.2 Probing Ultrafast Dynamics: The Pump–Probe Principle

When designing an experimental setup for investigating ultrafast dynamics of chemical transformations the experimentalist has to fulfill two requisites: an ultrashort probe with a duration of fs and a way to clock it to a trigger with the same time-resolution. Presently, there exist several schemes that comply to these requirements. Common to all of them is the pump–probe principle in which an ultrashort optical pulse, the pump, initiates a chemical change in the sample. A well-defined time-delay after that event an ultrashort probe measures a given property of the sample. By recording this property at a series of delays, time-dependent information about the initiated dynamics is obtained. Depending on the question that the experiment is designed to answer, different probes are used. Using ultrashort X-ray and electron pulses direct structural information can be obtained from diffraction patterns [34, 35], whereas optical probe pulses provide spectroscopic information. Here we will focus on the use of the latter in the field of ultrafast time-resolved spectroscopy. More specifically, unless otherwise stated, experiments involving absorption of one photon of the pump and one photon of the probe pulse are considered.

2.2.1 Coherence

The fundamental difference between time-resolved and steady state spectroscopy stems from the characteristics of the lasers used. From the Fourier relationship between the time and frequency domain it becomes clear that the infinite duration of the continuous wave (CW) lasers used in steady state spectroscopy, corresponds to a monochromatic wavelength spectrum. In time-resolved spectroscopy the situation is different: a finite (ultrashort) pulse duration in the time domain corresponds to a finite bandwidth in the frequency domain. It is important to realize that a finite spectral bandwidth in itself does not lead to a finite duration in the time domain: light from the sun is not pulsed despite the large bandwidth of frequencies emitted. The reason is that the frequencies from the sun are emitted at random instances in time. Another way of stating this is that the phases of the spectral components are not synchronized. The role of phase relationship can be illustrated with a simple example.

Considering the transversal modes of a laser cavity, there is (for most laser media) a set of modes with different frequencies that experience a gain that is greater than the cavity losses. Thus, these modes can exist simultaneously in the cavity and it is therefore instructive to consider the electric field generated by a superposition of these modes. For simplicity we assume the modes to be linearly polarized in the same direction so that a scalar expression of the modes is appropriate

$$e_i(t) = E_i \cos[\omega_i t + \varphi_i(t)] \tag{2.4}$$

where E_i is the field amplitude, ω_i is the frequency and $\varphi_i(t)$ is a time-dependent phase-factor of the ith mode. Figure 2.5 illustrates how the relationship between the latter factors will determine the time-dependence of the intensity, $I(t) = (\sum_{i=1}^{N} e_i(t))^2$, of the electric field generated by a superposition of N of these modes in the cavity. Figure 2.5a shows the result obtained from one mode and Fig. 2.5b that of two modes in phase, $\varphi_1(t) = \varphi_2(t)$. Figure 2.5c shows the result obtained from six modes with random phases, whereas Fig. 2.5d shows that of the same six modes with fixed phase relationships, $\varphi_i(t) = \varphi_j(t)$ for all i and j.

The main lesson to be learned from Fig. 2.5 is that when the phases of the modes are synchronized they interfere to generate well-defined time-dependent maxima of the intensity, whereas if there is no relationship between the phases the intensity varies randomly. When synchronized in phase the modes are called *coherent*. Thus, the sun is an incoherent light source, since there is no fixed relation between the phases of the emitted frequencies. Furthermore, comparison of Fig. 2.5b and d illustrates that coherence is crucial for making ultrashort laser pulses: the more cavity modes that can be synchronized in phase the shorter the pulse. The reader is referred to Ref. [36] for a thorough description of ultrashort laser pulses and how phase synchronization is achieved in practice.

Finally, note that while each mode is a standing wave, their coherent superposition is a *wave packet* that travels back and forth in the cavity. This can be shown completely

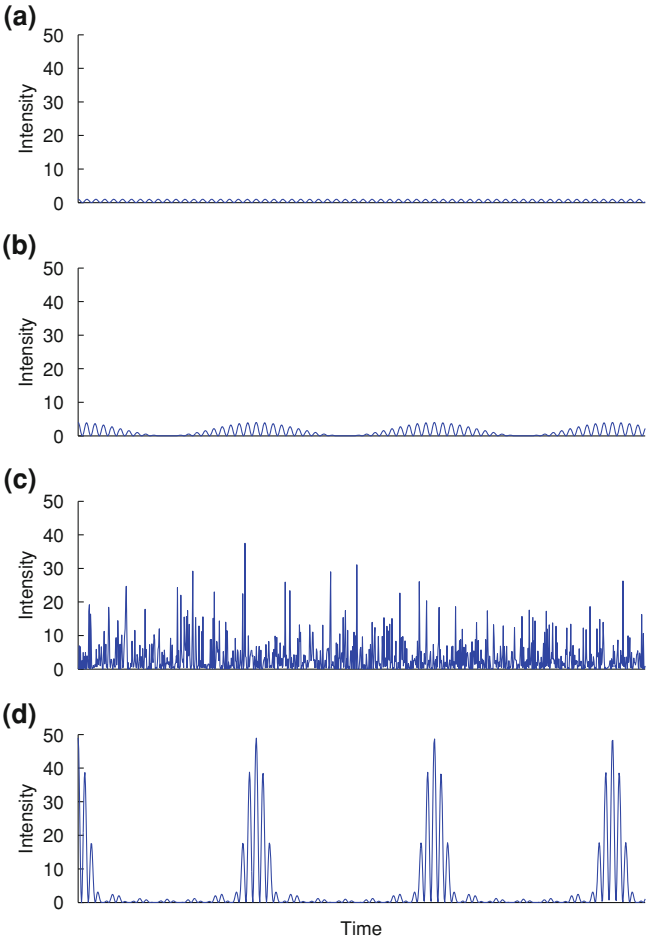

Fig. 2.5 Illustration of how the phase relations between a set of modes, $e_i(t) = E_i \cos[\omega_i t + \varphi_i(t)]$, influence the time-dependent intensity, $I(t) = (\sum_{i=1}^{N} e_i(t))^2$, of the field resulting from their superposition. **a** $N = 1$ mode. **b** $N = 2$ modes in phase, $\varphi_1(t) = \varphi_2(t)$. **c** $N = 6$ modes with random phases. **d** $N = 6$ modes synchronized in phase, $\varphi_i(t) = \varphi_j(t)$ for all i, j

analogously to what was done above in the time domain, by including the spatial dimension in the expression of the transversal modes.

2.2.2 Pump: Creation of a Wave Packet

Having established the concept of coherence, this section serves to explain why coherence plays a crucial role in the excitation step of a pump-probe experiment.

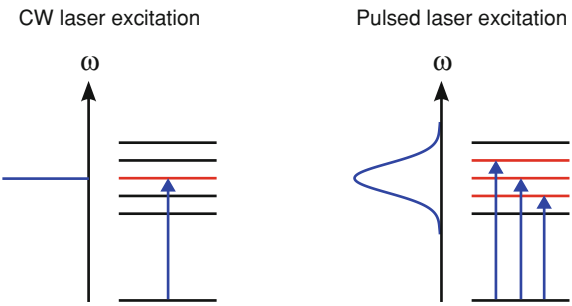

Fig. 2.6 Illustration of how absorption of a photon from a CW laser excites a single eigenstate (*left*), whereas an ultrashort laser pulse excites a coherent superposition of eigenstates (*right*)

First, a comparison between the well-known steady state and the ultrafast time-resolved spectroscopy is instructive. Thus, consider Fig. 2.6 that sketches a one-photon excitation of a ground state molecule by a CW and an ultrafast pulsed laser, respectively. Focusing on the CW excitation of a steady state experiment first, the single frequency component of the laser excites a single eigenstate of the molecule. The norm and any expectation value of an eigenstate is constant in time, which is why eigenstates are often called stationary states. Turning to the pump-probe experiment, an ultrashort laser pulse excites a set of eigenstates contained within the spectral bandwidth of the pulse. Because the phases of the spectral components within this bandwidth are synchronized, the excitation leads to a coherent superposition of stationary states constituting a wave packet $|\Psi(t)\rangle$. This terminology is not coincidental and in the following it will be clear that a wave packet of eigenstates is conceptually quite similar to the wave packet of laser modes discussed above. In view of clarity, assume the wave packet to be comprised of two stationary states $|a\rangle$ and $|b\rangle$ excited simultaneously and in equal amplitude

$$|\Psi(t)\rangle = \frac{1}{\sqrt{2}}\left(e^{-iE_a t/\hbar}|a\rangle + e^{-iE_b t/\hbar}|b\rangle\right) \tag{2.5}$$

where E_a and E_b are the energies of the eigenstates. Note that as opposed to the two terms it is comprised of, the wave packet itself is *not* an eigenstate of the time-dependent Schrödinger equation. By considering the expectation value of the wave packet for a given operator $\hat{X}$, it becomes clear that it is time-dependent [1]

$$\langle\Psi(t)|\,\hat{X}\,|\Psi(t)\rangle = \frac{1}{2}\left(\langle a|\,\hat{X}\,|a\rangle + \langle b|\,\hat{X}\,|b\rangle\right) + \cos[(E_b - E_a)t/\hbar]\,\langle a|\,\hat{X}\,|b\rangle \tag{2.6}$$

This expression illustrates that the coherence of the laser pulse is the key property for the success of the time-resolved experiment: because the stationary states are excited in phase, interference between the states leads to a time-dependent expectation value of the wave packet. In other words, the laser pulse has initiated dynamics in the molecule. In this simplified case of only two stationary states the dynamics is simply an oscillation about the average of the expectation values of each state. But in

more realistic examples in which several states are excited, and their amplitudes and phases are determined by both the transition dipole moment and the spectral components of the laser pulse, wave packets can exhibit significantly more complicated behavior.

In polyatomic molecules, the exact molecular eigenstates contained in the wave packet cannot be computed and even if they could, their coherent superposition would be incomprehensible. Thus, it is often useful to adapt a simpler and more intuitive basis in which to expand the exact eigenstates. As photochemical reactions is the subject of interest here, the adiabatic representation of electronic states mentioned earlier, is an obvious choice. In a typical experiment the wave packet will, at its birth, resemble a single excited electronic state, when expanded in that basis. As time goes by and the phase factors of the exact eigenstates evolve, the wave packet may then, when expanded in the adiabatic basis, turn out to have acquired character of a different electronic state. In the framework of adiabatic states this is a consequence of a non-adiabatic coupling between the electronic states, but it is stressed that the coupling is really a consequence of the choice of expansion basis. A different basis will provide a different view of what is of course the same dynamics. In any case, the expansion in simpler bases provides a more intuitive illustration of how the pump pulse can be used to trigger non-adiabatic dynamics such as a photochemical reaction with fs time-resolution.

2.2.3 Probe: Projection onto a Final State

After its creation by the pump pulse, the wave packet $|\Psi(t)\rangle$ evolves freely for a time Δt after which a second laser pulse probes it by projection on a final state $\left|\Psi_f\right\rangle$ in a one-photon excitation, as sketched in Fig. 2.7. The differential signal resulting from excitation to that particular state can be expressed as [37]

$$S_f(\Delta t) = \left|\langle\Psi_f|\vec{E}_{\text{probe}}(\omega)\cdot\vec{\mu}|\Psi(\Delta t)\rangle\right|^2 \tag{2.7}$$

in which $\vec{E}_{\text{probe}}(\omega)$ is the Fourier transform of the electric field of the probe pulse at the transition frequency ω (this is elaborated on in Sect. 4.2.3) and $\vec{\mu}$ is the transition dipole moment operator. Stolow and Underwood have rewritten Eq. (2.7) to a form that more clearly shows the signal to be comprised of interferences between energetically degenerate two-photon transitions to the final state [37]. For brevity the equation will not be written here, as the conclusion to draw is analogous to that drawn from Eq. (2.6); the experimental signal is modulated at frequencies corresponding to the energy differences between the stationary states within the wave packet.

In the probing step, the phase and amplitude of each of the stationary states are altered by the spectral components of the probe laser and the transition dipole moment to the final state. While the former contribution can be controlled, the latter depends on molecular structure and of course the final state itself. At a given time, there can

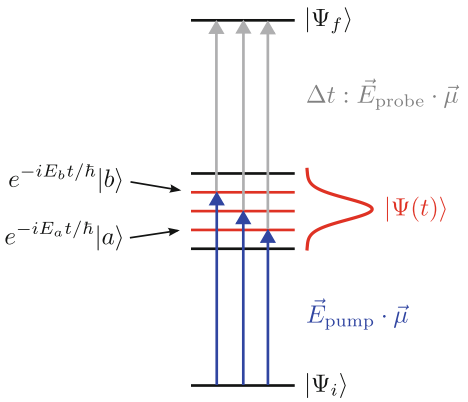

Fig. 2.7 Sketchillustrating the creation, evolution and probing of a wave packet. The experimental signal [see Eq. (2.7)] will be modulated at frequencies corresponding to the energy differences between the stationary states comprising the wave packet, resulting from interferences between energetically degenerate two-photon transitions such as those indicated in the figure

be a large overlap to one final state and a small overlap to another, while at a later time the situation is reversed. This illustrates that the final state acts as a template that the wave packet is projected onto by excitation with the probe pulse. As in every projection, information is lost in the process. But, when choosing different final states one has the possibility of making different projections and thereby hope to recover the (most important part of the) wave packet dynamics.

It is not always experimentally feasible to select a single final state, though, and the collected signal is integrated over a set of energetically allowed final states

$$S(\Delta t) = \sum_f S_f(\Delta t) \tag{2.8}$$

as is the case when measuring total fluorescence, total ion yield, etc. The integration done in such experiments may wash out the information about the wave packet dynamics available from each of the differential signals within the sum or even lead to false conclusions about the dynamics. Stolow and Underwood discuss an example of the latter case, comparing the integral detection of a total ion yield measurement with the differential detection of photoelectron spectroscopy [37].

2.2.4 Experimental Techniques

Even within the limited class of ultrafast experiments involving one optical pump and one optical probe pulse, several experimental schemes exist, e.g. time-resolved transient absorption spectroscopy [38], fluorescence spectroscopy [39], mass spectrometry (TRMS) [37, 39] and photoelectron spectroscopy (TRPES) [37, 39–49], to name a few. Every technique has its practical benefits and drawbacks, but most importantly from a conceptual point of view the final states are different. Thus, this property should (ideally) be the basis for the choice of a technique

for answering a specific scientific question, since it determines the experimental sensitivity towards different dynamics. In this project we have chosen TRMS and TRPES, since especially the latter offers appealing properties and is applicable in a large range of problems. These techniques belonging to time-resolved photoionization spectroscopy have some intriguing fundamental benefits as compared to the other techniques mentioned above, which will be discussed in Chap. 3.

2.3 What is Probed?

When conducting time-resolved experiments a major part of the time is spent on interpreting the results. In that process it is important to realize which factors can influence the experimental signal to ultimately answer the question of what the experiment really probes. This section will mention two such factors

The final state acting as a filter through which the wave packet dynamics is probed.

Sample averaging due to e.g. different environments or structures of the molecules in the sample.

2.3.1 The Final State

When designing a time-resolved experiment, one has to choose a (set of) final state(s) to act as the probing template. This choice should be done wisely, since it determines what information can be extracted from the experiment: it is the filter through which the dynamics is observed. In simple terms, if the experiment aims at answering if the molecule emits yellow light during the course of a chemical reaction, it should be made sure that the filter is indeed transparent to yellow light. The optimal choice of template reflects maximal sensitivity towards the dynamics of interest for the particular experiment. But in many cases too little is known about the final states to achieve this goal and a (more or less) qualified guess on a suitable final state is made. In such situations the interpretation of the experimental signals involves modeling of which molecular parameters the template can be expected to be sensitive to, and which of them are involved in the dynamics studied. Eventually, a close connection to advanced theory is necessary to raise the models to a level above qualified guesses or even to prevent false conclusions. This subject will be touched upon in Part II.

2.3.2 Sample Averaging

So far the attention was drawn to the probing step in a single molecule. Although it is practically possible to do single-molecule experiments [50, 52], most ultrafast

spectroscopy experiments are conducted on samples containing several molecules. Thus, it is important to realize how sample averaging influences the experimental signal. In experiments on molecules in solution the Boltzmann population of vibrational states and the influence of solvent on the local environment of each molecule is an example of such averaging. When conducting time-resolved experiments on molecules in gas phase as in this project, the use of a molecular beam considerably reduces the averaging by cooling the isolated molecules vibrationally and rotationally. But even in gas phase experiments averaging can arise due to the presence of different conformers in the molecular beam. In the time-resolved experiments on [2+2]cycloaddition conducted in this project (Chap. 7), it was possible to extract the contribution of two different conformers from the experimental signal, because of very different time scales of their dynamics, but in general this is not possible. Thus, it is desirable to be able to conduct the experiments on single conformers [53] to get the cleanest possible picture of the molecular dynamics. Recently, spatial separation of conformers in a molecular beam was demonstrated by Filsinger et al. using a very simple technique of deflection in a static electric field [54], but so far it has not been used for time-resolved experiments on conformationally pure samples.

References

1. Brogaard, R.Y.: Teoretiske og eksperimentelle undersøgelser af ultrahurtig dynamik. M. Sc. thesis, University of Copenhagen, In Danish. http://dl.dropbox.com/u/2637141/MscThesisRasmusBrogaard.pdf (2008)
2. Gilbert, A., Baggott, J.: Essentials of Molecular Photochemistry. Blackwell Scientific Publications, Boston (1991)
3. Schinke, R.: Photodissociation Dynamics. Cambridge Monographs on Atomic, Molecular, and Chemical Physics 1. Cambridge University Press, Boston (1993)
4. Horspool, W.M., Song, P.-S. (eds.): CRC Handbook of Organic Photochemistry and Photobiology. CRC Press, Inc., Boca Raton (1995)
5. May, V., Kühn, O.: Charge and Energy Transfer Dynamics in Molecular Systems. Wiley-VCH, Berlin (2000)
6. Domcke, W., Yarkony, D.R., Köppel, H. (eds.): Conical Intersections: Electronic Structure. Dynamics and Spectroscopy. World Scientific Publishing Co. Pte. Ltd., Singapore (2004)
7. Tannor, D.J.: Introduction to Quantum Mechanics—A Time-Dependent Perspective. University Science Books, Sausalito (2007)
8. Turro, N.J., Ramamurthy, V.J.C.: Modern Molecular Photochemistry of Organic Molecules. University Science Books, Scaiano (2010)
9. Eyring, H.: Chem. Rev. **17**, 65–77 (1935)
10. Evans, M.G., Polanyi, M.: Trans. Faraday Soc. **31**, 875–894 (1935)
11. Turro, N.J., Lechtken, P., Lyons, A., Hautala, R.R., Carnahan, E., Katz, T.J.: J. Am. Chem. Soc. **95**, 2035–2037 (1973)
12. De Waele, V., Beutter, M., Schmidhammer, U., Riedle, E., Daub, J.: Chem. Phys. Lett. **390**, 328–334 (2004)
13. Bernardi, F., Olivucci, M., Robb, M.A.: Chem. Soc. Rev. **25**, 321–328 (1996)
14. Migani, A., Olivucci, M.: Conical Intersections: Electronic Structure, Dynamics and Spectroscopy. In: Domcke, W., Yarkony, D.R., Köppel, H. (eds.) Conical Intersections and, Organic

Reaction Mechanisms, Chap 6, pp 272–315. World Scientific Publishing Co. Pte. Ltd., Singapore (2004)
15. Klessinger, M., Michl, J.: Excited States and Photochemistry of Organic Molecules. VCH Publishers Inc., New York (1995)
16. Polli, D., Altoe, P., Weingart, O., Spillane, K.M., Manzoni, C., Brida, D., Tomasello, G., Orlandi, G., Kukura, P., Mathies, R.A., Garavelli, M., Cerullo, G.: Nature **467**, 440–443 (2010)
17. Atchity, G.J., Xantheas, S.S., Ruedenberg, K.: J. Chem. Phys. **95**, 1862–1876 (1991)
18. Yarkony, D.R.: J. Chem. Phys. **114**, 2601–2613 (2001)
19. Martinez, T.J.: Nature **467**, 412–413 (2010)
20. Migani, A., Robb, M.A., Olivucci, M.: J. Am. Chem. Soc. **125**, 2804–2808 (2003)
21. Cederbaum, L.S.: Conical Intersections: Electronic Structure, Dynamics and Spectroscopy. In: Domcke, W., Yarkony, D.R., Köppel, H. (eds.) Born-Oppenheimer Approximation and Beyond, Chap 1, p 6. World Scientific Publishing Co. Pte. Ltd., Singapore (2004)
22. von Neumann, J., Wigner, E.P.Z.: Physik **30**, 467–470 (1929)
23. Truhlar, D.G., Mead, C.A.: Phys. Rev. A **68**, 032501 (2003)
24. Rose, T.S., Rosker, M.J., Zewail, A.H.: J. Chem. Phys. **88**, 6672–6673 (1988)
25. Mokhtari, A., Cong, P., Herek, J.L., Zewail, A.H.: Nature **348**, 225–227 (1990)
26. Møller, K.B., Henriksen, N.E., Zewail, A.H.: J. Chem. Phys. **113**, 10477–10485 (2000)
27. El-Sayed, M.A.: J. Chem. Phys. **36**, 573–574 (1962)
28. El-Sayed, M.A.: J. Chem. Phys. **38**, 2834–2838 (1963)
29. El-Sayed, M.A.: J. Chem. Phys. **41**, 2462–2467 (1964)
30. Zener, C.: Proc. R. Soc. London, Ser. A **137**, 696–702 (1932)
31. Desouter-Lecomte, M., Lorquet, J.C.: J. Chem. Phys. **71**, 4391–4403 (1979)
32. Köppel, H., Cederbaum, L.S., Domcke, W., Shaik, S.S.: Angew. Chem. Int. Ed. Engl. **22**, 210–224 (1983)
33. Lee, A.M.D., Coe, J.D., Ullrich, S., Ho, M.-L., Lee, S.-J., Cheng, B.-M., Zgierski, M.Z., Chen, I.-C., Martinez, T.J., Stolow, A.: J. Phys. Chem. A **111**, 11948–11960 (2007)
34. Chergui, M., Zewail, A.H.: Chem. Phys. Chem. **10**, 28–43 (2009)
35. Shorokhov, D., Zewail, A.H.: J. Am. Chem. Soc. **131**, 17998–18015 (2009)
36. Rullière, C.: Femtosecond Laser Pulses. Principles and Experiments. Springer, Berlin (1998)
37. Stolow, A., Underwood, J.G.: In: Rice, S.A. (ed.): Advances in Chemical Physics, vol. 139, pp. 497–584. Wiley, New York (2008)
38. Nibbering, E.T., Fidder, H., Pines, E.: Annu. Rev. Phys. Chem. **56**, 337–367 (2004)
39. Hertel, I.V., Radloff, W.: Rep. Prog. Phys. **69**, 1897–2003 (2006)
40. Seel, M., Domcke, W.: J. Chem. Phys. **95**, 7806–7822 (1991)
41. Kim, B., Schick, C.P., Weber, P.M.: J. Chem. Phys. **103**, 6903–6913 (1995)
42. Neumark, D.M.: Annu. Rev. Phys. Chem. **52**, 255–277 (2001)
43. Seideman, T.: Annu. Rev. Phys. Chem. **53**, 41–65 (2002)
44. Reid, K.L.: Annu. Rev. Phys. Chem. **54**, 397–424 (2003)
45. Stolow, A.: Annu. Rev. Phys. Chem. **54**, 89–119 (2003)
46. Stolow, A., Bragg, A.E., Neumark, D.M.: Chem. Rev. **104**, 1719–1758 (2004)
47. Wollenhaupt, M., Engel, V., Baumert, T.: Annu. Rev. Phys. Chem. **56**, 25–56 (2005)
48. Suzuki, T.: Annu. Rev. Phys. Chem. **57**, 555–592 (2006)
49. Reid, K.L.: Int. Rev. Phys. Chem. **27**, 607–628 (2008)
50. van Dijk, E.M.H.P., Hernando, J., García-López, J.-J., Crego-Calama, M., Reinhoudt, D.N., Kuipers, L., García-Parajó, M.F., van Hulst, N.F.: Phys. Rev. Lett. **94**, 078302 (2005)
51. Hernando, J., van Dijk, E.M.H.P., Hoogenboom, J.P., Garíca-López, J.-J., Reinhoudt, D.N., Crego-Calama, M., García-Parajó, M.F., van Hulst, N.F.: Phys. Rev. Lett. **97**, 216403 (2006)
52. Hildner, R., Brinks, D., Stefani, F.D., van Hulst, N.F.: Phys. Chem. Chem. Phys. **13**, 1888–1894 (2011)
53. Stolow, A.: Nature **461**, 1063–1064 (2009)
54. Filsinger, F., Küpper, J., Meijer, G., Hansen, J.L., Maurer, J., Nielsen, J.H., Holmegaard, L., Stapelfeldt, H.: Angew. Chem., Int. Ed. **48**, 6900–6902 (2009)

Chapter 3
A Time-Resolved Probing Method: Photoionization

Seel and Domcke were the first to suggest the use of time-resolved photoionization experiments to investigate ultrafast molecular dynamics [1, 2]. Since then experimentalists all over the world have made numerous implementations of time-resolved photoionization experiments, of which this chapter will focus on experiments on neutral molecules in a molecular beam. Since a more rigorous mathematical treatment will be given in Part II, this chapter serves to qualitatively highlight important concepts illustrating the universality of the experimental approach.

3.1 Fundamentals

3.1.1 The Final State

In time-resolved photoionization the probe pulse removes an electron—ideally in a one-photon optical transition. Since this process is allowed for all molecular configurations, photoionization provides a universal probing scheme, to which no electronic state or molecular structure is dark. This is one of the main benefits of the technique as compared to e.g. time-resolved transient absorption or fluorescence spectroscopy, in which electronic symmetry restrictions and Franck–Condon overlaps to the final state can prevent the probing of some molecular configurations. The reason for this can be appreciated by considering the final state; in the case of photoionization it is a continuum containing the cation and the free electron states. As all other optical transitions photoionization is subject to selection rules enforced by symmetry restrictions. Thus, group theory dictates that the direct product of the irreducible representations of the final state, the transition dipole moment and the state being ionized, has to contain the totally symmetric irreducible representation of the molecular point group, for the transition to be allowed. But, because the final state contains the free electron wave function which can take on any symmetry, any ionization transition is allowed. This also means that the free electron wave function can be used to derive symmetry properties of the excited state wave function by measuring

R. Y. Brogaard, *Molecular Conformation and Organic Photochemistry*, Springer Theses, DOI: 10.1007/978-3-642-29381-8_3,
© Springer-Verlag Berlin Heidelberg 2012

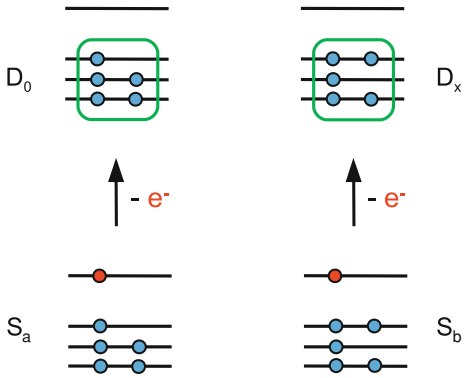

Fig. 3.1 Illustration of ionization correlations of two excited states S_a and S_b. The correlations can be rationalized using the Koopmans picture of photoionization that involves a single active electron (*red*) and leaves the electronic configuration of the core unchanged

the angular distribution of the emitted photoelectrons. An elegant example of how this is used in a time-resolved photoionization experiment probing the non-adiabatic dynamics of a photodissociation can be found in Refs. [3, 4].

3.1.2 Ionization Correlations

It is fairly straightforward to appreciate that nuclear dynamics is mapped out through the overlap between the vibrational wave functions of the neutral and the cation state, but in fact the ionization continuum also provides a template for probing changes in the electronic structure. This is most clearly appreciated by employing the Koopmans picture (Ref. [5] and references therein), in which the ionization process involves a single active electron and leaves the electronic configuration of the core unchanged. Consider as an example two excited states S_a and S_b with the electronic configuration shown in Fig. 3.1. In the Koopmans picture, ionization of these states will leave the cation in the ground and an excited state, respectively. This relation has been referred to as an ionization correlation between the neutral excited state and the ion state [5–8]. Although these correlations should be perceived as propensities more than strict rules, they often work surprisingly well in predicting which cation states are populated by ionization. Based on an inherently 'single molecular orbital' picture, the ionization correlations do not work well in cases of highly multiconfigurational excited states of the neutral and/or the cation. In such cases it is necessary to calculate the overlap between the electronic wave functions of the excited state and the different cation states to predict the preferred final state of the cation. The theoretical framework for calculating these overlaps will be presented in Part II.

3.2 Probing Non-Adiabatic Dynamics Through Photoionization

Having established that the molecular ionization continuum provides a versatile template for probing nuclear and electronic structure, Fig. 3.2 illustrates how this template is used in a time-resolved experiment to probe ultrafast non-adiabatic dynamics in

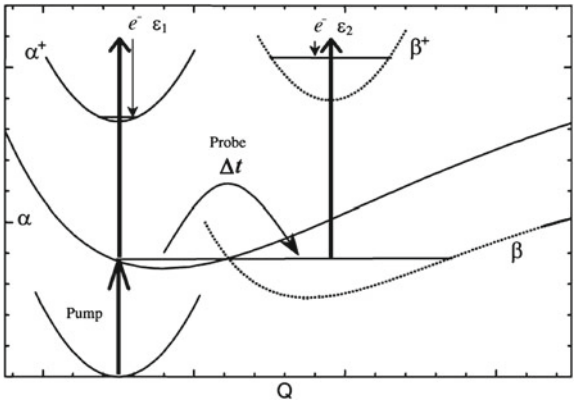

Fig. 3.2 Illustration of how non-adiabatic dynamics is probed in a time-resolved photoionization experiment. Excitation with the pump pulse prepares a wave packet initially resembling the state α that correlates to the cation state α^+. When ionized by a photon from the probe pulse, this state will give rise to the photoelectron spectrum ϵ_1. At a later time motion along the nuclear coordinate Q has induced a non-adiabatic transition, and the wave packet resembles the β state which correlates to the β^+ state of the cation, producing the photoelectron spectrum ϵ_2 when ionized. Fig. 2 in Ref. [5]

polyatomic molecules. Consider a situation in which the pump pulse prepares a wave packet initially resembling the electronic state α. As it turns out, this state correlates to the electronic state α^+ of the cation. Ionization of the state α with the probe pulse will produce photoelectrons with a spectrum ϵ_1 of kinetic energies. Due to a non-adiabatic electronic transition promoted by motion along the nuclear coordinate Q, the wave packet will at a later time resemble the vibrationally excited electronic state β, that correlates to the β^+ state of the cation. Since the latter state is energetically above the α^+ state, the photoelectron spectrum ϵ_2 produced by ionization of β will be significantly shifted from ϵ_1. This helps to distinguish not only the electronic but also the vibrational dynamics, since nuclear motion taking place in the electronic states α and β is reflected in the (time-dependent) Franck–Condon envelopes of the ϵ_1 and ϵ_2 spectrum, respectively. This shows that it is possible to trigger and probe ultrafast non-adiabatic dynamics as for example in a photochemical reaction by measuring the photoelectron spectrum as a function of time-delay between the pump and probe pulses.

For reasons of clarity, the ideal case of states that correlated to different states of the cation, referred to as complementary ionization correlations [7], was chosen in the example above. In the more complicated situation of excited states correlating to the same state of the cation, corresponding ionization correlations [8], it is in favorable cases still possible to follow the molecular dynamics in the time-resolved photoelectron spectrum. This is particularly true for rigid molecules in which the vibrational energy in the neutral state is transferred to the cation during ionization. Applying this to the example presented above, the ϵ_2 spectrum would then be shifted

compared to ϵ_1 by an amount corresponding to the vibrational energy transferred to the β state as a consequence of the IC from the α state, allowing the spectra to be distinguished, as demonstrated experimentally by Schmitt et al. [8]. Another way of stating that the vibrational energy of the neutral state is transferred to the cation, is that the Franck–Condon envelope of the photoelectron spectrum is peaked at $\Delta v = 0$ vibrational transitions. As it turns out, a rigid geometry is sufficient but not necessary for this to be fulfilled. Molecular Rydberg states [9], in which an electron is excited to a molecular orbital resembling an orbital of the Hydrogen atom, closely resemble cation states because the orbiting Rydberg electron has little contact with the molecular core. Because of this resemblance, the photoelectron spectra of Rydberg states are sharp peaks, due to a narrow Franck–Condon envelope favoring $\Delta v = 0$ transitions (Ref. [10] and references therein). Thus, Gosselin et al. demonstrated how IC between two Rydberg states exhibiting corresponding ionization correlations was easily followed in the time-resolved photoelectron spectrum due to clearly distinguishable spectra of the states [11].

The above was largely focused on the general case of IC between electronic states, but before ending this section it is worth elaborating slightly on how nuclear dynamics can be probed. Thus, for brevity consider the specific case of probing nuclear dynamics on a single PES. As mentioned above, the Franck–Condon envelope of the photoelectron spectrum reflects the vibrational overlap between the wave packet and the cation state. Provided the equilibrium geometry of the cation state is known, this will reveal the nuclear displacement coordinate along which the wave packet travels. But in cases where the wave packet travels to a region of nuclear configuration space far from the equilibrium geometry of the cation, this way of discerning the nuclear dynamics will fail, since the Franck–Condon envelope will be broad and unstructured. In such cases the time-evolution of the center position of the photoelectron spectrum can reveal the location of the wave packet on the PES, since in general the ionization potential (IP) depends on the nuclear coordinates. Finally, note that when this is not true, i.e. when the PESs of the neutral and cation states are parallel as e.g. in the case of Rydberg states, nuclear dynamics are not reflected in the photoelectron spectrum. It follows that (everything else being equal) only nuclear dynamics that influences the IP can be directly probed in TRPES. These issues will be discussed in more detail in Chap. 5 that presents an example of a simulation of time-resolved photoionization signals probing ultrafast nuclear dynamics taking place on a single PES.

3.2.1 Choosing a Pump–Probe Scheme

In view of clarity the issue was not addressed above, but the cleanest results of photoionization experiments are obtained when the probing step involves only one photon. When using two (or more) photons for the probing, there is a great risk that an intermediate highly excited state is reached before ionization. If so, this state will act as a filter in the probing process, potentially blurring or even hiding important

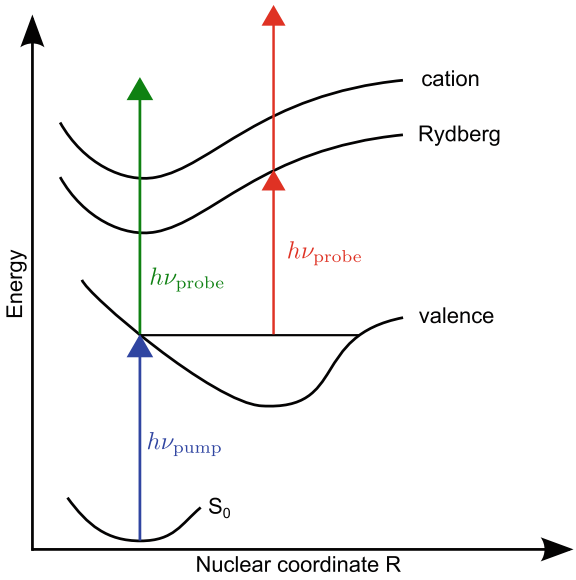

Fig. 3.3 Illustration of a time-resolved photoionization experiment in which an intermediate Rydberg state involved in a two-photon probing scheme filters out information about valence state nuclear dynamics, that is revealed in the photoelectron spectrum using a one-photon probing scheme. See text for details

information about the wave packet that would have been available using a one-photon probing scheme. An example involving nuclear dynamics in an excited valence state is depicted in Fig. 3.3.

Using one-photon probing, the dynamics is reflected in the Franck–Condon envelope of the excited-state photoelectron spectrum. A two-photon probing scheme, on the other hand, could involve an intermediate high-lying state which is likely to be of Rydberg character. As mentioned above, the Franck–Condon envelopes of Rydberg photoelectron spectra are narrow and peaked at $\Delta v = 0$. Thus, whatever information was available about the nuclear dynamics is "absorbed" by the Rydberg state and cannot be recovered from the photoelectron spectrum resulting from ionization through that intermediate state.

Using a two-photon pump scheme is also problematic, though it might in some cases be of scientific interest [12]. The problem is that it is difficult to avoid absorption of a third photon. As will be discussed in Chap. 9 that is indeed what happened in a time-resolved experiment on 1,3-dibromopropane; the experimental signal was previously thought to reflect dynamics in an excited state of the neutral molecule [13], but it turned out to be dynamics taking place in an excited state of the cation prepared by absorption of three photons of the pump pulse.

Whereas it is in most cases possible to choose a wavelength of the pump pulse suitable for one-photon absorption, choosing a probe wavelength suitable for one-photon probing is often difficult. The ideal choice is a wavelength short enough to ionize even the ground state with one photon. As the IP of most organic molecules fall in the range of 8–10 eV this corresponds to wavelengths of 125–155 nm. To reach these wavelengths from the fundamental wavelength range of Ti:Sapphire ultrafast

pulsed lasers of 750–850 nm, the fifth or sixth harmonic of the fundamental frequency has to be generated. While time-resolved photoionization experiments using such deep UV pulses have been demonstrated [14, 15], in most laboratories the fourth harmonic (∼200 nm) is the lower wavelength limit. Thus, in the more common case the probe wavelength is chosen as short as possible, while avoiding wavelengths that are absorbed by the ground state molecule, as this will generate signal from dynamics induced by the probe and probed by the pump. Although disentanglement of pump–probe from probe–pump signal has been demonstrated [16], it is general desirable to avoid such added complexity in the experimental data.

Summing up, a one-photon pump one-photon probe scheme is desirable, but in cases in which this cannot be achieved due to the requirements outlined above, it is replaced by a scheme involving two (or more) probe photons. This is the situation in the paracyclophane experiments presented in Chaps. 7 and 8. From here on the shorthand notation $[X,Y']$ will denote a process involving X photons of the pump and Y photons of the probe pulse.

3.3 Analyzing and Interpreting Experimental Results

The previous sections illustrated in general terms how the wave packet dynamics can be extracted from the data obtained in a time-resolved photoionization experiment. But in order to achieve a quantitative measure of the dynamics in practice, a systematic data analysis has to be performed. It is important to realize that already in this process of quantification, a model is imposed on the data. This section discusses the common assumptions leading to these models and how they influence the conclusions drawn about the molecular dynamics from the experimental results.

3.3.1 Ultrafast Dynamics Modeled by First Order Kinetics

In the analysis of both TRMS and TRPES data it is nearly always assumed that the dynamics follows first order kinetics, which can be described by a set of linear differential equations. This model is used extensively in all areas of physics and chemistry and the solution to such a set of equations is given by a sum of exponentials [17]. To obtain an expression that can be used to fit experimental signals, the molecular response has to be convolved with the Gaussian cross-correlation between the pump and the probe pulses that in the present case defines the instrument response function of the experiment. For a monoexponential decay with rate k the analytical expression for the convolution with a Gaussian centered at $t = 0$ is [18]

$$B(k, \sigma_{cc}, t) = \exp(-kt) \exp\left[\frac{(\sigma_{cc}k)^2}{2}\right] \frac{1}{2}\left(1 + \mathrm{erf}\left[\frac{1}{\sqrt{2}}\left(\frac{t}{\sigma_{cc}} - \sigma_{cc}k\right)\right]\right) \quad (3.1)$$

where σ_{cc} is related to the experimentally determined full-width at half maximum (fwhm) of the Gaussian cross-correlation function, $\text{fwhm}_{cc} = 2\sigma_{cc}\sqrt{2\ln 2}$. Examples of how linear combinations of these functions can be used to model multi-exponential decay and rise in experimental signals of fs time-resolved experiments are given in Ref. [18], and below it is shown how the functions are used to fit time-resolved photoelectron spectra.

For dynamics on a time scale of ps or longer the first order kinetics model seems reasonable because on such long time scales the behavior is likely to be statistical in nature. A well known example is passage through a transition state in a ground state reaction. But also in photochemistry statistical behavior can be observed; in case the CI is preceded by a significant barrier on the excited-state PES, passage through this excited-state transition state will control the population decay of the excited state, which will then be well described by first order kinetics. Another more subtle case is when oscillation along a given a nuclear coordinate in the excited-state PES brings the wave packet in and out of a region of high non-adiabatic coupling. A famous example is the NaI photodissociation experiment illustrated in Fig. 2.3. Because a constant (small) part of the population is transferred to the ground state at every encounter with the avoided crossing, the period-averaged time evolution of the excited-state population can be fitted to a monoexponential decay [19]. But for ultrafast wave packet dynamics directly reflecting nuclear motions, the experimental signal cannot be described by first order kinetics [19, 20]. In the simulation of time-resolved photoionization signals on acetone discussed in Chap. 5 we arrived at the same conclusion. But importantly, the decay constant derived from an exponential fit was practically identical to that obtained from the better Gaussian fit of the signal decay.[I] Thus, while the functional form is incorrect, the time constants obtained from exponential fits of signals reflecting dynamics on a sub-ps time scale are often in good agreement with the intrinsic time constants of the molecular dynamics.

3.3.2 Time-Resolved Mass Spectrometry

A priori, mass- and time-resolved detection of the ions generated by photoionization seems like a technique very well suited for the study of ultrafast dissociation reactions of organic molecules; the temporal evolution of the peaks in the mass spectrum corresponding to the fragments would reflect the dynamics of the dissociation. But as Fig. 3.4 illustrates, in many cases a given fragment ion can be generated via (at least) two pathways; from direct ionization of the corresponding neutral and from dissociation of the parent ion. This ambiguous origin complicates the interpretation of the experimental signals to an extent that in most cases requires TRPES or other differential detection schemes to determine whether a dissociation takes place in the neutral excited state or in the cation. The work of Gosselin et al. provides an illustrative example of this issue and the resolution of it using TRPES [11].

But even in cases not concerned with dissociation, TRMS results can be misleading and should be interpreted with care. Consider again the generic example of IC

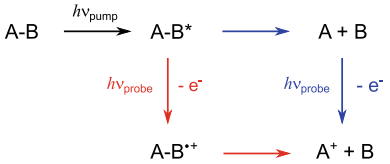

Fig. 3.4 Illustration of the issue of ambiguous origin of fragment ions in TRMS: a fragment ion can result either from ionization of the corresponding neutral (*blue path*) or from dissociation of the parent ion (*red path*)

presented in Fig. 3.2. The time-evolution of the parent ion signal in the mass spectrum can be obtained by integrating the time-resolved photoelectron spectrum along the energy axis (assuming negligible fragmentation of the ion). The signal will therefore be a weighted sum of the contribution from each electronic state, the weight being determined by the photoionization cross section of that particular state. This clearly illustrates how TRMS as an integral detection scheme blurs information easily available in the data from a differential technique such as TRPES; only in the limiting case that no parent ions are generated from the β state, the parent ion signal reflects the time scale for IC, as was the case in the work of Gosselin et al. [11]. If there is some amount of parent ions generated from probing the wave packet in the β state, the signal will reflect a weighted average of the lifetimes of the α and the β states that has nothing to do with the IC dynamics. Using TRPES to resolve it, Stolow and Underwood have demonstrated examples of both the former limiting and the latter more common case, depending on the wavelength of the ionizing probe [5].

The issues discussed above illustrate the potential pitfalls when interpreting TRMS results: in many cases the time-evolution of the parent ion signal does not directly reflect the dynamics in the parent molecule and a differential detection technique like TRPES is necessary. That being said, TRMS is still a useful supplement to TRPES, especially in the form of experiments in which the ion and the photoelectron are detected in coincidence (see e.g. Refs. [21–23] and references therein).

3.3.3 Time-Resolved Photoelectron Spectroscopy

Although the results from a TRPES experiment in principle carry a huge amount of information about the wave packet dynamics, extracting this information in a comprehensible form is a challenging task on its own. The most common approach is to do a global fit [24–27] of the time-resolved photoelectron spectrum, in which both the temporal and spectral dimensions are fitted simultaneously. In this work we employ the multi-exponential approach [25] and fit the dataset $S(\Delta t, E)$ of photoelectron kinetic energies E as a function of time-delay Δt between the pump and probe pulses to the following expression

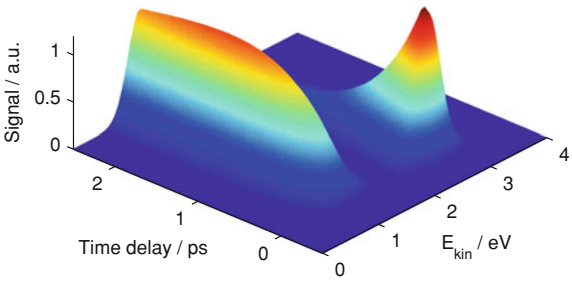

Fig. 3.5 Synthetic time-resolved photoelectron spectrum resembling data obtained when probing the non-adiabatic dynamics as sketched in the generic scenario in Fig. 3.2

$$S(\Delta t, E) = \sum_i A_i(E) B_i(\Delta t) \qquad B_i(t) = B(k_i, \sigma_{cc}, t) \tag{3.2}$$

where the *decay-associated spectrum* (DAS) $A_i(E)$ represents the fitted amplitudes across the kinetic energy spectrum of the basis function $B_i(t)$.

Figure 3.5 shows a synthetic time-resolved photoelectron spectrum resembling the data that would be obtained from an experiment probing the non-adiabatic dynamics sketched in Fig. 3.2. A global fit of the spectrum according to Eq. (3.2) would result in two DASs A_1 and A_2 and the corresponding basis functions B_1 and B_2 displayed in Fig. 3.6. Note from Fig. 3.6a that while A_2 equals the ϵ_2 photoelectron spectrum of the β state, A_1 contains both the ϵ_1 and the ϵ_2 spectrum, the latter at negative amplitude. There is of course nothing physical in negative amplitudes and it is only a consequence of the mathematical model used to describe the population kinetics. This can be appreciated by considering Fig. 3.6b that in addition to B_1 and B_2 also show the time-dependent populations of the electronic states, convolved with the Gaussian cross correlation. Since the population of the β state rises at rate k_1 and decays at rate k_2, this is modeled using a negative amplitude of the B_1 (from A_1) and a positive amplitude of the B_2 basis function (from A_2) in the spectral region of the photoelectron spectrum ϵ_2 of the β state. Once this relation between DASs and real photoelectron spectra is appreciated it serves a convenient way to determine the electronic population dynamics: the population in the α state, represented by the region of A_1 with positive amplitudes, goes to the β state because the spectrum of this state appears in the region of A_1 with negative amplitudes. In A_2 that has a corresponding spectrum of positive amplitudes, the fate of the β state can be observed (in the present case it just decays to a state not probed in the experiment).

The review above illustrates how the photoelectron spectra of the excited states and their order of population in the course of the (reaction) dynamics can be derived from the DASs, whereas the decay rates of the basis functions provide the time constants. Although very powerful and attractive, there is one important assumption in this global fit model: the time-independence of the excited-state photoelectron spectra. This assumption is quite good for rigid molecules in which the electronic transitions are associated with relatively small structural changes. But in cases of large-amplitude motion the Franck–Condon overlap to the vibrational states of the cation and, more importantly, the IP change significantly, thereby causing the spectral envelope to shift

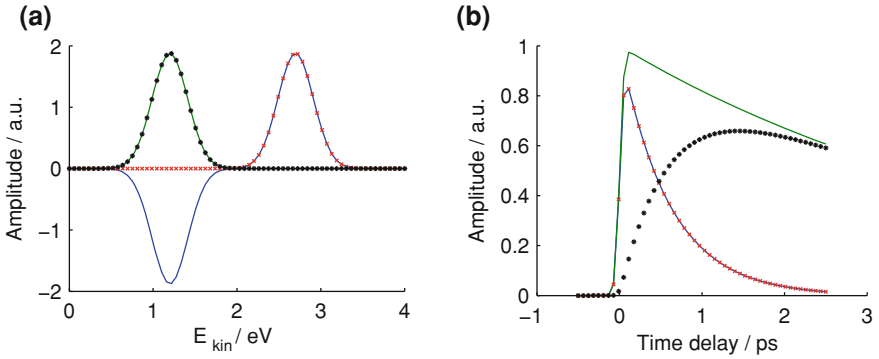

Fig. 3.6 Representation of the global fit of the time-resolved photoelectron spectrum shown in Fig. 3.5. **a** DASs A_1 (*blue*) and A_2 (*green*). Also shown are the photoelectron spectra ϵ_1 (*red*) and ϵ_2 (*black*). **b** basis functions B_1 (*blue*) and B_2 (*green*). Also shown are the time-dependent populations of the α (*red*) and β (*black*) states, convolved with the Gaussian cross correlation of the pump and probe pulse

as time goes by. In such cases the assumption of time-independent photoelectron spectra is inherently invalid and the global fitting procedure outlined above fails [28, 29]. These issues illustrate that in practice the global fitting procedure is best (if not exclusively) suited for extracting the kinetics of the electronic population dynamics.

Cases in which nuclear dynamics is of specific interest pose a challenge for the analysis. As an example, the time-resolved photoionization experiment on acetone dealt with in this work (Chap. 5), presents a case in which the increase of IP is so pronounced that during the dynamics the excited-state photoelectron spectrum is shifted out of the energy range accessible by the probe. Often, the conclusion of efforts devoted to interpreting such complex experimental data will be that support is needed from advanced theory and simulations to reveal the dynamics of the wave packet. The pursuit of a closer relation between theory and experiment in time-resolved photoionization is the subject of the following part of the thesis.

References

1. Seel, M., Domcke, W.: J. Chem. Phys. **95**, 7806–7822 (1991)
2. Seel, M., Domcke, W.: Chem. Phys. **151**, 59–72 (1991)
3. Bisgaard, C.Z., Clarkin, O.J., Wu, G., Lee, A.M.D., Geßner, O., Hayden, C.C., Stolow, A.: Science **323**, 1464–1468 (2009)
4. Hockett, P., Bisgaard, C.Z., Clarkin, O.J., Stolow, A.: Nat. Phys. **7**, 612–615 (2011)
5. Stolow, A.; Underwood, J.G.: In: Rice, S.A. (ed.) Advances in Chemical Physics, Vol. 139, pp. 497–584. Wiley, New York (2008)
6. Blanchet, V., Zgierski, M.Z., Seideman, T., Stolow, A.: Nature **401**, 52–54 (1999)
7. Blanchet, V., Zgierski, M.Z., Stolow, A.: J. Chem. Phys. **114**, 1194–1205 (2001)

8. Schmitt, M., Lochbrunner, S., Shaffer, J.P., Larsen, J.J., Zgierski, M.Z., Stolow, A.: J. Chem. Phys. **114**, 1206–1213 (2001)
9. Mulliken, R.S.: J. Am. Chem. Soc. **86**, 3183–3197 (1964)
10. Kuthirummal, N., Weber, P.M.: Chem. Phys. Lett. **378**, 647–653 (2003)
11. Gosselin, J.L., Minitti, M.P., Rudakov, F.M., Sølling, T.I., Weber, P.M.: J. Phys. Chem. A **110**, 4251–4255 (2006)
12. Schalk, O.; Boguslavskiy, A.E.; Stolow, A. (2011), in preparation
13. Kötting, C., Diau, E.W.-G., Sølling, T.I., Zewail, A.H.: J. Phys. Chem. A **106**, 7530–7546 (2002)
14. Peralta Conde, A., Kruse, J., Faucher, O., Tzallas, P., Benis, E.P., Charalambidis, D.: Phys. Rev. A **79**, 061405 (2009)
15. Allison, T.K., Wright, T.W., Stooke, A.M., Khurmi, C., van Tilborg, J., Liu, Y., Falcone, R.W., Belkacem, A.: Opt. Lett. **35**, 3664–3666 (2010)
16. Lee, S.-H., Tang, K.-C., Chen, I.-C., Schmitt, M., Shaffer, J.P., Schultz, T., Underwood, J.G., Zgierski, M.Z., Stolow, A.: J. Phys. Chem. A **106**, 8979–8991 (2002)
17. Istratov, A.A., Vyvenko, O.F.: Rev. Sci. Instrum. **70**, 1233–1257 (1999)
18. Pedersen, S., Zewail, A.H.: Mol. Phys. **89**, 1455–1502 (1996)
19. Møller, K.B., Henriksen, N.E., Zewail, A.H.: J. Chem. Phys. **113**, 10477–10485 (2000)
20. Møller, K.B., Zewail, A.H.: Chem. Phys. Lett. **351**, 281–288 (2002)
21. Davies, J.A., LeClaire, J.E., Continetti, R.E., Hayden, C.C.: J. Chem. Phys. **111**, 1–4 (1999)
22. Hertel, I.V., Radloff, W.: Rep. Prog. Phys. **69**, 1897–2003 (2006)
23. Geßner, O., Lee, A.M.D., Shaffer, J.P., Reisler, H., Levchenko, S.V., Krylov, A.I., Underwood, J.G., Shi, H., East, A.L.L., Wardlaw, D.M., Chrysostom, E.t.H., Hayden, C.C., Stolow, A.: Science **311**, 219–222 (2006)
24. Satzger, H., Zinth, W.: Chem. Phys. **295**, 287–295 (2003)
25. van Stokkum, I.H.M., Larsen, D.S., van Grondelle, R.: Biochim. Biophys. Acta, Bioenerg. **1657**, 82–104 (2004)
26. Mullen, K., Vengris, M., van Stokkum, I.: J. Global Optim. **38**, 201–213 (2007)
27. van Wilderen, L.J.G.W., Lincoln, C.N., van Thor, J.J.: PLoS ONE **6**, e17373 (2011)
28. Lee, A.M.D., Coe, J.D., Ullrich, S., Ho, M.-L., Lee, S.-J., Cheng, B.-M., Zgierski, M.Z., Chen, I.-C., Martinez, T.J., Stolow, A.: J. Phys. Chem. A **111**, 11948–11960 (2007)
29. Schalk, O., Boguslavskiy, A.E., Stolow, A., Schuurman, M.S.: J. Am. Chem. Soc. **133**, 16451–16458 (2011)

Part II
Theory

Chapter 4
Simulation of Time-Resolved Photoionization Signals

In any scientific field there is a mutual benefit from the combination of theory and experiment in which progress in one discipline stimulates new efforts in the other. Thus, the pioneering theoretical work of Seel and Domcke lead to the birth of ultrafast time-resolved photoionization experiments [1, 2]. Whereas much effort in theory is devoted to such exploratory tracks, this chapter will focus on the simulation of signals obtained from experiments already conducted. While striving for the best possible agreement between theory and experiment the real purpose of such simulations is to aid the interpretation of experimental data, ultimately aiming at a better understanding of the molecular dynamics under investigation.

The chapter is divided into two sections, in which the first is devoted to quantum simulation of ultrafast non-adiabatic molecular dynamics. The second section discusses the challenges faced when pursuing the closest possible relation between experiment and theory in the simulation of time-resolved photoion and—electron signals.

4.1 Quantum Molecular Dynamics: The AIMS Method

The Born–Oppenheimer approximation that separates the Schrödinger equation into an electronic and a nuclear part constitutes the framework that most chemists think within. Quantum chemistry software for solving the electronic part with frozen nuclei is now capable of doing highly accurate calculations on ground and excited states of increasingly larger molecular systems while maintaining a high degree of accessibility, and synthetic chemists now use it on a daily basis. In molecular dynamics simulations the focus is on the nuclear motion and numerous approaches ranging from purely classical to full quantum descriptions exist. The distinct separation of electronic structure calculation for constructing the PESs and the use of Newtonian mechanics to describe the (classical) nuclear dynamics on these PESs often works well [3]. But in cases such as photochemical reactions where the Born–Oppenheimer approximation breaks down and the molecular dynamics becomes non-adiabatic, an

R. Y. Brogaard, *Molecular Conformation and Organic Photochemistry*,
Springer Theses, DOI: 10.1007/978-3-642-29381-8_4,
© Springer-Verlag Berlin Heidelberg 2012

accurate description has to couple calculations of electronic structure and nuclear dynamics. In other words, the quantum mechanical coupling between the nuclei and the electrons has to be taken into account. Several approaches that achieve this exist and it is not the intent of this section to present an exhaustive overview. Rather, the approach of the ab initio multiple spawning (AIMS) method [3–17] used in this work will be reviewed. It is stressed, though, that mainly general concepts are discussed and a more detailed description of the AIMS method can be found in Ref. [3].

4.1.1 Electronic Structure

To obtain useful results from a quantum molecular dynamics (QMD) simulation an accurate description of the electronic structure is crucial. This task is more challenging than calculating vertical excitation energies from a ground state equilibrium geometry leading to prediction of absorption spectra. One example is doubly excited states that are not optically active and therefore have a minor influence on the absorption spectrum. But non-adiabatic dynamics outside the Franck-Condon region can lead to a non-radiative transition to such a state [3, 18, 19]. Hence, the electronic structure model used in QMD has to appropriately describe doubly excited states for the simulation to be even qualitatively correct. Furthermore, as mentioned earlier most photochemistry happens at CIs and other regions of large non-adiabatic coupling, so the electronic structure model has to correctly describe heavily mixing states and their coupling. Finally, the model also faces the challenge of achieving a balanced description of ground and excited states so as not to favour one over the other.

AIMS has been used with several different electronic structure models [4, 9, 14, 15], but in this work we have used the state-averaged complete active space self-consistent field [20] (SA-CASSCF) method. As it is not the purpose of this section to extensively discuss electronic structure models, the reader is referred to Ref. [3] for a justification of the choice of method. In this work the simulations were conducted using a code that integrates AIMS dynamics in the MOLPRO package for electronic structure calculations [21].

When conducting QMD simulations the representation of the electronic states is crucial, because it determines the form of their mutual coupling. Previously we introduced the adiabatic representation in which the electronic states diagonalize the electronic potential energy, but are coupled through the nuclear kinetic energy operator. In this representation the electronic character of each state changes as a function of nuclear displacement. In regions of large coupling this change is rapid and at a CI it diverges, because of the degeneracy of two adiabatic states. In contrast, a diabatic representation of the states minimizes the change of electronic character and thereby diagonalizes the nuclear kinetic energy operator. Instead the states are coupled through the electronic potential energy. Such *strictly diabatic* representations can only be constructed for electronic states of the same symmetry

in diatomic molecules, though. For polyatomics the representations are at best *quasi-diabatic*, i.e. they nearly diagonalize the nuclear kinetic energy operator [22]. Interestingly, whereas the adiabatic representation is unique, there exist infinitely many (quasi-)diabatic representations [22]. Furthermore, the construction of one such representation, the diabatization procedure, requires knowledge about global properties of the PESs [23]. Since the aim of AIMS is to conduct QMD simulations on polyatomic molecules, such knowledge about the PESs is seldom available nor computationally appealing to obtain for the molecules of interest. Thus, the adiabatic representation of the electronic states is employed in AIMS.

4.1.2 The Nuclear Wave Function and Equations of Motion

The main challenge in the transit from classical to QMD simulations is the nonlocality of the nuclear Schrödinger equation [24]. In principle, to solve the equation the complete global PESs are needed. In practice, it is sufficient to obtain the PESs on multidimensional grids in limited regions of the nuclear configuration space. The nuclear wave function can then be projected on these grids using discrete variable representations [25] and propagated using the time-dependent Schrödinger equation (see e.g. Refs. [24, 26]). Although this approach is very accurate, the number of points on the PESs that have to be calculated scales to the power of the number of nuclear vibrational coordinates, which means that it quickly becomes computationally prohibitively expensive with increasing size of the molecular system under investigation. Thus, it is desirable to adopt an approach that can obtain a more flexible balance between accuracy and number of electronic structure calculations. AIMS achieves this by employing an adaptive time-dependent set of localized nuclear basis functions. The wave function ansatz is

$$\Psi(\mathbf{r}, \mathbf{R}, t) = \sum_I \chi_I(\mathbf{R}, t)\Phi_I(\mathbf{r}; \mathbf{R}) \tag{4.1}$$

where $\mathbf{r}$ indicates the electronic coordinates, $\chi_I(\mathbf{R}, t)$ is the nuclear and $\Phi_I(\mathbf{r}; \mathbf{R})$ the electronic wave function for the Ith electronic state and the semi-colon denotes parametric dependence. Note that AIMS (in principle) can handle an arbitrary number of electronic states and nuclear degrees of freedom. Since each electronic state is associated with its own nuclear wave function, this ansatz is well suited for simultaneous description of nuclear dynamics on vastly different PESs, such as those of bound and repulsive states. Note that while the electronic wave function is time-independent, the nuclear wave function depends on time. This is due to the adaptive size of the set of nuclear basis functions, which is one of the main forces of AIMS. At any given time t in the simulation the number of nuclear basis functions, called *trajectory basis functions* (TBFs), on the electronic state I is $M_I(t)$. The nuclear wave function is expressed as a sum of these TBFs, each associated with a time-dependent complex amplitude

$$\chi_I(\mathbf{R},t) = \sum_{j=1}^{M_I(t)} C_j^I(t)\chi_j^I(\mathbf{R};\overline{\mathbf{R}}_j^I(t),\overline{\mathbf{P}}_j^I(t),\overline{\gamma}_j^I(t),\alpha_j) \tag{4.2}$$

The individual TBFs are defined as products of one-dimensional Gaussian functions

$$\chi_j^I(\mathbf{R};\overline{\mathbf{R}}_j^I(t),\overline{\mathbf{P}}_j^I(t),\overline{\gamma}_j^I(t),\alpha_j) = e^{i\gamma_j^I(t)}\prod_{\rho=1}^{3N}\chi_{\rho_j}^I(R_\rho;\overline{R}_{\rho_j}^I(t),\overline{P}_{\rho_j}^I(t),\alpha_{\rho_j}) \tag{4.3}$$

$$\chi_{\rho_j}^I(R;\overline{R}_{\rho_j}^I(t),\overline{P}_{\rho_j}^I(t),\alpha_{\rho_j}) = \left(\frac{2\alpha_{\rho_j}}{\pi}\right)^{\frac{1}{4}}\exp\Big[-\alpha_{\rho_j}\big(R-\overline{R}_{\rho_j}^I(t)\big)^2 + i\overline{P}_{\rho_j}^I(t)\big(R-\overline{R}_{\rho_j}^I(t)\big)\Big] \tag{4.4}$$

where the index ρ runs over the $3N$ nuclear coordinates of an N atom molecule, which typically [3] and also in this work are chosen to be the Cartesian coordinates. In this work we will use a brief notation not including the parametric dependence of the time-dependent center positions, momenta, phases and fixed widths ($\overline{R}_{\rho_j}^I(t)$, $\overline{P}_{\rho_j}^I(t)$, $\overline{\gamma}_j^I(t)$ and α_{ρ_j}, respectively).

The use of complex Gaussian functions in the definition of the nuclear basis functions is inspired by the pioneering work of Heller [27]. He showed that the time-evolution of the classical parameters (position and momentum) of such Gaussian wave packets on a single PES may be described by Hamilton's equations of motion (including up to second order terms in a local Taylor expansion of the PES) and noted [27]

> ...a point in phase space, representing the center of the wave packet, executing a classical trajectory; this point is "clothed" by a Gaussian function containing the information about the quantum part of the problem.

This is exactly the appealing property of AIMS: it maintains a classical flavour that eases the interpretation of the results, while still ensuring a correct description of quantal behavior. In AIMS the parameters of the Gaussians are propagated similarly to the equations of motion that Heller derived [27], with the exception of the widths that are assumed time-independent [3]. This assumption is rigorously correct for harmonic separable PESs in which the width is well-defined [27]. Recently, a method for optimizing the width parameters in the general case was published, and it was found that the simulation results were relatively independent of the specific values [16]. The benefit of using the classical equations of motion is that energies and gradients of the PESs are only needed at the center of each TBF, which minimizes the number of electronic structure calculations dramatically as compared to the grid methods described above: in AIMS these properties are calculated 'on the fly' when needed. A similar approach using Gaussian basis functions is applied in the G-MCTDH method [28–31].

Note that AIMS converges to an exact solution of the time-dependent nuclear Schrödinger equation in the limit of an infinite number of TBFs if interference is

taken into account through coupled propagation of their complex amplitudes $C_j^I(t)$. This has been validated numerically for small systems [5, 32]. The equations of motion for the amplitudes [3] are derived by substituting the wave function ansatz in the time-dependent Schrödinger equation. On the other hand, when propagating a single TBF on a single PES AIMS reduces to a classical simulation [3]. Thus, AIMS spans the entire range from a purely classical to a full quantum mechanical description. AIMS can then be tuned to the problem at hand while balancing the desired accuracy with the required number of computationally expensive electronic structure calculations. At this point it is worth mentioning a very common approximation made in AIMS simulations in which the $M_I(t = 0)$ initial TBFs are assigned an initial amplitude of one and propagated independently. However, any TBFs spawned during the simulation can still interfere with each other and their parent, and this "independent first generation" (IFG) approximation [3, 7] therefore only amounts to the initial (first generation) TBFs. The IFG approximation greatly limits the amount of coupled propagation and is therefore often employed in situations where the PESs are not known beforehand and electronic structure calculations have to be done on the fly. The assumption behind the approximation is that the importance of interference between TBFs on a single PES is negligible and so can be ignored at the benefit of significantly reduced computational effort.

4.1.3 Non-Adiabatic Dynamics: Spawning New Basis Functions

One of the core forces of AIMS is the time-dependent adaptive size of the nuclear basis set: it is kept minimal and expanded only when the molecular dynamics demands it. Such situations occur when the wave packet encounters a region of the PES where quantum effects such as tunneling and non-adiabatic dynamics cause it to bifurcate. In AIMS this is modeled by expanding the basis set in what is called a *spawning* event. In the following we will discuss spawning in the context of non-adiabatic dynamics. Since each TBF is associated with one particular electronic state, it requires the creation (spawning) of new TBFs to describe an electronic transition, i.e. population transfer from one state to another. In the decision on when to spawn AIMS relies on a measure called *the effective coupling* between two electronic states I and J

$$\Lambda_{IJ}^{\text{eff}} = |\dot{\mathbf{R}} \cdot \vec{\lambda}_{IJ}| \qquad \vec{\lambda}_{IJ} = \langle \Phi_I | \frac{\partial}{\partial \mathbf{R}} | \Phi_J \rangle \tag{4.5}$$

Note the similarity of $\Lambda_{IJ}^{\text{eff}}$ to the denominator of the Massey parameter presented in Eq. (2.2). Using $\hbar\Lambda_{IJ}^{\text{eff}}$ as the denominator of the Massey parameter and replacing $\vec{q}$ by $\mathbf{R}$ can be viewed as a generalization of the one-dimensional Landau–Zener model to multiple nuclear coordinates, where it is taken into account that the nuclei do not necessarily move parallel to the non-adiabatic coupling vector. In that picture the transition probability will increase when the effective coupling increases, illustrating the reason behind using the latter as a measure of when to spawn new TBFs.

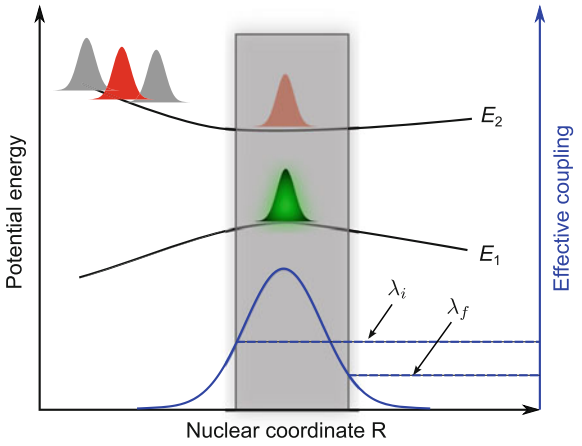

Fig. 4.1 Illustration of the elements of the spawning algorithm used to expand the nuclear basis set in AIMS when modeling non-adiabatic dynamics. A given TBF (*red*) is propagated on the E_2 PES coupled to the rest of the TBFs (*gray*). Once it enters a region of large non-adiabatic coupling (*shaded area*), defined by λ_i, spawning of a predefined number of TBFs (in this case only one, *green*) on the E_1 PES can occur until the region is left, defined by λ_f. Note that the situation $\lambda_i > \lambda_f$ is shown as an example, but that relation is not a requirement. See text for further details

In practice, the spawning algorithm works as illustrated in Fig. 4.1. At each time step in the simulation the effective coupling is calculated for every TBF in the wave packet. Whenever the value of $\Lambda_{IJ}^{\text{eff}}$ is larger than the threshold parameter λ_i a region of large non-adiabatic coupling has been entered and the parent TBF is allowed to spawn new basis functions. At this point the parent TBF is propagated according to Hamilton's equation of motion uncoupled from the rest of the TBFs of the wave packet, i.e. without propagating the complex amplitudes. This uncoupled propagation is stopped when the effective coupling has decreased below a second threshold parameter λ_f, that indicates that the parent TBF has left the region of non-adiabatic coupling. Within that region a predetermined number of basis functions are spawned with zero amplitude and each of them are propagated back in time to the beginning of the region. Then the coupled propagation, that can transfer amplitude (i.e. population) between the TBFs, is started again and continued until one of the TBFs reaches another coupling region. The details of the spawning procedure also involve determination of the initial position and momentum for each of the spawned TBFs, which will not be discussed here. To avoid unnecessary spawning, initial test simulations monitoring the magnitude of the non-adiabatic coupling are run, and the threshold parameters λ_i and λ_f for the real simulation are set such that only regions of increased non-adiabatic coupling are captured as spawning regions. Additional precautions to prevent uncontrollable growth of the basis set have been taken [3], but will not be discussed here.

Finally, it should be noted that the spawning algorithm is best suited for situations in which the non-adiabatic coupling is large and localized spatially or temporally

(in the sense that the TBFs spend little time near regions of large coupling) as e.g. near CIs. This will lead to infrequent events transferring large amount of population between electronic states. Cases in which the coupling is small and delocalized lead to frequent events transferring little population. Using the spawning algorithm outlined above this can result in an explosive increase in the number of TBFs ultimately leading to a breakdown of the simulation. Recently, Ben-Nun and Martínez suggested an alternative spawning algorithm to alleviate the problem [32].

4.1.4 Conducting an AIMS Simulation

To fully simulate a pump-probe experiment the interactions between the electric fields of the pump as well as the probe pulse and the molecule have to be taken into account. But if the pulse durations are very short as compared to the nuclear dynamics, it seems reasonable to neglect the time-dependence of the intensity of the pulses. Indeed it can be shown mathematically that if the temporal profile of the pulse intensity can be approximated by a δ-function, the wave packet created on the excited state by absorption of the pump pulse is a copy of the ground state wave function, scaled by the transition dipole moment (p. 397, Chapter 13 in Ref. [33]). Furthermore, the Condon approximation stating that the transition dipole moment is independent of the nuclear coordinates works well in the limited region covered by the ground state wave function. We will employ both approximations and thus, in the simulations conducted in this work the initial wave packet on the excited-state PES equals the ground state nuclear wave function excited by the pump pulse (since we do not attempt to calculate absolute quantities, the amplitude scaling is not important). In AIMS different ways of approximating this wave function have been applied, but most often and also in this work it is approximated by a number of TBFs generated from a vibrational Wigner distribution in a harmonic approximation [34, 35] as described in the following. For the $v = 0$ vibrational level of a harmonic oscillator with frequency ω and reduced mass m the Wigner distribution takes the following form [34]

$$\Gamma_W^{\text{H.O.}}(R, P) = \frac{1}{\pi\hbar} \exp\left(-\frac{m\omega}{\hbar} R^2 - \frac{P^2}{m\hbar\omega} \right) \tag{4.6}$$

By performing a calculation of normal modes with associated frequencies and reduced masses, the phase-space distribution function for the entire molecule can be expressed as the product of the Wigner distributions for each normal mode. In this work the initial position and momentum of each TBF is determined by sampling a $(\mathbf{R}, \mathbf{P})$ point from this distribution using a Monte-Carlo sampling procedure [36].

Whether the IFG approximation is applied or not an AIMS simulation is conducted by propagating a number $M_I(t = 0)$ of initial TBFs on the electronic state I excited by the pump pulse. This number is increased until convergence with respect to the expectation value of interest (in many cases the electronic state populations)

is obtained. The magnitude of $M_I(t = 0)$ depends on the molecule, excited state and molecular property of interest; in the acetone simulations 13 initial TBFs were sufficient.

A major part of conducting an AIMS simulation is of course analysis of the results. As noted above, the classical flavour of AIMS eases the interpretation of the results in the sense that the position centers of the TBFs reflect the nuclear motions in a comprehensible way. Since this thesis will only describe an example of how simulation results are analyzed in the context of the acetone simulation in Chap. 5 the reader is referred to Ref. [3] for a thorough description of the principles of AIMS data analysis.

4.2 Theoretical Framework for Signal Simulation

We will in the following employ the adiabatic representation of the electronic states. In the interest of brevity of the equations, unless otherwise stated, the total wave function is expressed as a product of an electronic part and a nuclear part, but the results can easily be generalized to the more realistic case of wave functions expressed as linear combinations of such products.

In a photoionization experiment the differential signal expressed in Eq. (2.7) describes the projection of the wave packet $\Psi(\mathbf{r}, \mathbf{R}, t) = \Phi(\mathbf{r}; \mathbf{R}, t)\chi(\mathbf{R}, t)$ on the ionization continuum $\Psi_+(\mathbf{r}, \mathbf{R}) = \Phi_+(\mathbf{r}; \mathbf{R})\chi_+(\mathbf{R})$

$$\begin{aligned} S_+(t) &= |\langle \Psi_+ | \vec{E}_{\text{probe}}(\omega) \cdot \vec{\mu} | \Psi(t) \rangle|^2 \\ &= |\langle \chi_+ | \vec{E}_{\text{probe}}(\omega) \cdot \vec{d} | \chi(t) \rangle|^2 \end{aligned} \tag{4.7}$$

in which the electronic photoionization matrix element $\vec{d}$ was defined as

$$\vec{d} = \langle \Phi_+ | \vec{\mu} | \Phi(t) \rangle \tag{4.8}$$

The section will start with a detailed review of this matrix element followed by a discussion of the theoretical framework used in this work to simulate the signals from TRMS and TRPES experiments.

4.2.1 The Electronic Photoionization Matrix Element

We will employ the same approach as Patchkovskii et al. [37, 38] and consider a singlet spatially non-degenerate n-electron neutral state I described by the wave function Φ_I. The electrons are described by the set $\{x\}_n$ of space-spin coordinates $x_i = (\vec{r}_i, \sigma_i), i = 1, \ldots, n$. Consider the case in which photoionization of I produces a spatially non-degenerate doublet cation state and a free electron. The wave function describing this state can be expressed as [37, 38]

$$\Phi_+(\{x\}_n) = \hat{A}\frac{1}{\sqrt{2}}\big(\Phi_\alpha(\{x\}_{n-1})\varphi_\beta(x_n) - \Phi_\beta(\{x\}_{n-1})\varphi_\alpha(x_n)\big) \tag{4.9}$$

where φ_σ is the continuum wave function of the free electron with $\alpha = \uparrow$ or $\beta = \downarrow$ spin. The $(n-1)$-electron wave functions $\Phi_{\alpha,\beta}(\{x\}_{n-1})$ are the degenerate doublet components of the cation. The anti-symmetrizer $\hat{A}$ is defined as $(1-\sum_{j=1}^{n-1}\hat{P}_{jn})/\sqrt{n}$, where $\hat{P}_{jn}$ permutes electron j and n in its operand. It should be noted that the single-determinant ansatz of Φ_+ neglects dynamical correlation between the free electron and the cation. This is analogous to the single-configuration Hartree–Fock (HF) approach of electronic structure theory [39, 40], and the ansatz can thus be improved by including more configurations in the definition of $\Phi_+(\{x\}_n)$ in the same way the HF description is improved by e.g. configuration interaction methods [41].

Remembering that the dipole operator is given by $\hat{\mu} = e\sum_{i=1}^{n}\vec{r}_i$, where e is the electron charge, the matrix element $\vec{d}$ representing the dipole-transition from Φ_I to Φ_+ can now be expressed as

$$\begin{aligned}
\vec{d} &= e\left\langle \Phi_I \left| \sum_{i=1}^{n}\vec{r}_i \right| \Phi_+ \right\rangle \\
&= \frac{e}{\sqrt{2n}}\left\langle \Phi_I \left| \sum_{i=1}^{n}\vec{r}_i \right| \left(1 - \sum_{j=1}^{n-1}\hat{P}_{jn}\right)(\Phi_\alpha\varphi_\beta - \Phi_\beta\varphi_\alpha) \right\rangle \\
&= \frac{e}{\sqrt{2n}}\left[\left\langle \Phi_I \left| \sum_{i=1}^{n}\vec{r}_i \right| \left(1 - \sum_{j=1}^{n-1}\hat{P}_{jn}\right)\Phi_\alpha\varphi_\beta \right\rangle \right. \\
&\quad \left. - \left(-\left\langle \Phi_I \left| \sum_{i=1}^{n}\vec{r}_i \right| \left(1 - \sum_{j=1}^{n-1}\hat{P}_{jn}\right)\Phi_\alpha\varphi_\beta \right\rangle\right)\right] \\
&= e\sqrt{\frac{2}{n}}\left\langle \Phi_I \left| \sum_{i=1}^{n}\vec{r}_i \right| \left(1 - \sum_{j=1}^{n-1}\hat{P}_{jn}\right)\Phi_\alpha\varphi_\beta \right\rangle \\
&= e\sqrt{2n}\left\langle \Phi_I \left| \sum_{i=1}^{n}\vec{r}_i \right| \Phi_\alpha\varphi_\beta \right\rangle
\end{aligned} \tag{4.10}$$

in which it was exploited in line 3 and 5 that the electrons are indistinguishable, which following the Pauli principle [42] means that Φ_I changes sign when two electrons are interchanged. In line 5 this reveals that all the terms in the last sum are identical. Note that an analogous result would be obtained in the case of the free electron having α spin. Thus, from here on the specific designation of spin will be skipped and replaced by the composite indices F and η representing the quantum numbers describing the state of the cation and the free electron, respectively. From now on, we will include these indices as subscripts on $\vec{d}$. As it will turn out, it is convenient to split the expression into two parts [37, 38], again by exploiting the indistinguishability of the electrons

$$\vec{d}_{IF\eta} = e\sqrt{2n}\left(\langle\Phi_I|\vec{r}_n|\Phi_F\varphi_\eta\rangle - \langle\Phi_I|\sum_{i=1}^{n-1}\vec{r}_n\hat{P}_{in}|\Phi_F\varphi_\eta\rangle\right)$$
$$= e\sqrt{2n}\left(\vec{d}_1 + \vec{d}_2\right) \tag{4.11}$$

in which the one-electron term $\vec{d}_1$ and the exchange term $\vec{d}_2$ were defined as

$$\vec{d}_1 = \langle\psi^D_{IF}|\vec{r}_n|\varphi_\eta\rangle \tag{4.12}$$
$$\psi^D_{IF}(x_n) = \langle\Phi_F|\Phi_I\rangle \tag{4.13}$$
$$\vec{d}_2 = -\sum_{i=1}^{n-1}\langle\Phi_I|\vec{r}_n|\hat{P}_{in}\Phi_F\varphi_\eta\rangle \tag{4.14}$$

4.2.2 Dyson Orbitals

In the commonly applied "sudden ionization approximation" of photoionization [43], in which the electron ejection is assumed to be so fast that it occurs without interaction with the ion core, it has been argued that $\vec{d}_1$ is the only contribution to the transition matrix element [37, 38]. We will employ the same approximation and from now on $\vec{d}_2$ is neglected. The one-electron term $\psi^D_{IF}(x_n)$ that appears in $\vec{d}_1$ is called a *Dyson orbital*, which is constructed from the overlap between the electronic wave functions of the initial and cation states of the system [37, 38, 43, 44]. Dyson orbitals are ionization-channel specific, as indicated by the IF subscript, and the norm of a given Dyson orbital is proportional to the one-electron character of the photoionization transition. Thus, for a given ionization channel the norm of the Dyson orbital is a quantitative measure of the validity of the Koopmans picture (Sect. 3.1.2). In other words, the norm of the Dyson orbital corresponding to ionization of an excited state I to a final state F of the cation, is a measure of the 'strength' of the ionization correlation between I and F. In a HF or similar single-configuration treatment of the electrons the norm of the Dyson orbitals are one and they simply equal the molecular orbitals of the initial (excited) state. For multi-configurational wave functions the shapes of the Dyson orbitals are more complex but still provide a measure of the one-electron character of the ionization transition. As such, the Dyson orbital can be viewed as the wave function of the electron ejected during the photoionization and therefore provides some intuition about the ionization process. The ionization of acetone constitutesan illustrative example; Fig. 4.2 shows calculated Dyson orbitals

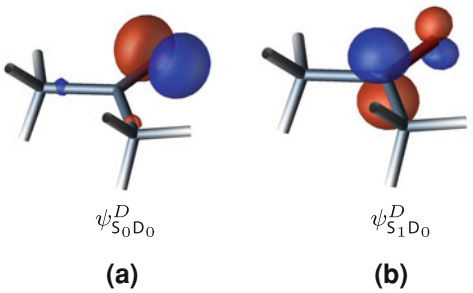

Fig. 4.2 Dyson orbitals corresponding to population of the ground state D_0 of the acetone radical cation by photoionization of **a** the S_0 ground state and **b** the $S_1(n, \pi^*)$ state

corresponding to ionization of the S_0 and the $S_1(n, \pi^*)$ states to the ground state D_0 of the cation. As can be seen, the $\psi^D_{S_0D_0}$ Dyson orbital is equal to the oxygen lone pair orbital, whereas the $\psi^D_{S_1D_0}$ looks like the π^* orbital. Thus, ionization of the ground state removes an electron from the lone pair, whereas the electron is ejected from the π^* orbital when the S_1 state is ionized.

4.2.3 Simulation of Time-Resolved Photoelectron Spectra

To obtain a closer link between QMD simulations and data from time-resolved photoionization experiments it is desirable to be able to calculate the time-resolved photoion and photoelectron yield, preferably energy- or even angle-resolved. Several approaches for such calculations have been suggested [1, 45–50]. As we do not aim to calculate angle-resolved signals, rotational motion is ignored and the state of the free electron is only characterized by its kinetic energy E, which will replace η in the following. Before introducing the formalism used in this work it is appropriate to elaborate slightly on Eq. (4.7)

$$S_{F v_F E}(t) = \left| \langle \chi_{v_F} | \vec{E}_{\text{probe}}(\omega) \cdot \vec{d}_{IFE} | \chi(t) \rangle \right|^2 \tag{4.15}$$

to explicitly indicate that the final state is characterized by the kinetic energy E of the free electron, as well as the cation state described by the indices F and v_F denoting the electronic and vibrational state, respectively. Remember that the neutral electronic state I can change with time as the nuclear wave packet moves along the PESs. In this context it is important to note the functional dependence of $\vec{d}_{IFE}$ on the nuclear coordinates. In the Condon approximation this dependence is assumed to be negligible, and therefore the probability of populating a given vibrational quantum number v_F of the cation is determined by the overlap between $|\chi_{v_F}\rangle$ and the nuclear wave packet $|\chi(t)\rangle$. This is the Franck–Condon picture of a vertical photoionization transition between the neutral and the cation electronic state. As

mentioned earlier these Franck–Condon envelopes of the photoelectron spectra can reveal nuclear dynamics.

Employing the framework used in Refs. [51, 52] the signal can now be reexpressed, while at the same time shedding light on the compact $\vec{E}_{\text{probe}}(\omega)$ notation used in Eq. (4.15) and all previous expressions of the signal. Thus, consider the electric field of the probe pulse

$$\vec{E}_{\text{probe}}(t) = \vec{E}_{\text{probe}} g(t) \cos[\omega_{\text{probe}} t] \tag{4.16}$$

where $\vec{E}_{\text{probe}}$ is the polarization vector, $g(t)$ is the temporal envelope and ω_{probe} is the carrier frequency. Interaction between this field and the nuclear wave packet $|\chi(t)\rangle$ induces a dipole transition to the ionization continuum, creating a new nuclear wave packet $|\chi_{FE}(t)\rangle = (\vec{E}_{\text{probe}}(\omega) \cdot \vec{d}_{IFE})\,|\chi(t)\rangle$ and a photoelectron with kinetic energy E. Applying time-dependent perturbation theory and the approximation that no nuclear dynamics takes place within the duration of the probe pulse, Gräfe et al. derived an expression for $\chi_{FE}(t)$ [52]

$$\chi_{FE}(\mathbf{R}, t) = \left(\vec{E}_{\text{probe}} \cdot \vec{d}_{IFE}(\mathbf{R})\right) f_{IF}(\mathbf{R}, E; \omega_{\text{probe}}) \chi(t) \tag{4.17}$$

$$f_{IF}(\mathbf{R}, E; \omega_{\text{probe}}) = i \int_{-\infty}^{\infty} g(t) e^{i(\text{IP}_{IF}(\mathbf{R}) + E - \hbar\omega_{\text{probe}})t/\hbar} dt \tag{4.18}$$

where $\text{IP}_{IF}(\mathbf{R})$ is the energy difference between the PESs corresponding to the $I \rightarrow F$ ionization channel. The expression for $\vec{E}_{\text{probe}}(\omega)$ is now revealed from Eq. (4.17)

$$\vec{E}_{\text{probe}}(\omega) = \vec{E}_{\text{probe}} f_{IF}(\mathbf{R}, E; \omega_{\text{probe}}) \tag{4.19}$$

and it becomes clear that the earlier mentioned "transition frequency ω", at which the electric field of the probe pulse is Fourier transformed, in the case of a photoionization experiment is given by $\omega = (\text{IP}_{IF} + E)/\hbar$.

It is not the aim of this work to take into account vibrational structure in the photoelectron spectra, and therefore we consider the integral detection case in which the signal is constituted by the contributions from all final states resulting in photoelectrons with kinetic energy E. Exploiting that the vibrational states constitute a complete basis the energy- and time-resolved but state-integrated signal reduces to the norm of $\chi_{FE}(t)$

$$\begin{aligned} S_F(E, t) &= \sum_{v_F} S_{F v_F E}(t) \\ &= \sum_{v_F} |\langle \chi_{v_F} | \chi_{FE}(t) \rangle|^2 \\ &= \langle \chi_{FE}(t) | \chi_{FE}(t) \rangle \\ &= \langle \chi(t) | |\vec{E}_{\text{probe}} \cdot \vec{d}_{IFE}|^2 |f_{IF}|^2 | \chi(t) \rangle \end{aligned}$$

$$= \int W_{IF}(\mathbf{R}, E; \omega_{\text{probe}}) |\chi(\mathbf{R}, t)|^2 d\mathbf{R} \tag{4.20}$$

in which the window function was defined as

$$W_{IF}(\mathbf{R}, E; \omega_{\text{probe}}) = |\vec{E}_{\text{probe}} \cdot \vec{d}_{IFE}(\mathbf{R})|^2 |f_{IF}(\mathbf{R}, E; \omega_{\text{probe}})|^2 \tag{4.21}$$

Thus, Eq. (4.20) expresses the signal as the overlap between the nuclear wave packet density $|\chi(\mathbf{R}, t)|^2$ and the window function. As such the window function describes the range of configurations accessible by the probe pulse. The window is composed of two parts; the left part describing the 'strength' of the dipole transition, sometimes called the electronic factor [17], and the right part that describes the energetics of the photoionization process, taking into account the frequency bandwidth of the probe pulse through the Fourier transform of its temporal profile. As an example a probe pulse with a Gaussian temporal profile results in a window with a Gaussian profile in the kinetic energy domain, centered at the difference between the IP and the probe photon energy.

Tao et al. have recently conducted simulations of time-resolved photoelectron spectra in which they explicitly evaluated the electronic factor [17]. In addition, they conducted simulations in which they approximated the term with the corresponding Dyson orbital norm

$$|\vec{E}_{\text{probe}} \cdot \vec{d}_{IFE}(\mathbf{R})|^2 \approx \langle \psi^D_{IF} | \psi^D_{IF} \rangle \tag{4.22}$$

Comparison of the results obtained in the two cases revealed that the approximation is reasonable [17]. Employing this approximation and inserting the AIMS nuclear wave function (Eq. (4.2)) in Eq. (4.20) gives

$$\begin{aligned} S_F(E, t) = & \sum_I \sum_{i,j=1}^{M_I(t)} C_i^I(t)^* C_j^I(t) \\ & \times \int W_{IF}(\mathbf{R}, E; \omega_{\text{probe}}) \chi_i^I(\mathbf{R}; t)^* \chi_j^I(\mathbf{R}; t) d\mathbf{R} \end{aligned} \tag{4.23}$$

which will be the working equation for simulating time-resolved photoionization signals in the present work.

References

1. Seel, M., Domcke, W.: J. Chem. Phys. **95**, 7806–7822 (1991)
2. Seel, M., Domcke, W.: Chem. Phys. **151**, 59–72 (1991)
3. Ben-Nun, M., Martínez, T.J.: Adv. Chem. Phys. **121**, 439–512 (2002)
4. Ben-Nun, M., Martínez, T.J.: Chem. Phys. Lett. **298**, 57–65 (1998)
5. Ben-Nun, M., Martínez, T.J.: J. Chem. Phys. **108**, 7244–7257 (1998)
6. Ben-Nun, M., Quenneville, J., Martínez, T.J.: J. Phys. Chem. A **104**, 5161–5175 (2000)

7. Hack, M.D., Wensmann, A.M., Truhlar, D.G., Ben-Nun, M., Martinez, T.J.: J. Chem. Phys. **115**, 1172–1186 (2001)
8. Ko, C., Levine, B., Toniolo, A., Manohar, L., Olsen, S., Werner, H.-J., Martínez, T.J.: J. Am. Chem. Soc. **125**, 12710–12711 (2003)
9. Baeck, K.K., Martinez, T.J.: Chem. Phys. Lett. **375**, 299–308 (2003)
10. Choi, H., Baeck, K.K., Martinez, T.J.: Chem. Phys. Lett. **398**, 407–413 (2004)
11. Martínez, T.J.: Acc. Chem. Res. **39**, 119–126 (2006)
12. Coe, J.D.: J. Martínez, T. Mol. Phys. **106**, 537–545 (2008)
13. Ko, C., Virshup, A.M., Martínez, T.J.: Chem. Phys. Lett. **460**, 272–277 (2008)
14. Hudock, H.R., Martínez, T.J.: ChemPhysChem **9**, 2486–2490 (2008)
15. Tao, H., Levine, B.G., Martínez, T.J.: J. Phys. Chem. A **113**, 13656–13662 (2009)
16. Thompson, A.L., Punwong, C., Martínez, T.J.: Chem. Phys. **370**, 70–77 (2010)
17. Tao, H., Allison, T.K., Wright, T.W., Stooke, A.M., Khurmi, C., van Tilborg, J., Liu, Y., Falcone, R.W., Belkacem, A., Martinez, T.J.: J. Chem. Phys. **134**, 244306 (2011)
18. Fuß, W., Schmid, W., Trushin, S.: Chem. Phys. **316**, 225–234 (2005)
19. Schalk, O., Boguslavskiy, A.E., Stolow, A.: J. Phys. Chem. A **114**, 4058–4064 (2010)
20. Roos, B.O.: In: Rice, S.A., Prigogine, I. (eds.) Advances in Chemical Physics, Vol. 69, pp. 399–445. Wiley, New York (1987)
21. Levine, B.G., Coe, J.D., Virshup, A.M., Martínez, T.J.: Chem. Phys. **347**, 3–16 (2008)
22. Mead, C.A., Truhlar, D.G.: J. Chem. Phys. **77**, 6090–6098 (1982)
23. Ruedenberg, K., Atchity, G.J.: J. Chem. Phys. **99**, 3799–3803 (1993)
24. Kosloff, R.J.: Phys. Chem. **92**, 2087–2100 (1988)
25. Light, J.C., Hamilton, I.P., Lill, J.V.: J. Chem. Phys. **82**, 1400–1409 (1985)
26. Kosloff, R.: Annu. Rev. Phys. Chem. **45**, 145–178 (1994)
27. Heller, E.J.: J. Chem. Phys. **62**, 1544–1555 (1975)
28. Burghardt, I., Meyer, H.-D., Cederbaum, L.S.: J. Chem. Phys. **111**, 2927–2939 (1999)
29. Worth, G.A., Burghardt, I.: Chem. Phys. Lett. **368**, 502–508 (2003)
30. Burghardt, I., Nest, M., Worth, G.A.: J. Chem. Phys. **119**, 5364–5378 (2003)
31. Burghardt, I., Giri, K., Worth, G.A.: J. Chem. Phys. **129**, 174104 (2008)
32. Ben-Nun, M., Martínez, T.J.: Isr. J. Chem. **47**, 75–88 (2007)
33. Tannor, D.J.: Introduction to Quantum Mechanics—A Time-Dependent Perspective. University Science Books, Sausalito (2007)
34. Brown, R.C., Heller, E.J.: J. Chem. Phys. **75**, 186–188 (1981)
35. Davis, M.J., Heller, E.J.: J. Chem. Phys. **80**, 5036–5048 (1984)
36. Levine, B.G., Martínez, T.J.: J. Phys. Chem. A **113**, 12815–12824 (2009)
37. Patchkovskii, S., Zhao, Z., Brabec, T., Villeneuve, D.M.: Phys. Rev. Lett. **97**, 123003–123007 (2006)
38. Patchkovskii, S., Zhao, Z., Brabec, T., Villeneuve, D.M.: J. Chem. Phys. **126**, 114306 (2007)
39. Fock, V.Z.: Phys. A: Hadrons Nucl. **61**, 126–148 (1930)
40. Roothaan, C.C.J.: Rev. Mod. Phys. **23**, 69–89 (1951)
41. Sherrill, C.D.; Schaefer III, H.F.: In: Löwdin, P.-O., Sabin, J.R., Zerner, M.C., Brändas, E. (eds.) Advances in Quantum Chemistry, Vol. 34, pp. 143–269. Academic Press, New York (1999)
42. Pauli, W.Z.: Phys. A: Hadrons Nucl. **31**, 765–783 (1925)
43. Pickup, B.T.: Chem. Phys. **19**, 193–208 (1977)
44. Oana, C.M., Krylov, A.I.: J. Chem. Phys. **127**, 234106 (2007)
45. Meier, C., Engel, V.: J. Chem. Phys. **101**, 2673–2677 (1994)
46. Arasaki, Y., Takatsuka, K., Wang, K., McKoy, V.: Chem. Phys. Lett. **302**, 363–374 (1999)
47. Batista, V.S., Zanni, M.T., Greenblatt, B.J., Neumark, D.M., Miller, W.H.: J. Chem. Phys. **110**, 3736–3747 (1999)
48. Suzuki, Y., Stener, M., Seideman, T.: J. Chem. Phys. **118**, 4432–4443 (2003)
49. Hudock, H.R., Levine, B.G., Thompson, A.L., Satzger, H., Townsend, D., Gador, N., Ullrich, S., Stolow, A., Martínez, T.J.: J. Phys. Chem. A **111**, 8500–8508 (2007)

50. Arasaki, Y., Takatsuka, K., Wang, K., McKoy, V.: J. Chem. Phys. **132**, 124307 (2010)
51. Møller, K.B., Henriksen, N.E., Zewail, A.H.: J. Chem. Phys. **113**, 10477–10485 (2000)
52. Gräfe, S., Scheidel, D., Engel, V., Henriksen, N.E., Møller, K.B.: J. Phys. Chem. A **108**, 8954–8960 (2004)

Chapter 5
Simulation: The Norrish Type-I Reaction in Acetone

In the following the theoretical framework introduced in the previous chapter is applied to a real case of ultrafast organic photodynamics: the Norrish Type-I reaction in acetone. Particular attention is payed to how the wave packet dynamics is expressed in the time-resolved photoionization signal and it will become clear that a close connection between theory and experiment is crucial for even a qualitatively correct interpretation of experimental results. The simulations presented in this chapter have been published in Ref. I.

5.1 Motivation

As mentioned in the introduction the aim of ultrafast spectroscopy it to shed light on the interplay between the flow of charge and energy and nuclear reaction dynamics; the intrinsic molecular properties defining the very heart of chemistry. An example of such interplay is the photoinduced C–C bond breakage observed in ketones when exposed to UV light, called the Norrish Type-I reaction [1]. The chromophore responsible for the UV absorption is the C=O double bond, yet the reactive site is the α-C–C bond, immediately raising the question on how the absorbed photon energy is distributed from the chromophore to the reactive site. Being a model system for ketone photodynamics, acetone has been subjected to a wide variety of experimental and theoretical studies of the Norrish Type-I reaction [2–10]. Ab initio calculations show that there is an effectively repulsive surface that leads from the higher lying electronic states (mainly Rydberg states) to an ultrafast bond breakage on the $S_2(n, 3s)$ state through a series of CIs [8]. The mechanism for decomposition from the $S_1(n, \pi^*)$ state was long debated [2–4, 6]. Some authors claimed the dissociation to be ultrafast, commencing directly in the S_1 state, based on the fact that TRMS experiments showed an ultrafast decay of the parent ion [3, 4]. Others believed in ISC to the $T_1(n, \pi^*)$ triplet state in which there is a barrier to dissociation [2, 6]. Through the combined use of TRPES and TRMS it was recently found that

R. Y. Brogaard, *Molecular Conformation and Organic Photochemistry*,
Springer Theses, DOI: 10.1007/978-3-642-29381-8_5,
© Springer-Verlag Berlin Heidelberg 2012

when excited at 253–288 nm the S_1 state is long-lived (> 100 ps) and the ultrafast decay of the parent ion signal was claimed to be due to the wave packet moving out of the Franck–Condon region to the S_1 minimum [9]. This conclusion was supported by recent computational work of Maeda et al. [10] who proposed a mechanism of slow ISC from the S_1 minimum to T_1 followed by decomposition, much like the mechanism proposed earlier [2, 6]. The ISC mechanism is believed to be overtaken by a faster S_1 decomposition at excitation energies above the S_1 dissociation barrier [6, 10]. The aim of this simulation is to gain further insight into which nuclear degrees of freedom are involved in the initial movement of the wave packet out of the Franck–Condon region, and in particular how this influences the TRMS and TRPES signals. We present calculated signals based on AIMS molecular dynamics simulations of acetone excited to the $S_1(n, \pi^*)$ state, including all nuclear degrees of freedom and coupling to the electronic ground state S_0. On the basis of these simulations we discuss the relation between the wave packet dynamics and the temporal evolution of the signal in the previous TRMS and TRPES experiments [9]. This is done using the previously mentioned concept of a probing window describing the range of configurations accessible by the probe pulse (Eq. (4.20), page 48).

5.2 Computational Details

As mentioned in the previous chapter we employed SA-CASSCF for electronic structure calculations. All ab initio calculations were performed without any use of symmetry. Unless otherwise stated SAN-CAS(m, n) will denote SA-CASSCF calculations in which N singlet states are averaged (each with equal weight) using an active space of m electrons in n orbitals. The reader is assumed to be familiar with such calculations and if not Ref. [11] can be consulted.

The results from the AIMS simulation are based on 13 initial TBFs propagated using the IFG approximation. The initial positions and momenta of the TBFs were sampled from the ground state vibrational Wigner distribution as described previously (Eq. (4.6)). The ground state equilibrium geometry and normal mode frequencies used to construct the Wigner distribution, were calculated at the MP2/cc-pVDZ level of theory. The initial TBFs were placed on the $S_1(n, \pi^*)$ state and propagated using a multiple time scale integration scheme, as described by Martínez [12]. A time step of 1.9 fs was employed, but adaptively reduced in case of convergence issues. The simulations were run for roughly 200 fs, significantly longer than the time scale of the experimentally observed ultrafast dynamics of 50 fs. At each time step electronic energies, gradients and non-adiabatic coupling elements were calculated using SA2-CAS(6,5)/6-31+G(d). The SA2-CAS(6,5) calculations included six electrons in an active space consisting of the π orbital of the C=O bond as well as the two oxygen lone pair orbitals, one of which mixed strongly with a σ orbital of the C–C bonds. Furthermore the π^* orbital and a C–C σ^* like orbitals were included. In the Franck–Condon region the natural populations of the σ and σ^* like orbital were very close to 2 and 0, respectively. This shows, as expected, that these orbitals are not

important in the description of the $S_1(n, \pi^*)$ state at the time of excitation. Nevertheless the orbitals were included in the active space to correctly treat a possible C–C bond breakage at later times.

To evaluate the signal as expressed in Eq. (4.23) on page 49, the Dyson orbitals need to be computed. As mentioned earlier, these orbitals are ionization-channel specific and in this work we consider the $\psi^D_{S_1 D_0}$ Dyson orbital corresponding to $S_1 \rightarrow D_0$ ionization, as this was the channel probed in the time-resolved experiments [9]. Dyson orbitals were computed at different nuclear configurations using the SuperDyson code [13]. These calculations were based on SA2-CAS(6,5)/DZP and SA2-CAS(5,5)/DZP wave functions calculated for the S_1 and D_0 state, respectively, where the state-averaging in the latter case is performed over doublet states.

5.3 Results and Discussion

5.3.1 Electronic State Populations

We first consider the non-adiabatic coupling between the S_1 and the S_0 state. The results of test simulations monitoring the magnitude of the non-adiabatic coupling showed that the coupling between S_1 and S_0 was not very pronounced. Even when setting the threshold parameters as low as to observe any significant spawning at all, the amplitudes of the few TBFs spawned in the S_0 state were vanishingly small. Therefore the major part of the TBFs were run with high thresholds to prevent spawning and thereby save computing time. We therefore conclude that there is no $S_1 \rightarrow S_0$ population transfer to the ground state, supporting the claim that bond dissociation takes place after slow ISC to the T_1 state, as proposed earlier [6, 9, 10]. As all TBFs were thus situated in the S_1 state at all times we will in the following equations skip the electronic index I used in the notation of the derivation of the theoretical framework. We further note that since the TBFs were propagated in the IFG approximation, the fact that no spawning was observed means that the TBFs at all times maintained their norm, i.e. $|C_j(t)|^2 = 1$ for all j.

5.3.2 Nuclear Dynamics

Having established that the dynamics involves only the S_1 state (on the time scale of roughly 200 fs that we investigated), we now move on to discuss the nuclear dynamics. Without any prior knowledge about the nuclear wave function, one would calculate expectation values of coordinates such as bond distances and angles coherently, to take overlap between the TBFs into account. We did this for one bond distance (the CO bond, see below), by numerical evaluation of

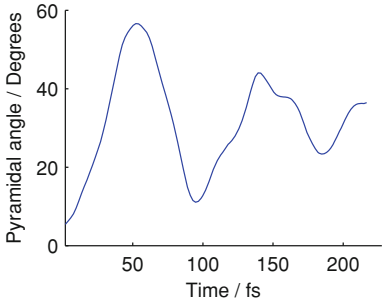

Fig. 5.1 Time-evolution of the average value of the CCCO pyramidal angle of acetone in the $S_1(n, \pi^*)$ state. After excitation there is a significant change along the pyramidalization coordinate which moves the wave packet out of the probing window (see text)

$$\langle\chi(t)|D(\mathbf{R})|\chi(t)\rangle = \sum_{i,j=1}^{M(t)} C_i^*(t)C_j(t)\int \chi_i^*(\mathbf{R};t)D(\mathbf{R})\chi_j(\mathbf{R};t)d\mathbf{R} \tag{5.1}$$

where $D(\mathbf{R})$ is the bond distance operator. In an incoherent evaluation of the expectation value, i.e. including only $i = j$ terms in the sum of Eq. (5.1), the expression reduces to a weighted average of the bond distances of the geometries represented by the TBF centers. In this average the TBFs should be weighted by their norm, but since that is maintained, the incoherent average is a simple classical average where all trajectories are weighted equally. In the test case of the CO bond distance the time-evolution of the expectation value calculated from Eq. (5.1) was identical to within numerical accuracy to the evolution obtained from the classical average over all TBFs. Thus, we chose the latter and much faster way of evaluating the rest of the expectation values.

When exciting the S_1 state, moving a lone pair electron to the π^* orbital, the C=O double bond acquires single bond character. Thus, the central carbon atom changes from an sp^2 to a more sp^3-like hybridization. Therefore one would a priori expect the most prominent change in geometry when leaving the Franck–Condon region to be pyramidalization around the central carbon atom. Figure 5.1 shows the average value of the CCCO pyramidal angle as a function of time, agreeing with the expectation; the wave packet exhibits a pronounced oscillatory motion along the pyramidalization coordinate. For completeness Fig. 5.2 shows the changes in CCO bond angle, CC bond and CO bond length.

As can be seen, the CCO angle reduces a little and the CO distance increases slightly, in agreement with the expected change in hybridization of the central carbon atom. What is more important is that the mean CC bond distance stays nearly constant. Thus, the simulation predicts that the S_1 state is non-reactive; no ultrafast bond breakage is taking place. We note that trajectories propagated for more than 350 fs also do not show any bond breakage. These phenomena, oscillation in the pyramidalization coordinate around the S_1 minimum and no ultrafast bond breakage, support the mechanism recently proposed by Maeda et al. [10].

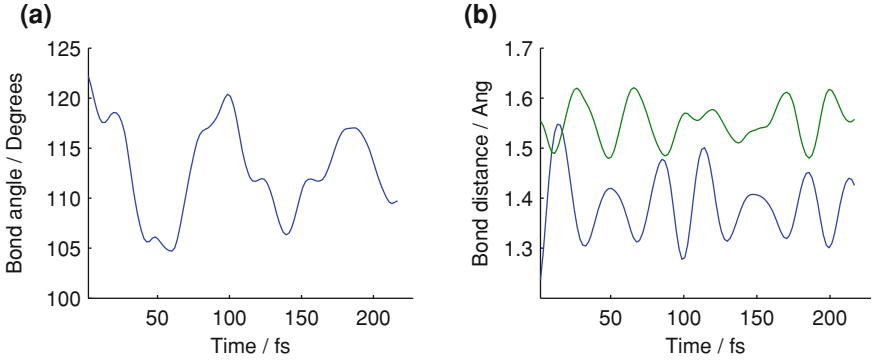

Fig. 5.2 Time-evolution of the average values of selected structural parameters of acetone after excitation to the $S_1(n, \pi^*)$ state. **a** The CCO bond angle. **b** The CO (*blue*) and CC (*green*) bond distances

5.3.3 Simulation of TRMS and TRPES Signals

So far the simulations agree qualitatively with the general mechanism of the photodynamics as proposed by us and others [2, 6, 9, 10]. We now turn to the calculation of TRMS and TRPES signals, to facilitate a more quantitative comparison between the simulations and the <30 fs decay of the S_1 photoelectron signal (as well as the parent ion signal in TRMS) that was measured previously [9]. In idealized TRPES experiments such decay would reflect an electronic transition; in this case IC to S_0 or ISC to T_1. But in the interpretation of the results of the TRPES experiments [9] the S_1 lifetime is significantly longer than 30 fs, and as shown above, the simulations agree with this interpretation. The signal decay is believed to reflect the wave packet leaving a certain probing window of the Franck–Condon region [9]. As such, this is an important example of a TRPES experiment in which a decay in the photoelectron signal is not due to electronic population transfer. Rather, it is nuclear dynamics affecting the probing efficiency of that particular electronic state, as was observed in TRPES experiments on DNA bases [14]. Recently, the discrepancy between the time-resolved photoionization signal decay times and calculated lifetimes of excited-state ethylene was also shown to be due to pure nuclear dynamics causing a decreased probing efficiency [15].

To compute TRMS and TRPES signals we turn to the expression derived in Eq. (4.23) on page 49. Since only (partly) energy-integrated signals will be considered in the present work, the expression reduces to

$$S(t) = \sum_{i,j=1}^{M(t)} C_i(t)^* C_j(t) \int \langle \psi^D_{S_1D_0} | \psi^D_{S_1D_0} \rangle \times W(\mathbf{R}; \omega_{\text{probe}}) \chi_i(\mathbf{R}; t)^* \chi_j(\mathbf{R}; t) d\mathbf{R} \tag{5.2}$$

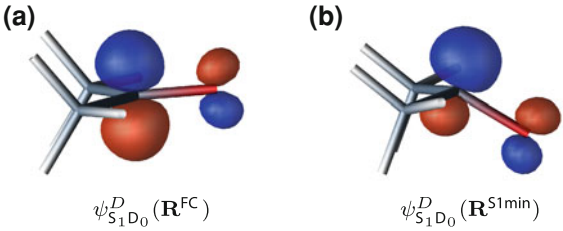

Fig. 5.3 The Dyson orbital for ionization of the S_1 state to the D_0 ion state at the **a** Franck–Condon and **b** S_1 minimum geometry. The norm of the Dyson orbital is virtually identical for the two geometries, indicating that the electronic overlap between the neutral and the ion state is unchanged when the wave packet moves from the Franck–Condon region to the minimum on the S_1 PES

in which the definition of the energy-integrated probing window $W(\mathbf{R}; \omega_{\text{probe}})$ will be presented later. Like any other electronic quantity, the Dyson orbital norm does in principle exhibit a parametric dependence on the nuclear coordinates. To estimate the extent of this dependence the $\psi^{D}_{S_1D_0}$ Dyson orbital was computed at the Franck–Condon geometry and the S_1 minimum geometry, respectively. As can be seen in Fig. 5.3 the orbital is very similar to the π^* orbital of the neutral acetone molecule. This reflects a perfect agreement with the Koopmans picture of ionization, that predicts the removal of the π^* electron in ionization of the $S_1(n, \pi^*)$ state to the D_0 ion state. As can be seen, the Dyson orbital looks qualitatively similar in the two geometries and more importantly the norm changes by less than 5 %. It means that the electronic overlap between the excited state and the cation does not change significantly when the wave packet travels from the Franck–Condon region to the S_1 minimum geometry. This justifies replacing the Dyson orbital norm by a constant factor and we will then turn to the definition of the energy-integrated window $W(\mathbf{R}; \omega_{\text{probe}})$. The range of the window should depend only on the coordinates describing the nuclear motions that are responsible for an increase of the IP. When going from the Franck–Condon to the S_1 minimum geometry of acetone, high level ab initio calculations predict an increase of 1.7 eV in the vertical IP of the S_1 state [9]. Such increase is observed for ionization of a geometry significantly different from the minimum geometry of the ion state created, in the present case D_0 [9]. Optimizing the geometry of the D_0 state at the MP2/cc-pVDZ level of theory revealed a close similarity to the Franck–Condon geometry. As shown above, the most prominent change in geometry when the wave packet leaves the Franck–Condon region, and therefore the change responsible for the IP increase, is along the pyramidalization coordinate. This scenario is sketched in Fig. 5.4. We therefore chose the probing window to depend only on pyramidalization, defined by out-of-plane motion of the three carbons and the oxygen atom. The upper limit for the width of the window can be estimated from the set of values of these four Cartesian coordinates (R_1, R_2, R_3, R_4) for which the IP fulfills the inequality

$$\text{IP}^{\text{FC}} \leq \text{IP}(R_1, R_2, R_3, R_4) \leq \varepsilon_{\text{probe}} \tag{5.3}$$

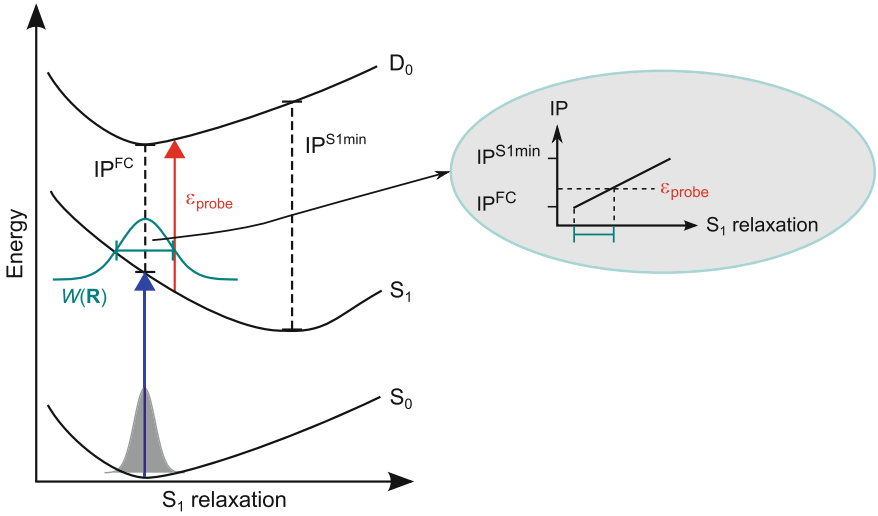

Fig. 5.4 Sketch of the time-resolved photoionization experiment on acetone. The pump pulse (*blue arrow*) prepares a wave packet in the Franck–Condon region of the S_1 state, which then travels to the S_1 minimum. The accompanying increase of IP causes the wave packet to move out of the probing window $W(\mathbf{R})$ of configurations detectable by the probe pulse. In the TRMS experiment the probing window can be defined as the nuclear configurations for which the IP is less than the total probe photon energy $\varepsilon_{\text{probe}}$. This coordinate space is determined by assuming a linear dependence of the IP on the nuclear coordinates (illustrated in the *right* part of the figure)

since, when the IP exceeds the total probe photon energy $\varepsilon_{\text{probe}}$ (the experiment employed two-photon probing) ionization is no longer possible, as sketched in Fig. 5.4. This window would govern the time evolution of the acetone molecular ion signal in the TRMS experiment. In the signal obtained from the TRPES experiment the window width was smaller, since the transient was obtained by integrating an energy interval around a peak in the photoelectron spectrum [9]. In that case, the upper limit in Eq. (5.3) would be $\varepsilon_{\text{probe}} - E_{\text{min}}$, where E_{min} is the lower limit of the interval. Below we will compare how the choice of these two window widths—representing either the TRMS or the TRPES signal—influenced the simulated signal $S(t)$. We have chosen an E_{min} value that gives a TRPES window width of 0.1 eV. The TRMS window has a width of 0.56 eV (corresponding to the difference between IP^{FC} and $\varepsilon_{\text{probe}}$). For convenience we chose the functional form of the window to be a product of Gaussians in the out-of-plane Cartesian coordinate of each of the four aforementioned heavy atoms. The width of the Gaussians are defined so that Eq. (5.3) is fulfilled within the fwhm. This was done by assuming a linear dependence of the IP on the nuclear coordinates. Within this assumption the fwhm of the Gaussian describing the TRMS probing window extent in the coordinate R_i is given by

$$\text{fwhm}_i = \frac{\varepsilon_{\text{probe}} - \text{IP}^{\text{FC}}}{\text{IP}^{\text{S1min}} - \text{IP}^{\text{FC}}} |R_i^{\text{FC}} - R_i^{\text{S1min}}| \tag{5.4}$$

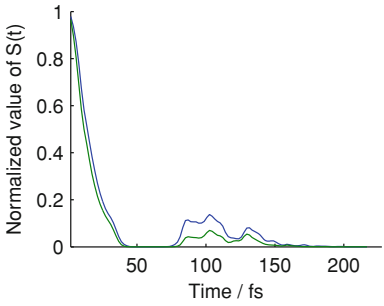

Fig. 5.5 Time-evolution of the signal $S(t)$ corresponding to the TRMS (*blue*) and TRPES (*green*) windows, relating the simulated results to the previously recorded TRMS and TRPES data on acetone [9]. The initial ultrafast decay of less than 20 fs agrees well with the experimental observations

where R_i^{FC} and R_i^{S1min} are the values at the Franck–Condon and S_1 minimum geometry, respectively. The corresponding fwhm of the TRPES probing window is derived by replacing $\varepsilon_{\mathrm{probe}}$ with $\varepsilon_{\mathrm{probe}} - E_{\mathrm{min}}$, according to the discussion above. From this construction of the window function and the definition of the TBFs (Eq. 4.3) the simulated signal can be expressed as

$$\begin{aligned} S(t) &= \sum_{i,j=1}^{M(t)} C_i^*(t) C_j(t) \int W(\mathbf{R}; \omega_{\mathrm{probe}}) \chi_i^*(\mathbf{R}; t) \chi_j(\mathbf{R}; t) d\mathbf{R} \\ &= \sum_{i,j=1}^{M(t)} e^{i(\gamma_j(t) - \gamma_i(t))} C_i^*(t) C_j(t) \\ &\quad \times \prod_{\rho=1}^{3N} \int w_\rho(R) \chi_{\rho_i}^*(R; t) \chi_{\rho_j}(R; t) dR \end{aligned} \tag{5.5}$$

where the $M(t) = 13$ TBFs are averaged coherently, and $w_\rho(R)$ are the above mentioned Gaussians for the coordinates representing pyramidalization and constant values of 1 for the rest of the nuclear coordinates. The normalized $S(t)$ corresponding to the TRMS and TRPES window widths is shown in Fig. 5.5 (we note that the computed signals were identical to within numerical accuracy, when the averaging of the TBFs was done incoherently). As can be seen, both functions decay to zero within less than 50 fs in an almost identical manner, agreeing with the identical decay times obtained when fitting the TRMS and TRPES data [9]. This illustrates that even though the probing windows in the TRMS and TRPES experiments are different, what both experiments capture is the wave packet leaving the Franck–Condon region. The decays can be fit to a Gaussian decay of 12–13 fs agreeing well with the 18 fs obtained from the fits of the experimental data [9]. Monoexponential fits give similar decay times to within 1–2 fs, but the fits are poor and illustrate a case where first order kinetics is a poor model of the dynamics, as discussed earlier. In fact, in cases such as the present, in which the experimental signal reflects the wave packet moving out of a certain probing window in the Franck–Condon

region, the signal decay is closely related to the initial decay of the autocorrelation function, which is near Gaussian [16]. The partial revival of the $S(t)$ function around 100 fs is due to the pyramidalization vibration that brings the molecule back to an almost planar configuration, as can also be seen from Fig. 5.1. Due to the wider window, this revival is more pronounced in the simulated TRMS signal than it is in the TRPES signal. Still, with an amplitude of 10% (or less) of the maximum signal it is not possible to judge whether this feature is present in the TRMS and TRPES data on acetone [9], due to a limited signal-to-noise ratio. We conclude that from the point of view of the experiment, in which a limited subset of configurations near the Franck–Condon region can be probed, the wave packet leaves the Franck–Condon region, travels towards the S_1 minimum and does not return. Interestingly, this would not a priori be the conclusion when considering Fig. 5.1 that shows a quite pronounced pyramidalization vibration which could be thought to give rise to pronounced revivals in the experimental signal. This result shows the importance of realizing, both in experimental and theoretical work, that in the probing step of the experiment the wave packet is projected onto a template that is only sensitive to certain degrees of freedom and furthermore only to a certain extent. This can be pictured in a simplified manner as watching the molecular photodynamics taking place on a stage on which the lighting is such that only a limited region in the space of molecular configurations is lighted, and only dynamics bringing the molecule into that particular region is observed. In the case of acetone photodynamics, the molecule quickly moves out of the lighted region when the pyramidalization is activated and the subsequent vibration takes place in the dark.

5.4 Conclusion

We have shed light on the initial ultrafast dynamics of the Norrish Type-I reaction in acetone and provided a detailed comparison with previous TRPES and TRMS experiments on the reaction [9]. Based on the experiments it was suggested that within the first 30 fs after excitation, the wave packet moves out of the Franck–Condon region and travels to the S_1 minimum. No ultrafast bond breakage or transition to the ground state was observed and the lifetime of the S_1 state was more than 100 ps. Thus, it is likely that dissociation takes place in the T_1 state. This assignment was supported by the present AIMS simulations providing a complete description of the initial photodynamics. Furthermore, by simulating TRMS and TRPES signals we obtained a measure of the timescale on which the wave packet leaves the probing window, thus providing a more detailed comparison between the simulations and the experiments. The simulated decay time, 12 fs, agrees quite well with the experimental value of 18 fs [9]. We explain the decay of the experimental TRMS and TRPES signal to be due to an increased IP caused by a large difference in geometry between the D_0 and the S_1 minimum. As such this is an important example of a case in which decay of a photoelectron signal is not due to electronic population transfer, but relaxation to the excited state minimum, as has also been observed by Hudock et al. [14] and

Tao et al. [15]. We expect such a phenomenon to be present in many experiments probing valence states like the $S_1(n, \pi^*)$ state of acetone in which the minimum geometry of the excited state is significantly different from that of the ion state created. The results of this work stress the importance of pursuing a close relation to the experiment, when molecular dynamics simulations are used as a supplement in the interpretation of time-resolved experiments. The molecular dynamics do not necessarily explain the experimental signal unless the probing step is taken into account in the simulations.

References

1. Gilbert, A., Baggott, J.: Chapter 7: photochemical reactions of the carbonyl chromophore. In: Gilbert, A., Baggott, J. (eds.) Essentials of Molecular Photochemistry, pp. 288–301. Blackwell Scientific Publications, Oxford (1991)
2. Shibata, T., Suzuki, T.: Chem. Phys. Lett. **262**, 115–119 (1996)
3. Zhong, Q., Poth, L., Castleman, A.W. Jr.: J. Chem. Phys. **110**, 192–196 (1999)
4. Owrutsky, J.C., Baronavski, A.P.: J. Chem. Phys. **110**, 11206–11213 (1999)
5. Farmanara, P., Stert, V., Radloff, W.: Chem. Phys. Lett. **320**, 697–702 (2000)
6. Diau, E.W.-G., Kötting, C., Zewail, A.H.: Chem. Phys. Chem. **2**, 273–293 (2001)
7. Sølling, T.I., Diau, E.W.-G., Kötting, C., Feyter, S.D., Zewail, A.H.: Chem. Phys. Chem. **3**, 79–97 (2002)
8. Diau, E.W.-G., Kötting, C., Sølling, T.I., Zewail, A.H.: Chem. Phys. Chem. **3**, 57–78 (2002)
9. Rusteika, N., Møller, K.B., Sølling, T.I.: Chem. Phys. Lett. **461**, 193–197 (2008)
10. Maeda, S., Ohno, K., Morokuma, K.: J. Phys. Chem. Lett. **1**, 1841–1845 (2010)
11. Roos, B.O.: In: Rice, S.A., Prigogine, I. (eds.) Advances in Chemical Physics, vol. 69, pp. 399–445. Wiley, Chichester (1987)
12. Levine, B.G., Martínez, T.J.: J. Phys. Chem. A **113**, 12815–12824 (2009)
13. SuperDyson. Fortran90 code for calculating Dyson orbitals from small CI expansions. Made by Dr. Serguei Patchkovskii, Steacie Institute for Molecular Sciences, National Research Council Canada, Ottawa
14. Hudock, H.R., Levine, B.G., Thompson, A.L., Satzger, H., Townsend, D., Gador, N., Ullrich, S., Stolow, A., Martínez, T.J.: J. Phys. Chem. A **111**, 8500–8508 (2007)
15. Tao, H., Allison, T.K., Wright, T.W., Stooke, A.M., Khurmi, C., van Tilborg, J., Liu, Y., Falcone, R.W., Belkacem, A., Martinez, T.J.: J. Chem. Phys. **134**, 244306 (2011)
16. Heller, E.J.: Acc. Chem. Res. **14**, 368–375 (1981)

Part III
Experiments

Chapter 6
Experimental Setups

This chapter describes the experimental setups used to conduct the time-resolved photoionization experiments in the project. Some experiments were carried out in the Molecular Photonics Group at the Steacie Institute for Molecular Sciences, National Research Council Canada, in Ottawa and others in the Femtolab, Department of Chemistry, University of Copenhagen. The next two sections will describe the setups used in the two laboratories. All of the used techniques are available in several other international laboratories, why the setups in view of brevity of the thesis will be fairly briefly described. Where appropriate the reader is referred to previously published work for details.

Fundamentally, setups for conducting fs time-resolved photoionization experiments on gaseous samples consist of; a fs laser system, a sample of cold molecules and a charged-particle detection scheme for ions and/or electrons. Whereas the laser systems used in Ottawa and Copenhagen are quite similar, the sample preparation and detection schemes exhibit fundamental differences that will be described and discussed in the following.

6.1 Femtolab Copenhagen

The experimental setup in Copenhagen is used to record time-resolved photoelectron and mass spectra. In the following sections the laser system and the spectrometer are described.

6.1.1 Laser System

The laser setup used in Copenhagen is sketched in Fig. 6.1. The fs laser system consists of a Ti:Sapphire oscillator (Spectra Physics, Tsunami, 80 MHz, 800 nm,

R. Y. Brogaard, *Molecular Conformation and Organic Photochemistry*,
Springer Theses, DOI: 10.1007/978-3-642-29381-8_6,
© Springer-Verlag Berlin Heidelberg 2012

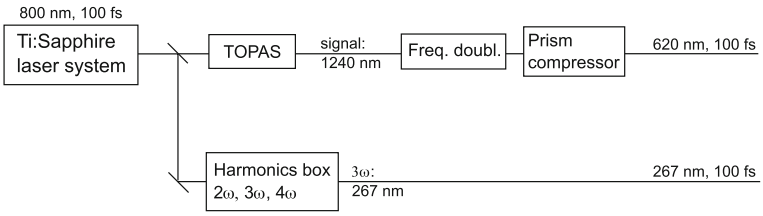

Fig. 6.1 Schematic overview of the laser setup in Copenhagen. Indicated are the wavelengths and outputs used in the experiments conducted in this project. Pulse durations are fwhm values

70 fs fwhm) pumped by a Nd:YLF diode laser (Spectra Physics, Millennia). The output of the oscillator is amplified by a Ti:Sapphire regenerative amplifier (Spectra Physics, Spitfire, 1 kHz, 100 fs fwhm, 1.0 W) pumped by a Nd:YLF laser (Spectra Physics, Empower). The output of the amplifier is used to pump an optical parametric amplifier (TOPAS-C, Light Conversion) as well as a home built setup ('Harmonics box') used to generate up to the fourth harmonic of the fundamental frequency.

Pump Pulses The experiments conducted in Copenhagen used $\lambda_p = 267$ nm laser pulses for the pump step. They were generated as the third harmonic of the fundamental by collinear sum frequency mixing of the second harmonic and the fundamental ('Harmonics box' in Fig. 6.1).

Probe Pulses Laser pulses with a center wavelength of $\lambda_e = 620$ nm were used in the probe step of the experiment. They were generated by frequency doubling of the signal output from the TOPAS. The pulses were passed through a single-pass prism compressor, which sole purpose in the present case was to filter out residual intensity at longer wavelengths. The probe was delayed with respect to the pump pulse by a computer-controlled motorized delay stage. The pulses were combined to collinear propagation (not shown in the figure) using dichroic mirrors transmitting the probe and reflecting the pump. At the reaction chamber (Fig. 6.2) the pulses were focused into the interaction region by a concave Al mirror.

6.1.2 The Time-of-Flight Spectrometer and Continuous Inlet System

The time-of-flight (TOF) photoelectron and mass spectrometer used in Copenhagen has been described thoroughly in the literature [1]. The apparatus is sketched in Fig. 6.2. This project involves liquid samples, but the inlet system can handle solid and gaseous samples as well. In the case of liquid samples a mixture of carrier gas and sample vapor is created by bubbling He gas (typically at 0.3 bar) through the sample (not shown in the figure). The gas mixture is expanded through a conical nozzle (Ø100 μm) in the vacuum source chamber. During this adiabatic expansion the

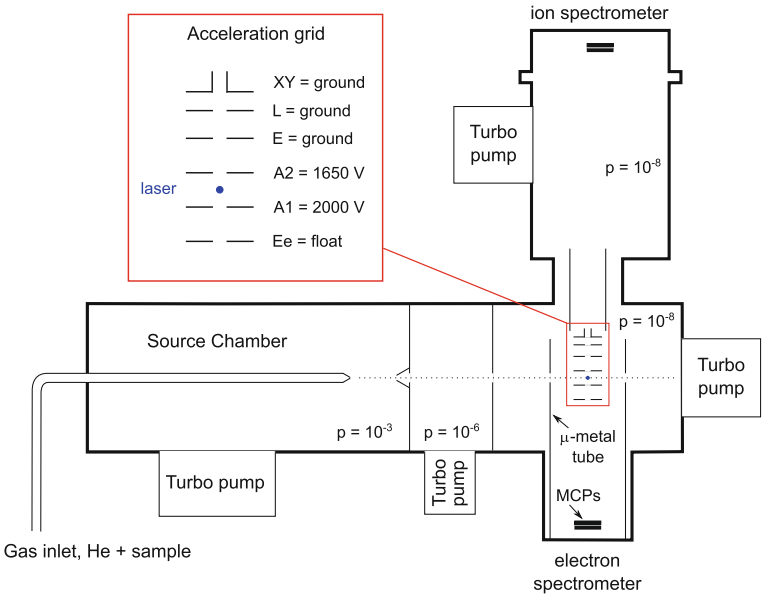

Fig. 6.2 Schematic overview of the molecular beam TOF spectrometer in Copenhagen. Dimensions are not to scale. Typical pressures (order of magnitude) in the chambers at operating conditions are stated in mbar. The inset shows the voltages applied to the acceleration plates when the apparatus is used for mass spectrometry. When used for photoelectron spectroscopy all plates are grounded

heavy sample molecules are accelerated to the speed of the light carrier gas atoms and cooled down vibrationally and rotationally by soft collisions with the atoms. A skimmer (Ø200 μm) placed approximately 1 cm in front of the nozzle leads to the formation of a beam of molecules entering the next chamber. In the expansion process the sample molecules can reach speeds exceeding the local speed of sound and therefore the beam is called a *supersonic molecular beam* [2]. Such beams are excellent sources of cold molecules; rotational temperatures below 0.5 K have been reached [3]. The cooling also affects the nozzle itself, so in the experiments conducted in this project the nozzle was heated to 70–80 °C to prevent condensation of sample in the opening. From the differentially pumped chamber the molecular beam passes through a pinhole (Ø1 mm) to the interaction chamber, where it is intersected at right angle by the laser beams.

In the interaction region electrons and cations are generated by photoionization of the cold molecules and the apparatus can detect both charged species, although not in coincidence but operated as a photoelectron or a mass spectrometer, respectively. When used for mass spectrometry, voltages are applied to the acceleration plates as shown in the inset of Fig. 6.2 to extract the cations that then move upwards through the flight tube into the ion spectrometer. Placed at the top of the spectrometer is an ion detector consisting of a set of chevron-stacked microchannel plates (MCPs) operated at negative voltage. Notice that the flight path from the interaction region

to the MCPs is not at right angle to the molecular beam. The MCPs are placed a little off-axis to account for the velocity component of the ions in the propagation direction of the molecular beam. When an ion hits the detector it generates a small negative DC voltage (∼70 mV) signal in the anode that is sent to a time digitizer card (FAST ComTec, P7888-2(E)) in a computer (not shown in the figure). By feeding the card with a trigger signal from the laser clocking each laser pulse, the computer can measure the TOF spectrum of the ions generated in the interaction region at each laser shot. Assuming a uniform electric field from the acceleration grid the TOF of an ion with mass to charge ratio m/z is given by

$$t_{\mathrm{TOF}}^{\mathrm{ion}} = l\sqrt{\frac{m}{2zV_{\mathrm{ext}}}} + L_{\mathrm{i}}\sqrt{\frac{m}{2zV_{\mathrm{acc}}}} \tag{6.1}$$

where l is the length of the acceleration region, V_{ext} is the extraction potential (in this case $V_{\mathrm{A1}} - V_{\mathrm{A2}} = 350$ V, see inset of Fig. 6.2), L_{i} is the length of the field-free ion flight path and V_{acc} is the acceleration potential (in this case $V_{\mathrm{A2}} = 1650$ V). The first and second term is the time spent in the acceleration and the field-free region, respectively. Note that what the computer acquires is a spectrum of ion hits as a function of time t after the trigger signal. Thus, $t_{\mathrm{TOF}}^{\mathrm{ion}} = t - t_0$, where t_0 is the actual time of ionization with respect to the trigger signal. Taking this into account and condensing all the constants of Eq. (6.1) into a single spectrometer constant K, the TOF is converted to mass to charge ratio as $m/z = K(t - t_0)^2$. The mass spectrometer is calibrated by determining the parameters K and t_0 from ion TOF spectra of samples with known mass spectra, typically *N,N*-dimethylisopropylamine (DMIPA) and acetone.

When the apparatus is used as a photoelectron spectrometer all acceleration plates are grounded. The μ-metal tube shields the interaction region and the electron spectrometer from the earth magnetic field to (ideally) achieve a field-free environment for the electrons. Another set of chevron-stacked MCPs operated at positive voltage is placed at the bottom of the photoelectron spectrometer. Also the anode is at high positive voltage, meaning that the electron signal is formed at high DC potential. Thus, the anode is decoupled from the following timing electronics using capacitive decoupling. The decoupled negative DC voltage signal (∼40 mV) is passed through an amplifier (Phillips Scientific, Model 6954 B 100). The amplified signal (∼350 mV) is sent to the time digitizer card mentioned above and the TOF spectrum of the electrons is measured in the same way as for the ions. Conversion of TOF to kinetic energy of the photoelectrons is done using

$$E = \frac{A}{(t_{\mathrm{TOF}}^{\mathrm{e}})^2} - E_0 \quad A = \frac{L_{\mathrm{e}}^2}{2m_{\mathrm{e}}} \quad t_{\mathrm{TOF}}^{\mathrm{e}} = t - t_0 \tag{6.2}$$

where L_{e} is the electron flight path, and it is taken into account that the electrons can acquire a small amount of kinetic energy E_0 due to contact potentials from the acceleration grid or other small deviations from the ideal field-free

environment. The photoelectron spectrometer is calibrated by determining the parameters A, E_0 and t_0 from electron TOF spectra of samples with known photoelectron spectra containing sharp peaks, usually Xe and/or DMIPA. Typical values of $|E_0|$ are 0–0.2 eV. When transforming the TOF spectrum $S(t^{\mathrm{e}}_{\mathrm{TOF}})$ to a kinetic energy spectrum $S(E)$ the Jacobian is taken into account to get the correct shape of the spectrum

$$S(E) = S(t^{\mathrm{e}}_{\mathrm{TOF}}(E)) \left| \frac{dt^{\mathrm{e}}_{\mathrm{TOF}}}{dE} \right| = S(t^{\mathrm{e}}_{\mathrm{TOF}}(E)) \cdot \frac{(t^{\mathrm{e}}_{\mathrm{TOF}}(E))^3}{2A} \tag{6.3}$$

Note that this scaling is not necessary in the conversion of an ion TOF spectrum to a mass spectrum, because it consists of (practically) discrete peaks as opposed to the finite width peaks constituting the photoelectron TOF spectrum.

When doing photoelectron spectroscopy with laser beams at wavelengths in the UV range, electrons ejected by scattered photons hitting surfaces in the spectrometer can constitute a considerable background. The main measure taken to reduce this background is to minimize the number of scattered photons. This is done by using a high quality CaF_2 optic (CVI Melles-Griot, excimer-grade) as spectrometer entrance window for the laser beams. Furthermore, an iris placed in the reaction chamber minimizes the number of scattered photons reaching the spectrometer. Despite these measures, scattered photons will reach the spectrometer, the surfaces of which are therefore made from materials with high work functions. Thus, the acceleration grid is made from oxidized Molybdenum and all stainless steel surfaces near the interaction region are coated with Aerodag®.

Time-resolved photoelectron and mass spectra are automatically recorded by a LabVIEW program that repeats the procedures outlined above for a series of delays between the pump and probe pulses. The in situ temporal cross correlation of the pump and probe pulses, that constitutes the instrument response function needed for fitting the experimental data (Eq. (3.1), page 28), is determined from the pump–probe signal of a molecular or atomic species in which the center wavelengths of both pulses are non-resonant. Typically, Xe or DMIPA is used. Depending on the number of photons needed to ionize the species, this procedure determines a $\mathrm{fwhm}_{\mathrm{cc}}$ value of an $[X,Y']$ temporal cross correlation. By assuming identical temporal widths of the pump and probe pulses, $\mathrm{fwhm}_{\mathrm{cc}}$ can be reduced or increased to reflect the instrument response function of the $[A,B']$ process that creates the signal in the experiment.

6.2 Molecular Photonics Group

The experimental setup in Ottawa is used to record time-resolved photoelectron spectra. In the following sections the laser system and the spectrometer are described.

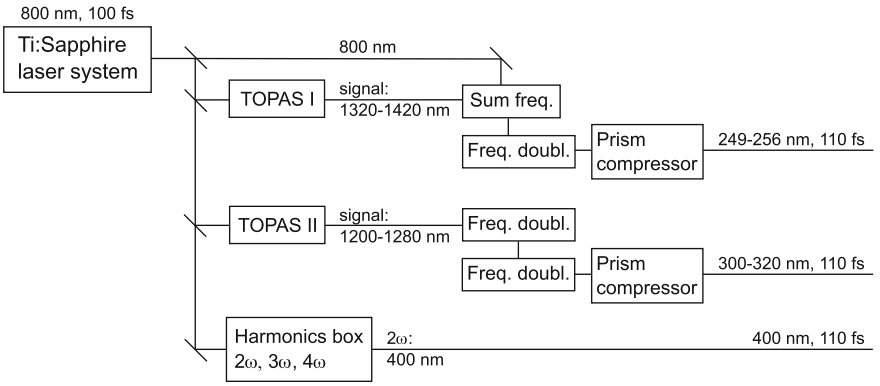

Fig. 6.3 Schematic overview of the laser setup in Ottawa. Indicated are the wavelength ranges and outputs used in the experiments conducted in this project. Pulse durations are fwhm values

6.2.1 Laser System

The laser setup used in Ottawa is sketched in Fig. 6.3. The fs laser system consists of a Ti:Sapphire oscillator (Spectra Physics, Tsunami, 80 MHz, 800 nm, 80 fs fwhm) pumped by a Nd:YLF diode laser (Spectra Physics, Millennia). The output of the oscillator is amplified by a Ti:Sapphire regenerative amplifier (Coherent, Legend, 1 kHz, 100 fs fwhm, 2.4 W) pumped by two Nd:YLF lasers (Positive Light, Evolution). The output of the amplifier is used to pump two optical parametric amplifiers (TOPAS, Light Conversion) as well as a home built setup ('Harmonics box') used to generate up to the fourth harmonic of the fundamental frequency.

Pump Pulses Laser pulses of center wavelengths ranging from $\lambda_p = 248$ nm to $\lambda_p = 320$ nm were used in the pump step of the experiments. Pulses with center wavelengths of 249–256 nm were generated by non-collinear sum frequency mixing of the fundamental with the signal output of a TOPAS, followed by frequency doubling. Pulses with center wavelengths of 300–320 nm were generated as the fourth harmonic of the signal output of a second TOPAS. In both cases any linear frequency chirp of the laser pulses acquired due to group velocity dispersion in the optical elements in the beam path was compensated for using a double pass prism compressor.

Probe Pulses All experiments conducted in Ottawa used $\lambda_e = 400$ nm probe pulses, generated by frequency doubling of the fundamental (the 'Harmonics box' in Fig. 6.3). The probe was delayed with respect to the pump pulse by a computer-controlled motorized delay stage. The pulses were combined to collinear propagation using dichroic mirrors transmitting the probe and reflecting the pump. At the reaction chamber (see description in Sect. 6.2.2) the pulses were focused mildly into the interaction region by a concave Al mirror.

6.2.2 The Magnetic Bottle and Pulsed Inlet System

The apparatus used in Ottawa has been described in detail in Ref. [4] and Fig. 6.4 shows a schematic overview of the apparatus inspired by a figure from that paper. The apparatus consists of a source chamber separated from the interaction chamber by a gate valve. The source chamber is pumped by four oil diffusion pumps backed by a roots blower. In the source chamber is placed a 1 kHz pulsed valve (Even-Lavie) [3] with a 250 μm diameter conical nozzle [5], through which a mixture of gaseous sample and He carrier gas (typically at a pressure of 4 kTorr) is expanded in vacuum, creating a molecular beam as described above, the main difference being that in this case the beam is pulsed. In this apparatus two skimmers are placed in the molecular beam path from the nozzle to the interaction region. For samples with significant vapor pressures (on the order of 10 Torr or more) at room temperature the mixing of sample vapor and carrier gas can be done outside the source chamber. But the samples used in this project are solid and very non-volatile. Thus, the solid samples were placed in a cartridge inside the body of the pulsed valve. By heating the body of the valve to 110–120 °C sublimation was induced and the sample vapor seeded in He carrier gas passed through the valve. But due to the expansion the front of the valve was cooler than the rest, which lead to condensation of solid sample in the nozzle. These problems were alleviated by attaching a home built heater and a thermocouple sensor to the front of the valve, and keeping that part about 20 °C warmer than the body of the valve.

In the interaction region, the molecular beam is crossed at right angle by the laser beams. To achieve synchronization between the arrival of the laser pulses and the molecular beam pulse, the pulsed valve receives its trigger signal from a digital delay generator (Stanford Research Systems, DG-535) that is synchronized to the laser system. The delay between the laser signal and the valve trigger signal is optimized on the experimental signal on a day-to-day basis, since it depends on carrier gas pressure, valve opening time (typically 12–15 μs) and the general condition of the valve.

The details of the magnetic bottle detection technique can be found in the literature [4, 6, 7], and only a brief description will be given here. While the technique is also based on TOF measurement, the collection efficiency of a magnetic bottle can reach values close to 50%, which is far better than the field-free TOF spectrometer described above. The reason is that whereas the field-free TOF spectrometer only collects the electrons within the small solid angle covered by the detector, the magnetic bottle collects nearly all electrons emitted in the upper hemisphere of the interaction volume. This is achieved by employing a strong magnetic field ($B_i = 1$ T) in the interaction region, that gradually changes to a constant weak field ($B_f = 10$ G) guiding the electrons to an MCP detector. The gradual change in the magnetic field strength from B_i to B_f means that for each electron the speed is maintained $|\vec{v}_i| = |\vec{v}_f|$, but the transversal components of the initial velocity $\vec{v}_i$ are drastically reduced as the electron executes a spiraling motion on its way towards the detector. This is illustrated in the inset of Fig. 6.4. Instead of installing a μ-metal tube as in the

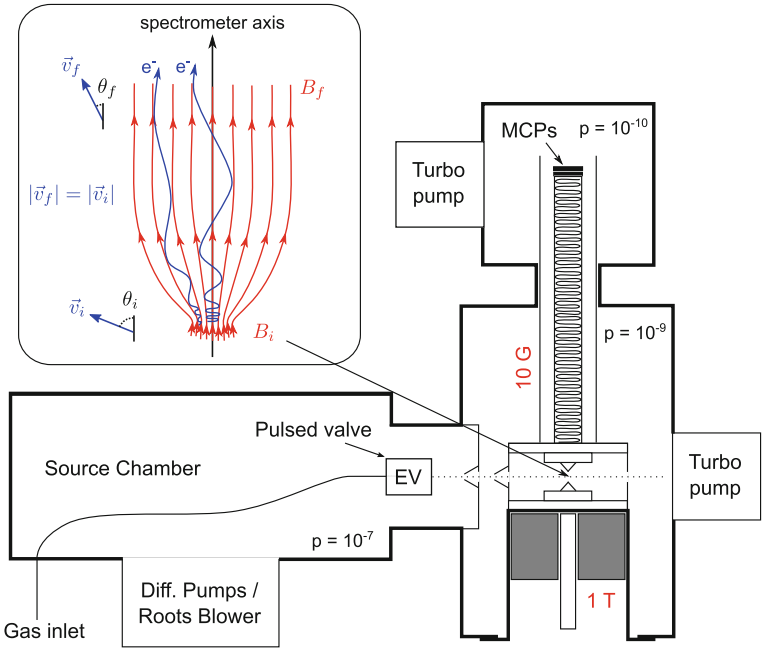

Fig. 6.4 Schematic overview of the molecular beam magnetic bottle apparatus in Ottawa. Typical pressures (order of magnitude) in the chambers at operating conditions are stated in mbar. Dimensions are not to scale. The inset is largely inspired from Fig. 15 in Ref. [6] and illustrates the magnetic field lines and electron paths of the magnetic bottle

TOF spectrometer in Copenhagen, the magnetic bottle spectrometer in Ottawa is surrounded by two sets of Helmholtz coils (not shown in the figure) to compensate for the earth magnetic field. The operation of the electron detector and handling of the signal is done similarly to the procedure described for the field-free TOF spectrometer. Calibration of the magnetic bottle spectrometer and transformation of the TOF spectrum to a kinetic energy spectrum is done exactly as described above. Usually, the well-known vibrationally resolved photoelectron spectrum of NO [8] is used for the calibration.

Time-resolved photoelectron spectra are automatically recorded by a LabVIEW program controlling the delay between the pump and probe pulses. The instrument response function is determined in the same way as outlined for the Copenhagen spectrometer, typically using NO or 1,3-butadiene.

References

1. Rusteika, N.: Computational and experimental investigation of ultrafast photodissociation in isolated organic molecules: understanding the effects of femtosecond laser excitation. Ph.D. thesis, University of Copenhagen (2009)
2. Scoles, G.: Atomic and Molecular Beam Methods, vol. 1, 2. Oxford University Press, New York (1988, 1992)
3. Even, U., Jortner, J., Noy, D., Lavie, N., Cossart-Magos, C.:J. Chem. Phys. **112**, 8068–8071 (2000)
4. Lochbrunner, S., Larsen, J., Shaffer, J., Schmitt, M., Schultz, T., Underwood, J., Stolow, A.:J. Electron Spectrosc. Relat. Phenom. **112**, 183–198 (2000)
5. Hillenkamp, M., Keinan, S., Even, U.:J. Chem. Phys. **118**, 8699–8705 (2003)
6. Hertel, I.V., Radloff, W.: Rep. Prog. Phys. **69**, 1897–2003 (2006)
7. Kruit, P., Read, F.H.:J. Phys. E: Sci. Instrum. **16**, 313–324 (1983)
8. Jarvis, G.K., Evans, M., Ng, C.Y., Mitsuke, K.:J. Chem. Phys. **111**, 3058–3069 (1999)

Chapter 7
Paracyclophanes I: [2+2]cycloaddition of Ethylenes

This chapter presents the first of two studies of photochemical reaction dynamics. The first section reviews the fundamental issue related to studying bimolecular reactions with fs time-resolution. This is followed by a presentation of the time-resolved investigation of the [2+2]cycloaddition reaction, which was published in Ref. II. The experiments were carried out on the magnetic bottle spectrometer in Ottawa (Sect. 6.2.2). Readers interested in specific experimental parameters not mentioned in this thesis are referred to the paper.

7.1 Studying Bimolecular Reaction Dynamics with Femtosecond Time-Resolution

The general scope of the thesis encompasses the study of (the influence of conformation in) bimolecular reaction dynamics and during the project much effort has been spent on such investigations. To get the cleanest possible picture of a bimolecular reaction free of solvent effects the ultimate goal is to conduct the time-resolved experiment on isolated molecules in the gas phase. The problem is that the rate of collision of molecules in the gas phase is low, meaning that for an ensemble of molecules the time zero of a bimolecular reaction cannot be defined with fs time-resolution. Scherer et al. [1, 2] pioneered a very elegant solution to this problem in which they kept the reactants together in a van der Waals complex, an approach that has later been pursued by other groups as well [3–5]. In this project we have taken a slightly different approach in which the reactants are connected to a molecular scaffold. From synthesis of a series of compounds Hopf and coworkers have shown that the [2.2]paracyclophane is a well suited scaffold to study interaction between functional groups, [6] and therefore disubstituted [2.2]paracyclophanes have been chosen as model systems for our investigations of (pseudo)bimolecular reaction dynamics.

R. Y. Brogaard, *Molecular Conformation and Organic Photochemistry*,
Springer Theses, DOI: 10.1007/978-3-642-29381-8_7,
© Springer-Verlag Berlin Heidelberg 2012

7.2 Motivation

The most common excited-state reaction in DNA is the formation of the cyclobutane pyrimidine dimer in a [2+2]cycloaddition between adjacent thymine bases, [7, 8] a mutation that can lead to skin cancer [9, 10]. This reaction has been studied by Schreier et al. [11] in an all-thymine oligodeoxynucleotide using fs time-resolved infrared spectroscopy, revealing that the reaction is complete within 1 ps. Such a high reaction rate would be lethal to DNA if all adjacent thymine bases underwent [2+2]cycloaddition. This is obviously not the case and the remarkably low quantum yield for this reaction is explained by a conformational restriction: a reactive conformation of the thymine bases before light absorption is crucial for inducing the ultrafast mutagenic cycloaddition [11].

In this work we aim for a better understanding of photoinduced [2+2]cycloaddition dynamics, especially with respect to the relation between the ground state conformation prior to light absorption and the resulting excited-state reactivity. We have chosen pseudo-*gem*-divinyl[2.2]paracyclophane (GEM-V), shown in Fig. 7.1, as a model system for the [2+2]photocycloaddition. As shown in the figure, the molecule can in principle exist in three different conformers depending on the relative orientation of the vinyl groups: the anti-anti, syn-syn and syn-anti conformers. In benzene solution the molecule cyclizes quantitatively upon irradiation by a UV lamp and even when left in diffuse daylight [6]. As is indicated in Fig. 7.1 the cyclized product is formed only by the anti-anti conformer. Thus, GEM-V seems to be a good candidate for comparing the excited-state dynamics of two different types of conformers: one that is suited for [2+2]cycloaddition and one that is not. We have also studied the isomeric pseudo-*para*-divinyl[2.2]paracyclophane (PARA-V) shown in Fig. 7.1. In PARA-V the vinyl groups are placed such that the [2+2]cycloaddition cannot take place. PARA-V thus serves as an non-reactive reference compound for comparison with GEM-V.

7.3 Results

7.3.1 Ab Initio Calculations

Pseudo-*gem*-divinyl[2.2]paracyclophane (GEM-V)

The optimized geometry of the anti-anti conformer of GEM-V is shown in Fig. 7.2. Note that the molecule does not possess C_s symmetry; the two halves are twisted, reducing the symmetry to C_1. This distortion was also observed in previous computational and experimental studies of [2.2]paracyclophane [12–14]. An important point to notice is that the vinyl groups are twisted by 26 degrees out of the plane of the phenyl rings. The twist angles in the syn-anti conformer (not shown) are similar.

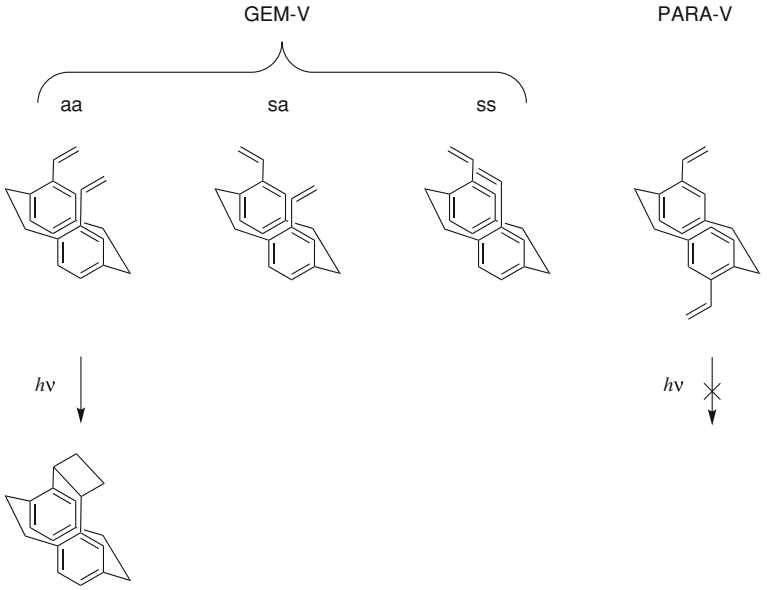

Fig. 7.1 The anti-anti (aa), syn-anti (sa) and syn-syn (ss) conformers of pseudo-*gem*-divinyl[2.2]paracyclophane (GEM-V). Only the anti-anti conformer reacts in a photoinduced [2+2]cycloaddition. Also shown is the non-reactive reference compound pseudo-*para*-divinyl[2.2]paracyclophane (PARA-V)

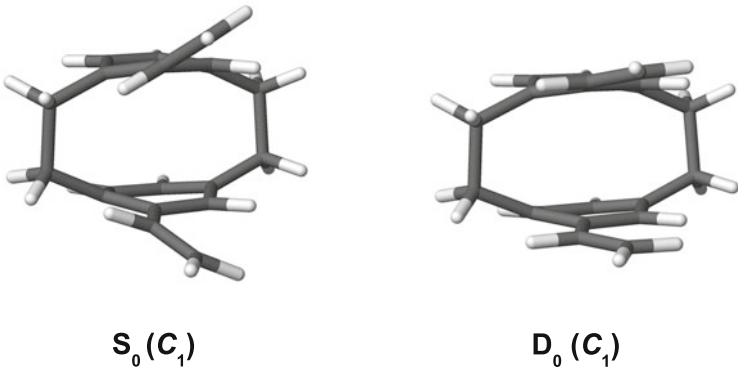

Fig. 7.2 B3LYP/6-31G(d) optimized geometries of the anti-anti conformer of GEM-V in the ground neutral (S_0) and cation ground state (D_0)

It would be desirable to be able to calculate the heats of formation of the anti-anti and syn-anti geometries and on the basis thereof predict a ratio of the anti-anti to syn-anti conformers. But this would require calculation of heats of formation within chemical accuracy, which to the best of our knowledge is not possible for molecules

Table 7.1 RI-CC2/cc-pVDZ excitation energies of GEM-V (anti-anti (aa) and syn-anti (sa) conformers) and PARA-V compared to experimental values obtained from the gas phase absorption spectra Ref. II

	GEM-V			PARA-V	
	Calc. aa	Calc. sa	Exp.	Calc.	Exp.
S_1 (π, π^*)	4.17	4.17	4.0	4.15	4.0
S_2 (π, π^*)	4.38	4.38	4.3	4.40	4.3
S_3 (π, π^*)	4.59	4.66	5.0	4.64	5.0

Values are in eV

as large as the paracyclophanes. Furthermore, this ratio ($\sim$3:1) is available from X-ray diffraction measurements of the solid sample Ref. II. If the conformers would equilibrate after sublimation of the sample from the crystalline phase, the ratio could change in the gas phase. Based on the calculation of the vinyl twist transition state involved in the conversion between the anti-anti and syn-anti conformer, we find that the barrier in electronic energy on the B3LYP/6-31G(d) level is 10 kJ/mol, which is considerably more than $RT = 3.3$ kJ/mol at 120 °C—the temperature at which the samples are sublimated. Thus, we believe that the conformer ratio present in the crystal will be preserved in the gas phase after sublimation.

In the cation ground state equilibrium structure (see Fig. 7.2) the vinyl groups are almost in plane with the ring, the twist angle being reduced to 7 degrees. The difference in these twist angles between the ground and ionic states is expected to result in an extended Franck–Condon progression in the photoelectron spectrum as was previously observed for substituted styrenes [15].

To explore the electronic character of the excited states in the Franck–Condon region, vertical excitations of the anti-anti and syn-anti conformer were calculated. The calculated excitation energies are shown in Table 7.1, together with approximate experimental values obtained from the maxima in the gas phase absorption spectra Ref. II. The reader is referred to Heilbronner and Yang [16] for a thorough description of the electronic structure of paracyclophanes. The orbitals involved in the most important configurations in the description of the lowest excited states of the anti-anti conformer are shown in Fig. 7.3. The orbitals of the syn-anti conformer are very similar. From the perspective of the individual halves of the molecule, calculations predict the S_1 state to be quite similar to the S_1 state of styrene, with HOMO-1→LUMO and HOMO→LUMO+1 being the most important configurations [17]. The S_2 state is described by numerous configurations and no simple characterization can be made. The S_3 state is mainly a HOMO→LUMO excitation. Note that in the HOMO there is a nodal plane between the styrene units in the occupied orbitals which is not present in the LUMO. Furthermore, as can be seen from the perspective of the ethylene groups the HOMO→LUMO excitation is analogous to the $\pi \rightarrow \pi^*$ excitation that leads to ethylene dimerization. Thus, we expect the HOMO→LUMO excitation to describe the diabatic state that is reactive in the [2+2]cycloaddition.

According to the Woodward-Hoffmann rules pericyclic reactions that are forbidden in the ground state are allowed in the excited state (see e.g. Ref. [18] and

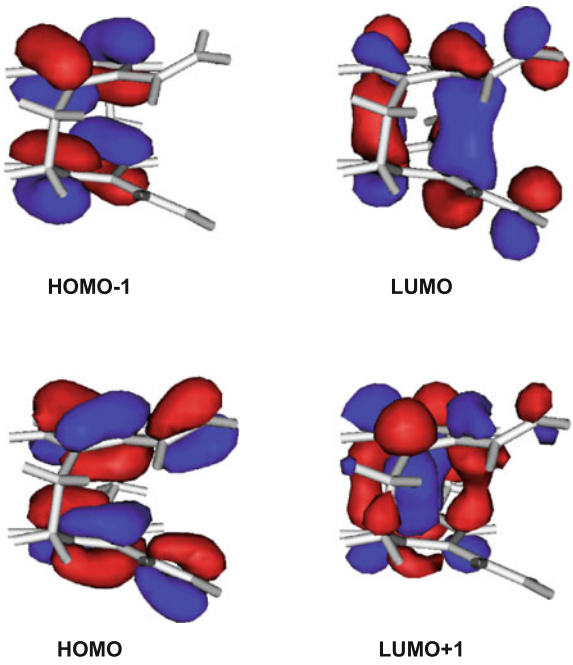

Fig. 7.3 RI-CC2/cc-pVDZ orbitals calculated at the Franck–Condon geometry in the anti-anti conformer of GEM-V

references therein). In the case of ethylene dimerization, computations do indeed predict the pericyclic reaction to occur through a CI between S_1 and S_0 [18, 19]. Therefore, a search for a MECI between S_1 and S_0 leading to [2+2]cycloaddition was conducted at the SA2-CAS(4,4)/6-31G(d) level of theory. The resulting geometry and branching space vectors are shown in Fig. 7.4. The geometry is quite similar to the corresponding geometry at the MECI calculated for ethylene dimerization [18, 19]. The major difference is the asymmetry present in the C–C distances of the forming single bonds, 1.98 and 2.55 Å, compared to the value of 2.19 Å computed for the ethylene dimerization [19]. Considering a more dynamical aspect of the [2+2]cycloaddition in GEM-V, following the gradient difference and derivative coupling vectors towards the CI primarily leads to an approach of the outer C–C-pair in the forming cyclobutane ring, which further emphasizes the asymmetry of the reaction. The asymmetry is most likely due to the presence of the rigid paracyclophane scaffold that makes it unfavourable to obtain a geometry with symmetrical C–C bond distances. This implies that the bond formation in the [2+2]reaction in GEM-V is asymmetrical, which in the most extreme case would mean that the reaction is not concerted, but stepwise with a biradical intermediate in the ground state. It was not possible to locate such an intermediate, though, as SA2-CAS(4,4) geometry optimization started close to the CI clearly converged towards the cyclobutane product.

Figure 7.5 shows the quasi-diabatic potential energy curves along an interpolated [2+2]cycloaddition reaction path in the anti-anti conformer of GEM-V. The path was

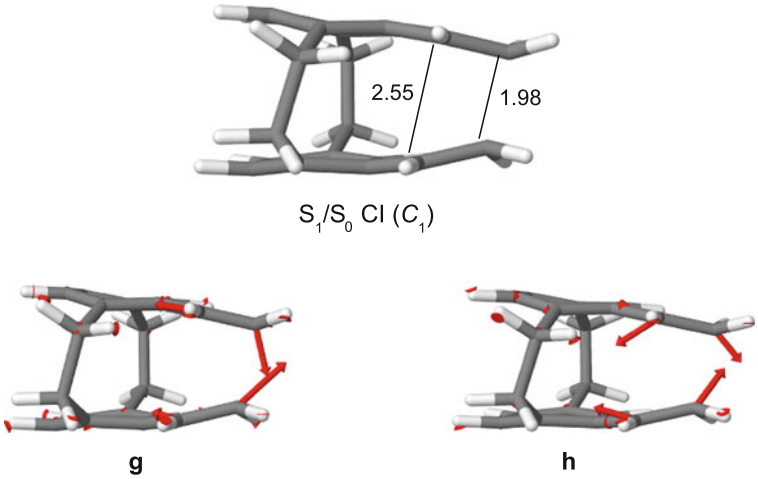

Fig. 7.4 The geometry, gradient difference (**g**) and derivative coupling (**h**) vectors at the S_1/S_0 MECI involved in [2+2]cycloaddition in GEM-V, calculated at the SA2-CAS(4,4)/6-31G(d) level of theory. Distances are measured in Å

created as a linear interpolation in internal coordinates between the Franck–Condon geometry and the geometry at the CI. It is apparent that the reactive diabatic state is S_a (the S_3 adiabatic state in the Franck–Condon region), agreeing with our expectations discussed above. The interpolated reaction path in the S_1 adiabatic state involves a small barrier of 0.2 eV of electronic energy. One should keep in mind, though, that the minimum-energy path could be different from the linearly interpolated one and thus not involve a barrier. Calculating a reliable minimum-energy path using SA-CASSCF would be prohibitively computationally expensive, though, since—as opposed to at the CI—a reasonable active space should include all the 16 π electrons. Furthermore, when taking the momentum of the wave packet into account it is not necessarily so that the minimum-energy path will be followed, since inertia also plays a role, as seen for example in the variation of S_1 lifetimes in α, β-enones [20]. Such dynamical effects can only be correctly addressed computationally by molecular dynamics simulations.

Pseudo-*para*-divinyl[2.2]paracyclophane (PARA-V)

Excited states were calculated for an optimized geometry of PARA-V and the three lowest excitation energies are shown in Table 7.1. Their predicted electronic characters are very similar to the corresponding states in GEM-V, agreeing with the similarity of the absorption spectra of the compounds Ref. II.

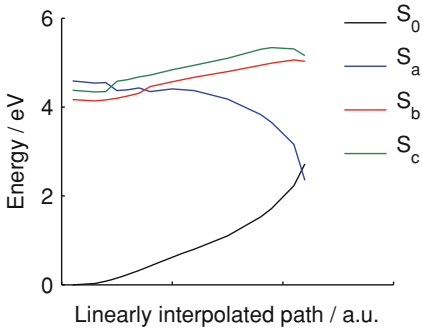

Fig. 7.5 RI-CC2/cc-pVDZ potential energy curves along the linearly interpolated reaction path from the Franck–Condon to the CI geometry in the anti-anti conformer of GEM-V. The excited-state curves are constructed so as to represent approximately diabatic states S_a, S_b and S_c

7.3.2 Time-Resolved Photoelectron Spectra

Ionization occurs to the ionic ground state for which the IPs were previously determined by He(I) photoelectron spectroscopy to 7.8 and 7.9 eV for GEM-V and PARA-V, respectively [21]. In the two experiments with pump wavelengths of $\lambda_p = 249$ nm and $\lambda_p = 300$ nm and a probe wavelength of $\lambda_e = 400$ nm, the total photon energies in a [1,2′] scheme are 11.2 and 10.3 eV, respectively. Time constants and DASs were determined by fitting the TRPES data as described previously (Sect. 3.3.3). In this chapter normalized DASs are defined as DASs that have been normalized to a maximum absolute amplitude of one.

Pseudo-*para*-divinyl[2.2]paracyclophane (PARA-V)

For PARA-V, only data with $\lambda_p = 249$ nm and $\lambda_e = 400$ nm were recorded. The resulting time-resolved photoelectron spectrum is shown in Fig. 7.6a. From the IP and the total photon energy, the maximum kinetic energy of the photoelectrons in a [1,2′] ionization scheme is 3.3 eV. The region of the spectrum corresponding to [1,1′] ionization, below 0.2 eV, is not considered and the data analysis focuses on the region between 0.5 and 3.3 eV. The photoelectron spectrum is broad and has no obvious structure. This is in agreement with the computational finding that a broad range of vinyl group twist angles gives rise to an extended range of conformations, Ref. II leading to an inhomogeneous broadening of the photoelectron spectrum.

The low kinetic energy region, below 2 eV, is delayed as compared to the high energy region above 2 eV (not visible to the eye in Fig. 7.6a). This is the signature of a lower lying state being populated by IC from the initial state excited at the Franck–Condon geometry. The IC converts electronic to vibrational energy, thereby shifting the signal to lower kinetic energies. Fitting the time-resolved photoelectron spectrum gave three time constants of 50 ± 30 fs, 0.6 ± 0.3 ps and >500 ps (the third time constant was too long to be reasonably estimated from the fit) and the DASs of these three channels are shown in Fig. 7.7a. As can be seen, the rise time of the

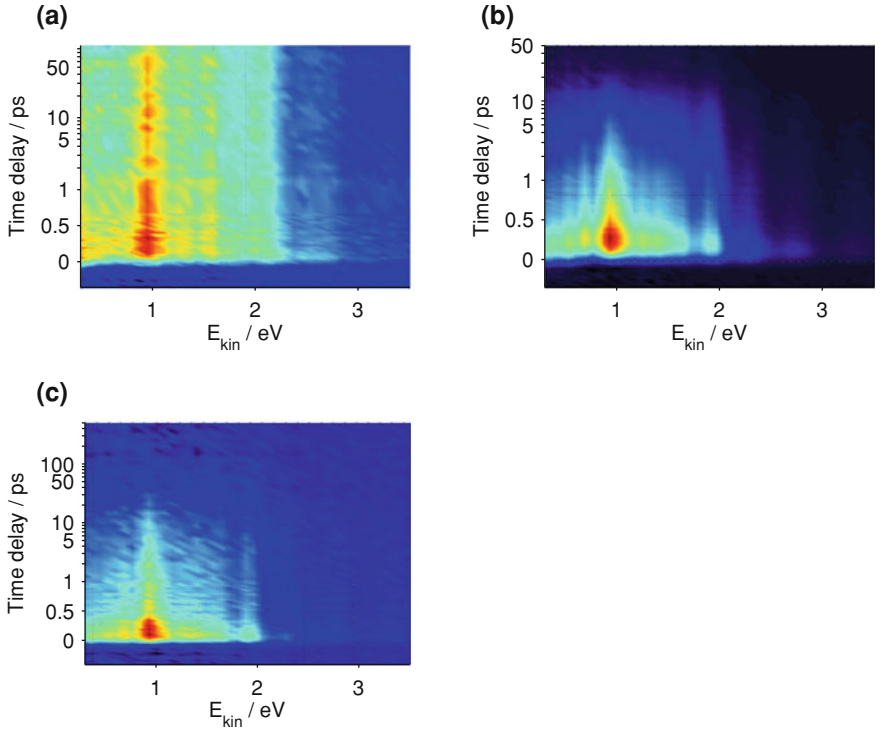

Fig. 7.6 Time-resolved photoelectron spectra of **a** PARA-V excited at $\lambda_p = 249\,\text{nm}$, **b** GEM-V excited at $\lambda_p = 249\,\text{nm}$ and **c** GEM-V excited at $\lambda_p = 300\,\text{nm}$. In all experiments pulses of center wavelength $\lambda_e = 400\,\text{nm}$ were used in the probing step

delayed part of the spectrum—corresponding to the region of the DAS that has a negative amplitude—is 50 fs. The intermediate state in the scheme has a lifetime of 0.5 ps, decaying to a much longer lived species with a lifetime of more than 500 ps.

Pseudo-*gem*-divinyl[2.2]paracyclophane (GEM-V)

As can be seen, the time-resolved photoelectron spectra of GEM-V shown in Fig. 7.6 are very similar to that of PARA-V. The $\lambda_p = 249\,\text{nm}$ data (Fig. 7.6b) was fitted to the same model as used in the previous section. The resulting three time constants are $120 \pm 30\,\text{fs}$, $330 \pm 50\,\text{fs}$ and $8.2 \pm 0.9\,\text{ps}$ and the DASs are shown in Fig. 7.7b. What is important to note is that the last time constant is 8.2 ps, much shorter than the $>500\,\text{ps}$ for the same step in PARA-V.

In the $\lambda_p = 300\,\text{nm}$ data (Fig. 7.6c) there are no time delayed features in the time-resolved photoelectron spectrum. Time constants and DASs were determined by fitting the [1,2′] region of the spectrum in the same manner as it was done for the

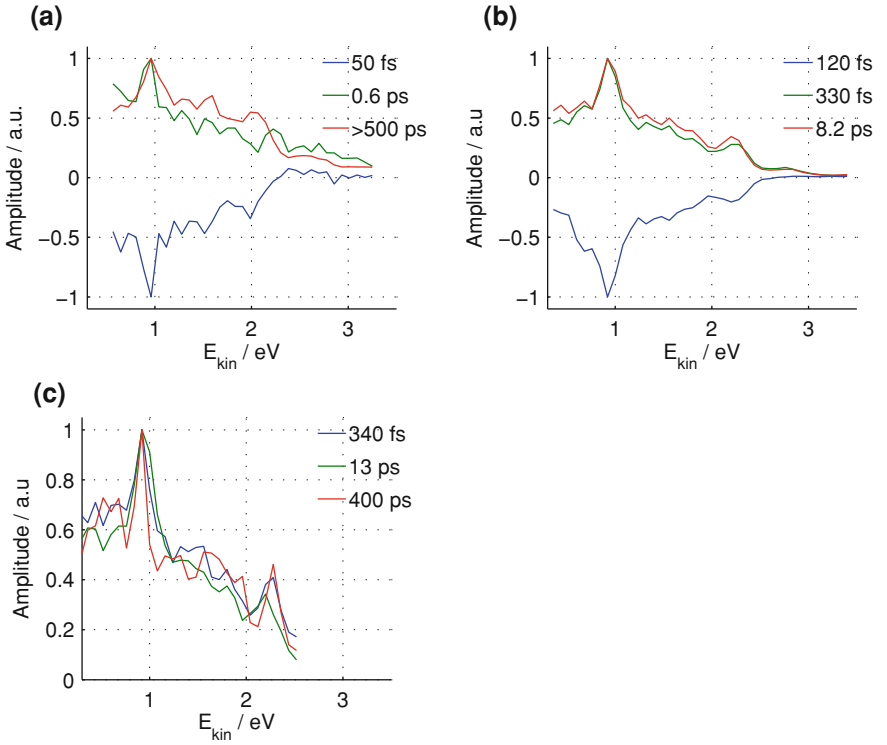

Fig. 7.7 Normalized DASs obtained from the global fits of the time-resolved photoelectron spectra shown in Fig. 7.6

$\lambda_p = 249\,\text{nm}$ data. The resulting three time constants are $340 \pm 50\,\text{fs}$, $13.5 \pm 1.0\,\text{ps}$ and $400 \pm 50\,\text{ps}$ and the DASs of these channels are shown in Fig. 7.7c.

7.4 Discussion

*7.4.1 Pseudo-*para*-divinyl[2.2]paracyclophane (PARA-V)*

The rise time, 50 fs, obtained from the fit of the time-resolved photoelectron spectrum is assigned to population of the S_2 and the S_1 state from the initially excited S_3 state. Since these states have overlapping photoelectron spectra, it is not possible to assign whether the dynamics are sequential—population of S_2 followed by a decay to S_1—or parallel—population of both S_2 and S_1 from S_3. This is because their DASs overlap heavily, eliminating the possibility for regions of negative amplitude that would reveal the order of state population (Sect. 3.3.3). We assign the 0.6 ps decay to the lifetime of the S_2 state, whereas the subsequent long-lived decay, >500 ps, is attributed to the lifetime of the S_1 state. This interpretation of the decay kinetics

is shown schematically in Fig. 7.8, assuming sequential population of the S_2 and the S_1 state. The S_1 lifetime in PARA-V is significantly longer than the styrene S_1 state lifetime of 88 ps, [22] but similar to the 100–300 ps lifetime of the S_1 state in the benzene dimer [23]. Assuming that the $S_1 \rightarrow S_0$ population decay pathway of PARA-V is similar to the one of styrene and other substituted benzenes, the reason for the long S_1 lifetime could be the rigidity of the paracyclophane cage structure, which restricts the out of plane motions of the benzene ring that lead to the S_1/S_0 CI [22–24].

*7.4.2 Pseudo-*gem*-divinyl[2.2]paracyclophane (GEM-V)*

Exciting the S_1 and S_2 States Directly

In the $\lambda_p = 300$ nm experiment both the S_1 and the S_2 states can be excited by the pump pulse. Thus, the time-resolved photoelectron spectrum is expected to reflect dynamics evolving in both states in parallel. From a kinetics perspective, this would give rise to a biexponential decay. This is indeed observed. The fact that the DASs are identical can be explained by ionization through an intermediate state, i.e. the absorption of the first of the two probe photons is resonant. Thus, the DASs are identical, because they represent the photoelectron spectrum of the intermediate highly excited state, not the excited states of interest. This is a clear illustration of how two-photon probing can wash out information, as discussed previously (Sect. 3.2.1). Whereas the DASs themselves therefore do not provide any information, the associated time constants do. We assign the 340 fs to the lifetime of the S_2 state. The two long time constants, 13.5 and 400 ps, are assigned to the lifetime of the S_1 state in the anti-anti and syn-anti conformer, respectively. This assignment is depicted schematically in Fig. 7.8 where, for simplicity, only sequential population of S_1 is shown. The interpretation is supported by the fact that the mean value of the ratios of the 13.5 and 400 ps decay amplitudes is 3.4, fairly close to the 3:1 anti-anti:syn-anti conformer ratio measured in the crystal Ref. II. One possible explanation of the relatively long lifetime of the S_1 state in the reactive anti-anti conformer is the presence of a barrier along the [2+2]reaction coordinate, as predicted by the calculations. The 400 ps lifetime of the syn-anti conformer agrees well with the >500 ps lifetime of the S_1 state in PARA-V. However, the fact that the S_1 lifetime is shorter in the syn-anti conformer of GEM-V excited at 300 nm as compared to PARA-V excited at 249 nm, gives some evidence that the ethylene group might cross the rotational barrier to form the anti-anti conformer, thus providing an additional decay channel that is not present in PARA-V.

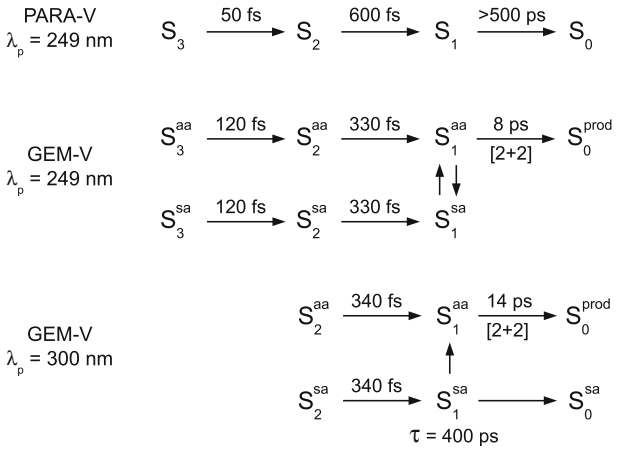

Fig. 7.8 The decay kinetics in PARA-V and GEM-V as interpreted from the TRPES data. The symbols S_x^{aa} and S_x^{sa} represent state x in the anti-anti and syn-anti conformer, respectively. S_0^{prod} refers to the ground state product of the [2+2]cycloaddition. The lifetime of the S_1^{sa} state, that decays by two different pathways, is indicated by τ

Exciting the S_3 State

The 120 fs rise time extracted by fitting the time-resolved photoelectron spectrum obtained when using $\lambda_p = 249$ nm is assigned to population of the S_2 and the S_1 states from the initially excited S_3 state. As was the case for PARA-V, these states have overlapping photoelectron spectra, so it is not possible to decide whether the dynamics are sequential or parallel. The decays are interpreted as described in the previous section; the short time constant is the lifetime of the S_2 state, whereas the longer one is that of the S_1 state (see Fig. 7.8). Note that the S_2 lifetime, 330 fs, is almost identical to that observed when exciting S_2 directly, despite the fact that the vibrational energy content is approximately 0.7 eV higher in the former experiment. This we assign to be a signature of non-adiabatic ultrafast dynamics, where population transfer is poorly described by density-of-states based models such as Fermi's Golden rule, because it is determined by the momentum in a small subset of the vibrational coordinates [20, 25–27].

It is noted that when populated from S_3, the decay of the S_1 state is not biexponential. We believe that this is because both conformers exhibit a S_1 lifetime of very similar magnitude. Considering that the vibrational excess energy in the S_1 state when populated from the S_3 state is approximately 1 eV, we find it likely that the rotational barrier of the vinyl group can now be crossed on a shorter timescale, bringing the molecule into the reactive anti-anti conformation in which [2+2]cycloaddition commences through the S_1/S_0 CI. In the framework of intramolecular vibrational-energy redistribution (IVR) this is indeed plausible. Thus, the vinyl group rotation is a low frequency mode that, because of a high density of states, is favored when IVR

commences in the S_1 state of the syn-anti conformer. Assuming that the S_1 lifetimes of both conformers are similar, it means that the rate of conversion of the syn-anti to the anti-anti conformer is faster than the rate of [2+2]cycloaddition. The lifetime, 8.2 ps, is shorter than that observed for direct excitation of S_1 in the $\lambda_p = 300$ nm experiment, 13.5 ps. This shortening of the lifetime can be explained by the higher vibrational energy content when S_1 is populated from the higher lying electronic state. The higher vibrational energy content might mean that the barrier towards the S_1/S_0 CI (in the present case leading to [2+2]cycloaddition) is crossed faster, as was previously observed for substituted benzenes [22].

7.5 Conclusion

This chapter presents a time-resolved investigation of a pseudo-bimolecular [2+2] cycloaddition performed using TRPES. The [2.2]paracyclophane scaffold of GEM-V was used to place two ethylene units at a distance at which the reaction can take place. Two conformers of the molecule, the anti-anti that is reactive in [2+2]cycloaddition and the syn-anti that is not, have been observed in X-ray diffraction measurements of the solid sample Ref. II. The presence of these two types of conformers makes the molecule an ideal system for an investigation of the relation between ground state conformation (determining the Franck–Condon geometry) and excited-state reactivity in a [2+2]photocycloaddition. Experiments were also performed on the isomeric reference compound PARA-V in which the ethylene units cannot react via [2+2]cycloaddition. The S_1 state in PARA-V has a lifetime of more than 500 ps. When exciting the S_1 state in GEM-V directly, the two conformers seem to exhibit quite different lifetimes; 13.5 ps in the anti-anti and 400 ps in the syn-anti conformer. This result shows the importance of the molecular conformation prior to light absorption in inducing a [2+2]cycloaddition: the S_1 lifetime in the non-reactive syn-anti conformation is significantly longer than in the reactive anti-anti conformation. Furthermore, the experiments show that it is only the lifetime of the S_1 state, in which the calculations predict the [2+2]cycloaddition to occur through a S_1/S_0 CI, that is significantly affected by the vicinity of the ethylene units. Accordingly, the observed S_3 and S_2 state lifetimes of GEM-V and PARA-V do not differ much.

With respect to the [2+2]cycloaddition leading to thymine dimerization in DNA a conformation which is non-reactive in [2+2]cycloaddition is of crucial importance. This is because it allows for ultrafast electronic relaxation mechanisms [28–35] to efficiently compete with the harmful thymine dimerization channel, thereby protecting the DNA strand. Thus, extrapolating from the findings of this experiment, it seems that ground state conformation before light absorption is just as important as the relaxation mechanisms in protecting DNA from photodamage, consistent with the suggestions of Schreier et al. [11].

References

1. Scherer, N.F., Sipes, C., Bernstein, R.B., Zewail, A.H.: J. Chem. Phys. **92**, 5239–5259 (1990)
2. Scherer, N.F., Khundkar, L.R., Bernstein, R.B., Zewail, A.H.: J. Chem. Phys. **87**, 1451–1453 (1987)
3. van Zee, R.D., Stephenson, J.C.: J. Chem. Phys. **102**, 6946–6948 (1995)
4. Miller, C.C., van Zee, R.D., Stephenson, J.C.: J. Chem. Phys. **114**, 1214–1232 (2001)
5. Wester, R., Bragg, A.E., Davis, A.V., Neumark, D.M.: J. Chem. Phys. **119**, 10032–10039 (2003)
6. Bondarenko, L., Hentschel, S., Greiving, H., Grunenberg, J., Hopf, H., Dix, I., Jones, P.G., Ernst, L.: Chem. Eur. J. **13**, 3950–3963 (2007)
7. Cadet, J., Vigny, P.: Chapter the photochemistry of nucleic acids. In: Morrison, H. (ed.) Bioorganic Photochemistry, vol. 1, pp. 1–272. John Wiley and Sons Inc., New York (1990)
8. Douki, T., Reynaud-Angelin, A., Cadet, J., Sage, E.: Biochemistry **42**, 9221–9226 (2003)
9. Taylor, J.S.: Acc. Chem. Res. **27**, 76–82 (1994)
10. Vink, A.A., Roza, L.: J. Photochem. Photobiol. B **65**, 101–104 (2001)
11. Schreier, W.J., Schrader, T.E., Koller, F.O., Gilch, P., Crespo-Hernández, C.E., Swaminathan, V.N., Carell, T., Zinth, W., Kohler, B.: Science **315**, 625–629 (2007)
12. Caramori, G.F., Galembeck, S.E., Laali, K.K.: J. Org. Chem. **70**, 3242–3250 (2005)
13. Henseler, D., Hohlneicher, G.: J. Phys. Chem. A **102**, 10828–10833 (1998)
14. Hope, H., Bernstein, J., Trueblood, K.N.: Acta Crystallogr. Sect. B: Struct. Crystallogr. Cryst. Chem. **28**, 1733–1743 (1972)
15. Kobayashi, T., Yokota, K., Nagakura, S.: J. Electron Spectrosc. Relat. Phenom. **2**, 449–454 (1973)
16. Heilbronner, E., Yang, Z.-Z.: The electronic structure of cyclophanes as suggested by their photoelectron spectra. In: Vögtle, F. (ed.) Topics in Current Chemistry, vol. 115, pp. 1–55 (1983)
17. Ribblett, J.W., Borst, D.R., Pratt, D.W.: J. Chem. Phys. **111**, 8454–8461 (1999)
18. Bernardi, F., De, S., Olivucci, M., Robb, M.A.: J. Am. Chem. Soc. **112**, 1737–1744 (1990)
19. Dallos, M., Lischka, H., Shepard, R., Yarkony, D.R., Szalay, P.G.: J. Chem. Phys. **120**, 7330–7339 (2004)
20. Lee, A.M.D., Coe, J.D., Ullrich, S., Ho, M.-L., Lee, S.-J., Cheng, B.-M., Zgierski, M.Z., Chen, I.-C., Martinez, T.J., Stolow, A.: J. Phys. Chem. A **111**, 11948–11960 (2007)
21. Yang, Z., Heilbronner, E., Hopf, H., Ehrhardt, S., Hentschel, S.: J. Phys. Chem. **92**, 914–917 (1988)
22. Lee, S.-H., Tang, K.-C., Chen, I.-C., Schmitt, M., Shaffer, J.P., Schultz, T., Underwood, J.G., Zgierski, M.Z., Stolow, A.: J. Phys. Chem. A **106**, 8979–8991 (2002)
23. Radloff, W., Freudenberg, T., Ritze, H.H., Stert, V., Noack, F., Hertel, I.V.: Chem. Phys. Lett. **261**, 301–306 (1996)
24. Lasorne, B., Sicilia, F., Bearpark, M.J., Robb, M.A., Worth, G.A., Blancafort, L.: J. Chem. Phys. **128**, 124307 (2008)
25. Diau, E.W.-G., Kötting, C., Sølling, T.I., Zewail, A.H.: Chem. Phys. Chem **3**, 57–78 (2002)
26. Sølling, T.I., Diau, E.W.-G., Kötting, C., Feyter, S.D., Zewail, A.H.: Chem. Phys. Chem **3**, 79–97 (2002)
27. Schalk, O., Boguslavskiy, A.E., Stolow, A.: J. Phys. Chem. A **114**, 4058–4064 (2010)
28. Crespo-Hernández, C.E., Cohen, B., Hare, P.M., Kohler, B.: Chem. Rev. **104**, 1977–2020 (2004)
29. Ullrich, S., Schultz, T., Zgierski, M.Z., Stolow, A.: Phys. Chem. Chem. Phys. **6**, 2796–2801 (2004)
30. Ullrich, S., Schultz, T., Zgierski, M.Z., Stolow, A.: J. Am. Chem. Soc. **126**, 2262–2263 (2004)
31. Nielsen, S.B., Sølling, T.I.: Chem. Phys. Chem **6**, 1276–1281 (2005)
32. Satzger, H., Townsend, D., Zgierski, M., Patchkovskii, S., Ullrich, S., Stolow, A.: Proc. Natl. Acad. Sci. U.S.A. **103**, 10196–10201 (2006)
33. Hudock, H.R., Levine, B.G., Thompson, A.L., Satzger, H., Townsend, D., Gador, N., Ullrich, S., Stolow, A., Martínez, T.J.: J. Phys. Chem. A **111**, 8500–8508 (2007)
34. Middleton, C.T., de La Harpe, K., Su, C., Law, Y.K., Crespo-Hernández, C.E., Kohler, B.: Annu. Rev. Phys. Chem. **60**, 217–239 (2009)
35. Bisgaard, C.Z., Satzger, H., Ullrich, S., Stolow, A.: Chem. Phys. Chem **10**, 101–110 (2009)

Chapter 8
Paracyclophanes II: The Paternò-Büchi Reaction

This chapter presents the second study of a bimolecular photochemical reaction realized using the [2.2]paracyclophane scaffold. The reaction, a cycloaddition between a photoexcited carbonyl group and an alkene to form a four-membered cyclic ether (oxetane), is named the Paternò-Büchi (PB) reaction [1, 2]. The experiments realizing the first fs time-resolved investigation of the PB reaction, were performed using the Ottawa magnetic bottle spectrometer (Sect. 6.2.2, page 70). Readers interested in specific experimental and computational details are referred to Ref. III.

8.1 Motivation

The PB reaction has been extensively used in preparative chemistry [3, 6] and widely studied in a mechanistic perspective [2, 7–14]. It is induced by exciting the (n, π^*) state of the carbonyl group containing molecule, and has a high regio- and stereoselectivity. Zimmerman suggested that the selectivity is governed by a non-concerted mechanism in which a 1,4-biradical intermediate is formed upon attack of the C=O group on the alkene moiety [8]. As shown in Fig. 8.1 there are two types of 1,4-biradicals, resulting from either C–C (**1**) or O–C attack (**2**). The regioselectivity of the reaction was inferred from the stability of the intermediate 1,4-biradicals, i.e. that the major product is formed from the most stable biradical [8]. This step-wise mechanism was supported by results from experiments on the PB reaction between benzophenone and dioxene in which a triplet C–C 1,4-biradical intermediate was observed and its lifetime determined to be on the order of ns [9, 10]. The reason for the long lifetime of the triplet biradical is that ring closure to form the oxetane has to be preceded by the forbidden process of a spin flip, as opposed to a reaction in the singlet state. A more detailed understanding of the excited-state part of the reaction was achieved in the computational work on the prototype system of formaldehyde and ethylene by Palmer et al. [11]. They revealed the presence of two CIs between the singlet (n, π^*) and the ground state, corresponding to O–C and

R. Y. Brogaard, *Molecular Conformation and Organic Photochemistry*,
Springer Theses, DOI: 10.1007/978-3-642-29381-8_8,
© Springer-Verlag Berlin Heidelberg 2012

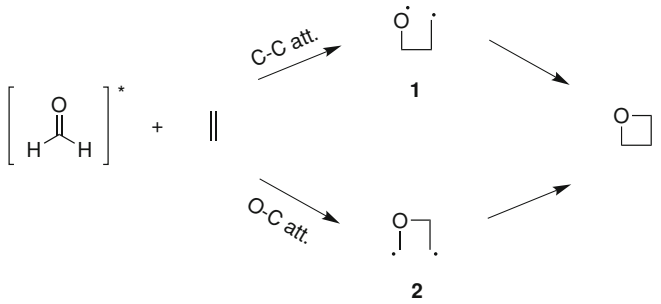

Fig. 8.1 Scheme illustrating the Paternò-Büchi reaction between excited formaldehyde and ground state ethylene to form oxetane. The reaction can proceed through either of two biradical intermediates, one resulting from C–C (**1**) and one from O–C attack (**2**)

C–C bond formation, respectively. The CI corresponding to C–C bond formation is situated very close to the products on the PES, meaning that ring closure to form the four-membered oxetane ring on the ground state can occur without involving any intermediates. On the contrary, the CI corresponding to O–C bond formation is situated close to the reactants on the PES, and passage through this CI leads to an intermediate C–C 1,4-biradical, where ring closure to form the oxetane ring in the ground state is associated with a barrier. Studies of the photodissociation of oxetane have provided some insight on the retro PB reaction; both product kinetic energy distributions [15] and TRMS results [16] point to an ultrafast dissociation with the singlet reaction being the dominant reaction pathway [15].

In general aliphatic ketones react via the singlet (n, π^*) state [3, 17], whereas the high ISC rates of aromatic carbonyl compounds [18] means that PB reactions involving these species occur almost exclusively through their triplet states [3, 7, 17]. What distinguishes the singlet and triplet pathway is the excited-state part of the PB reaction, i.e. whether there is a 'detour' via ISC from the singlet (n, π^*) state to the triplet state manifold, or the entire reaction occurs in the singlet state manifold. Palmer et al. calculated the geometries and energies of the triplet biradicals in the formaldehyde/ethylene model system to be quite similar to their singlet counterparts [11]. They concluded that whether the ground state is populated from the triplet excited state via ISC or from the singlet excited state via IC, does not significantly affect the final part of the reaction taking place in the ground state. Recent experimental work suggests that this is not the case if the reactants are substituted, though, since the conformations mediating efficient ISC in the long-lived triplet biradicals result in a different regio- and stereoselectivity than obtained in the singlet state pathway, in which the lifetime of the biradicals is much shorter [14].

In this work we perform a fs time-resolved study of a PB reaction with the aim of providing new insights on the excited-state dynamics of the reaction, in particular regarding the interplay between the singlet and triplet state manifold. We proceed along the same route as in Chap. 7 and use pseudo-*gem*-vinylformyl[2.2]-paracyclophane (GEM-VF, Fig. 8.2) as a model system. The pseudo-*para* isomer of

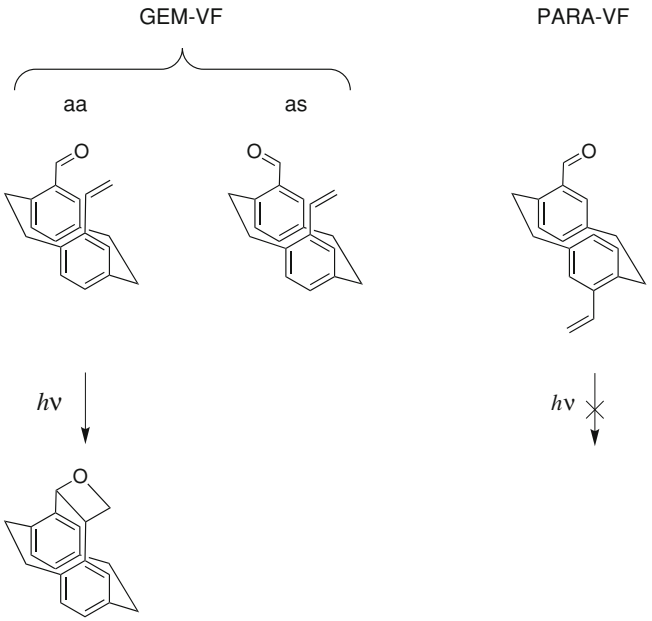

Fig. 8.2 The anti-anti (*aa*) and anti-syn (*as*) conformers of pseudo-*gem*-vinylformyl-[2.2]paracyclophane (GEM-VF). Only the anti-anti conformer reacts in a PB reaction. Also shown is the non-reactive reference compound pseudo-*para*-vinylformyl[2.2]paracyclophane (PARA-VF)

GEM-VF (PARA-VF, Fig. 8.2), in which the functional groups cannot react, is used as a reference compound. Being an aromatic carbonyl compound, ISC should be very efficient in GEM-VF, making it suitable for studying the interplay between singlet and triplet states in the PB reaction.

8.2 Results

The following sections will present and discuss computational results as well as data obtained in TRPES experiments on GEM-VF and PARA-VF.

8.2.1 Computational Results

Pseudo-*gem*-vinylformyl[2.2]paracyclophane (GEM-VF)

X-ray crystallography data show that both the anti-anti and anti-syn conformers of GEM-VF are present in the crystal and interconvert at the low temperature of the

Table 8.1 RI-CC2/cc-pVDZ excitation energies of singlet states of GEM-VF (anti-anti (aa) and anti-syn (as) conformer) and PARA-VF compared to experimental values obtained from the gas phase absorption spectra

	GEM-VF			PARA-VF	
	Calc. aa	Calc. as	Exp.	Calc.	Exp.
S_1 (n, π^*)	3.80	3.79	3.8	3.80	3.8
S_2 (π, π^*)	4.09	4.10	4.1	4.07	4.0
S_3 (π, π^*)	4.30	4.25	4.8	4.33	4.8

Values are in eV

diffraction experiment Ref. III. Therefore both conformers are present in the molecular beam after sublimation of the solid sample. Thus, we have optimized the geometries of both conformers (B3LYP/6-31G(d)) and calculated vertical excitations to singlet states to get an insight on their electronic structure in the Franck-Condon region. The calculated excitation energies are listed in Table 8.1 together with the experimental values obtained from gas phase absorption spectra Ref. III. The orbitals involved in the description of the lowest lying electronic states of the anti-anti conformer are shown in Fig. 8.3 (those of the anti-syn conformer are practically identical). The most important configuration in the description of the S_1 state is an $(n(\mathrm{O}), \pi^*)$ excitation. The S_2 state is mainly a (π_a, π^*) excitation, whereas the most important configuration in the S_3 state is (π_b, π^*). The S_1 state is therefore expected to be the reactive state in a PB reaction, analogously to the (n, π^*) state in the formaldehyde/ethylene model system. The S_3 state is interesting because of its pronounced similarity to the reactive (π, π^*) state in the [2+2]cycloaddition in GEM-V (Fig. 7.3, page 79). Thus, the $S_3(\pi, \pi^*)$ state of GEM-VF might lead to PB reaction, analogously to the formation of photocycloaddition products observed from thioketones excited to the $S_2(\pi, \pi^*)$ state in the presence of olefins [19].

Since the focus of this work is on the interplay between the excited-state singlet and triplet manifold in the PB reaction, the triplet states of interest are the ones located below the reactive S_1 state and therefore available for ISC. Table 8.2 shows the calculated excitation energies of the first four triplet states, three of which are energetically below S_1. Note that in the Franck–Condon structure the order of the (n, π) and (π, π^*) states is reversed in the triplet as compared to the singlet state manifold. $T_1(\pi, \pi^*)$ is non-reactive in PB reaction, but it has been seen before ([18], p. 630) that reactivity of carbonyl containing compounds can take place from a higher lying (n, π^*) state (in this case T_2) if it is energetically close.

To investigate how well GEM-VF models the ideal bimolecular PB reaction, we conducted a search for S_1/S_0 MECIs at the SA2-CAS(6, 5)/6-31G(d) level of theory, to locate structures similar to those found by Palmer et al. [11]. As it is generally accepted that O–C attack is favored for electron rich alkenes [3] such as GEM-VF, we focus on the MECI corresponding to O–C attack. The structure, the gradient difference (**g**) and derivative coupling (**h**) vectors at the CI shown in Fig. 8.4 are very similar to what Palmer et al. obtained [11]. This indicates that the paracyclophane scaffold does not impose a severe geometrical restriction along the excited-state part

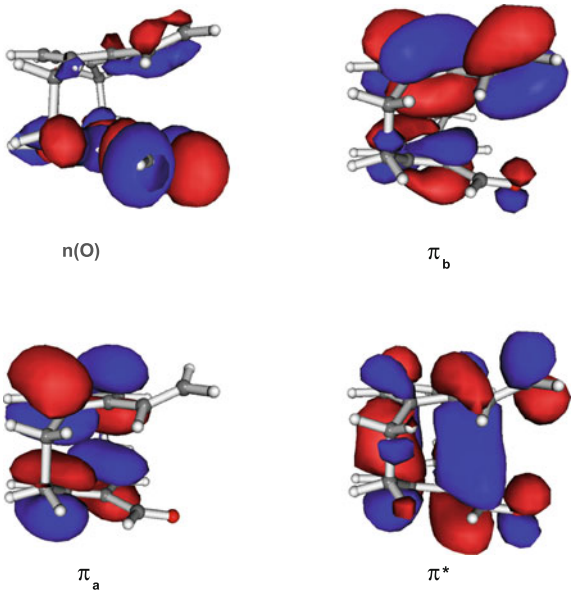

Fig. 8.3 RI-CC2/cc-pVDZ orbitals involved in the most important configurations describing the excited states of GEM-VF

Table 8.2 RI-CC2/cc-pVDZ excitation energies of the first four triplet states of GEM-VF (anti-anti (aa) and anti-syn (as) conformer) and PARA-VF

	GEM-VF		PARA-VF
	aa	as	
T_1 (π, π^*)	3.23	3.27	3.20
T_2 (n, π^*)	3.42	3.43	3.42
T_3 (π, π^*)	3.56	3.54	3.56
T_4 (π, π^*)	3.91	3.95	3.90

Values are in eV

of the PB reaction path commencing through O–C attack, when compared to the true bimolecular PB reaction between ethylene and formaldehyde. An RI-CC2/cc-pVDZ calculation shows that the CI is situated 3.4 eV above the ground state minimum which is 0.4 eV below the S_1 energy in the Franck-Condon region, indicating that the CI is energetically accessible.

It is desirable to calculate a minimum-energy path in the S_1 state from the Franck-Condon region to the CI, since that would give an idea about the path the wave packet follows in the excited-state part of the PB reaction. At the CASSCF level this would require a balanced description of the electronic structure of the S_1 state along the entire path, a requirement that the (6,5) active space does not fulfill and that would only be satisfied by including all the π electrons in the paracyclophane scaffold in the active space—a prohibitively expensive computational task. Instead, potential

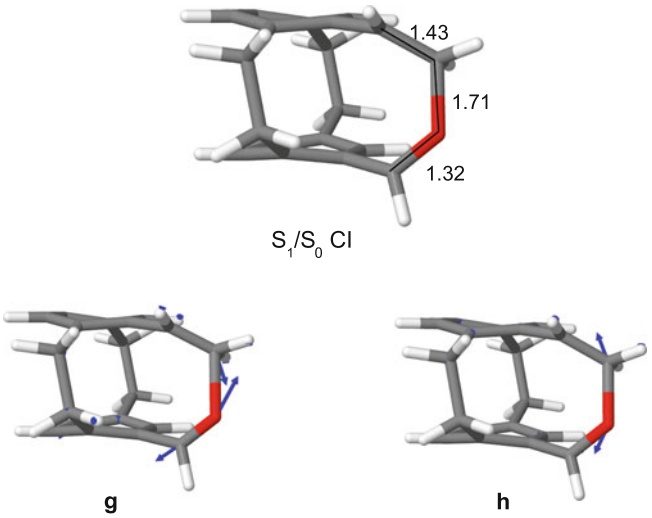

Fig. 8.4 The structure, the gradient difference (**g**) and derivative coupling (**h**) vectors at the S_1/S_0 MECI corresponding to O–C attack in the PB reaction in GEM-VF, calculated at the SA2-CAS(6, 5)/6-31G(d) level of theory. Distances are measured in Å

energy curves of the first three singlet and triplet excited states were calculated at the RI-CC2/cc-pVDZ level along an approximated path of the excited-state part of the PB reaction corresponding to O–C attack. The path was constructed by linear interpolation in internal coordinates from the Franck–Condon to the CI structure and the resulting potential energy curves are shown in Fig. 8.5.

We note the presence of a small barrier along the curve of the reactive S_1 state. This is not a definite proof of an excited-state barrier in the PB reaction in GEM-VF, though, since a barrier-free path could exist. Interestingly, T_1 is indeed reactive in the PB reaction, although it has (π, π^*) character in the Franck–Condon region. This is due to strong mixing between the (n, π^*) and (π, π^*) states along the pathway, which is present in both the singlet and triplet state manifold. The mixing is important to the interpretation of the time-resolved photoelectron spectra, since it means that the states are likely to show corresponding ionization correlations, in this case meaning that they all ionize to the electronic ground state of the cation.

Finally it is important to note that quite near the Franck-Condon region there is a crossing between the $S_1(n, \pi^*)$ and the $T_3(\pi, \pi^*)$ state. According to El-Sayed's rules (Sect. 2.1.3, page 11) the rate of ISC between S_1 and T_3 will be high, since in this case the change of spin state is accompanied by a change in orbital angular momentum. Furthermore, according to the energy gab law ([17], Chap. 4 pp. 130–131) ISC is most efficient for isoenergetic states and the S_1/T_3 crossing is therefore important, since it means that it is likely that ISC will compete efficiently with the singlet state reaction pathway of the PB reaction.

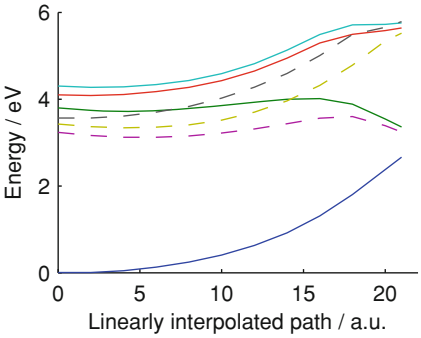

Fig. 8.5 RI-CC2/cc-pVDZ potential energy curves of the ground state and first three singlet (*solid*) and triplet (*dashed*) excited states along an approximated excited-state path of the PB reaction corresponding to O–C attack in GEM-VF. The curves were constructed from vertical excitation energies calculated at structures along a path defined as a linear interpolation in internal coordinates from the Franck–Condon to the S_1/S_0 CI structure

Pseudo-*para*-vinylformyl[2.2]paracyclophane (PARA-VF)

Since PARA-VF works as a reference compound, it is important to confirm that the electronic structures of the excited states are quite similar to those of GEM-VF. We therefore optimized the ground state geometry of PARA-VF and calculated singlet excited states from this structure. The vertical excitation energies are shown in Table 8.1. The values are within the accuracy of the method identical to those of GEM-VF, agreeing with the similarity of the corresponding absorption spectra. Also the orbitals (not shown) involved in the most important configurations of the excited states are almost identical to those of GEM-VF. The similarity between PARA-VF and GEM-VF also applies to the calculated triplet states and vertical excitation energies at the Franck-Condon structure shown in Table 8.2. This means that PARA-VF can work as a reference compound for the ISC rate in a case where the PB reaction channel is not present.

8.2.2 Time-Resolved Photoelectron Spectra

TRPES data was recorded using two different pump wavelengths $\lambda_p = 320\,\text{nm}$ and $\lambda_p = 256\,\text{nm}$. In both cases the probe wavelength was $\lambda_e = 400\,\text{nm}$. Although the exact IPs for GEM-VF and PARA-VF are not known experimentally, they can be estimated from photoelectron spectroscopy data on a series of vinyl-substituted [2.2]paracyclophanes recorded by Yang et al. [20]. As mentioned in the previous section, all excited states are likely to ionize to the D_0 state of the cation. As can be seen from Fig. 8.3 the HOMO π_b has almost no density at the formyl group. Thus, we approximate the IP of GEM-VF to be similar to the IP of the molecule

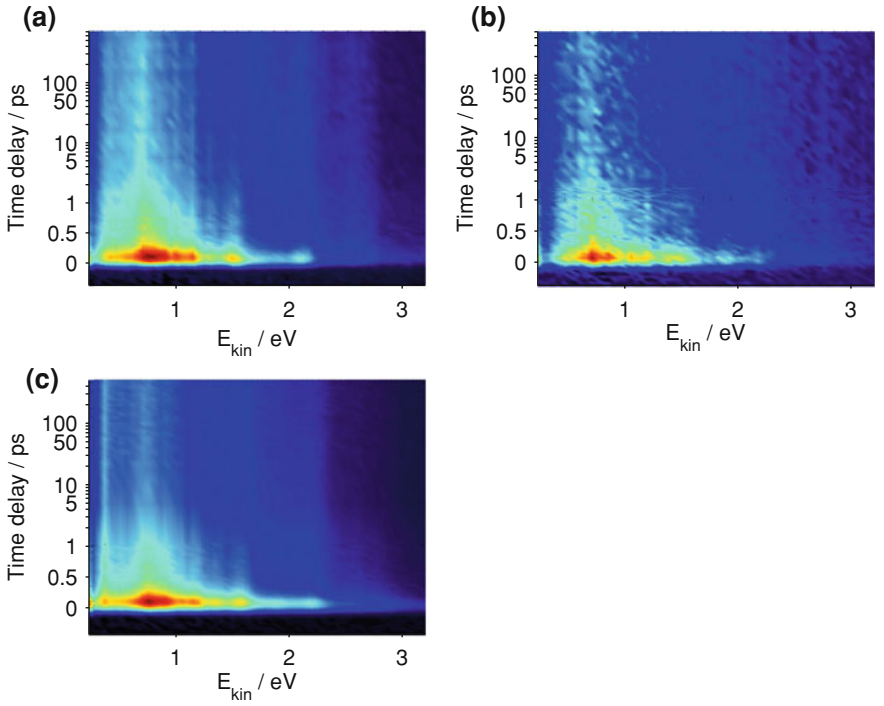

Fig. 8.6 Time-resolved photoelectron spectra of GEM-VF and PARA-VF. In all experiments a probing wavelength of $\lambda_e = 400$ nm was used. **a** PARA-VF excited at $\lambda_p = 315$ nm. **b** GEM-VF excited at $\lambda_p = 320$ nm. **c** GEM-VF excited at $\lambda_p = 256$ nm

without the formyl group, determined to be 8.0 eV [20]. Since the HOMO of PARA-VF (not shown) exhibits the same properties as the HOMO of GEM-VF, the IP of PARA-VF is approximated to the same value. For comparison, the IPs of pseudo-*gem* and pseudo-*para*-divinyl[2.2]paracyclophane are 7.8 and 7.9 eV, respectively [20], supporting this approximation.

Time constants and DASs were determined by fitting the TRPES data as described previously (Sect. 3.3.3, page 30).

Pseudo-*para*-vinylformyl[2.2]paracyclophane (PARA-VF)

For PARA-VF, only data with $\lambda_p = 315$ nm was recorded. The resulting time-resolved photoelectron spectrum is shown in Fig. 8.6a. From the IP and the total photon energy, the maximum kinetic energy of the photoelectrons in a [1,2′] ionization process is 2.2 eV. The data analysis will focus on the [1,2′] region of the spectrum. The PE spectrum is broad and has no obvious structure, as it was the case in GEM-V, where it was explained by inhomogeneous broadening caused by

an ensemble of conformations with different twist angles of the vinyl groups with respect to the benzene rings (Chap. 7). Accordingly this should apply to the formyl group as well. Furthermore, in a series of resonance enhanced multiphoton ionization (REMPI) experiments on substituted [2.2]paracyclophanes Schon et al. observed extended progressions of large-amplitude vibrations involving the paracyclophane scaffold [21, 22]. Those progressions are likely to be present in our photoelectron spectra as well, however insufficient resolution makes them appear as a broadening of the spectra. The time evolution of the spectrum was fitted to a biexponential decay with time constants of 130 fs and 1.7 ps as well as a constant offset component. The DASs are shown in Fig. 8.7a.

Pseudo-*gem*-vinylformyl[2.2]paracyclophane (GEM-VF)

For GEM-VF data with pump wavelengths of $\lambda_p = 320$ nm and $\lambda_p = 256$ nm, respectively, was recorded. In both experiments a probe wavelength of $\lambda_e = 400$ nm was used. The time-resolved photoelectron spectra are shown in Fig. 8.6b and 8.6c, respectively. In a [1,2′] ionization scheme, the maximum kinetic energy of the photoelectrons is 2.1 and 3.1 eV in the $\lambda_p = 320$ nm and $\lambda_p = 256$ nm experiment, respectively. The data analysis will focus on the [1,2′] region. The spectrum obtained in the $\lambda_p = 320$ nm experiment is very similar to that of PARA-VF discussed above.

The data recorded at $\lambda_p = 320$ nm was fitted to a biexponential decay with time constants of 110 fs and 1.8 ps as well as a constant offset component. The corresponding DASs are shown in Fig. 8.7b. The similarity of the fits of the PARA-VF and GEM-VF data at this pump wavelength is striking.

For the data recorded with $\lambda_p = 256$ nm we observe the low kinetic energy part of the spectrum to be delayed in time as compared to the high kinetic energy part. This is the signature of a lower lying state being populated by IC from the initial state excited at the Franck–Condon geometry. The IC process converts electronic to vibrational energy, thereby shifting the signal to lower kinetic energies. Thus, the best fit was obtained by using three exponential decay components, as well as an offset component. The DASs are shown in Fig. 8.7c. The temporal shift in the TRPES data is modeled by the fit in the DAS corresponding to the 50 fs time-constant; the negative amplitude in the low-energy region shows that this part of the spectrum rises on the same ultrashort time-scale as the high energy part decays. The following biexponential decay to the offset is described by time constants of 110 fs and 1.8 ps. These values are nearly identical to those obtained from the fit of the GEM-VF experiment using $\lambda_p = 320$ nm, as well as the experiment on PARA-VF.

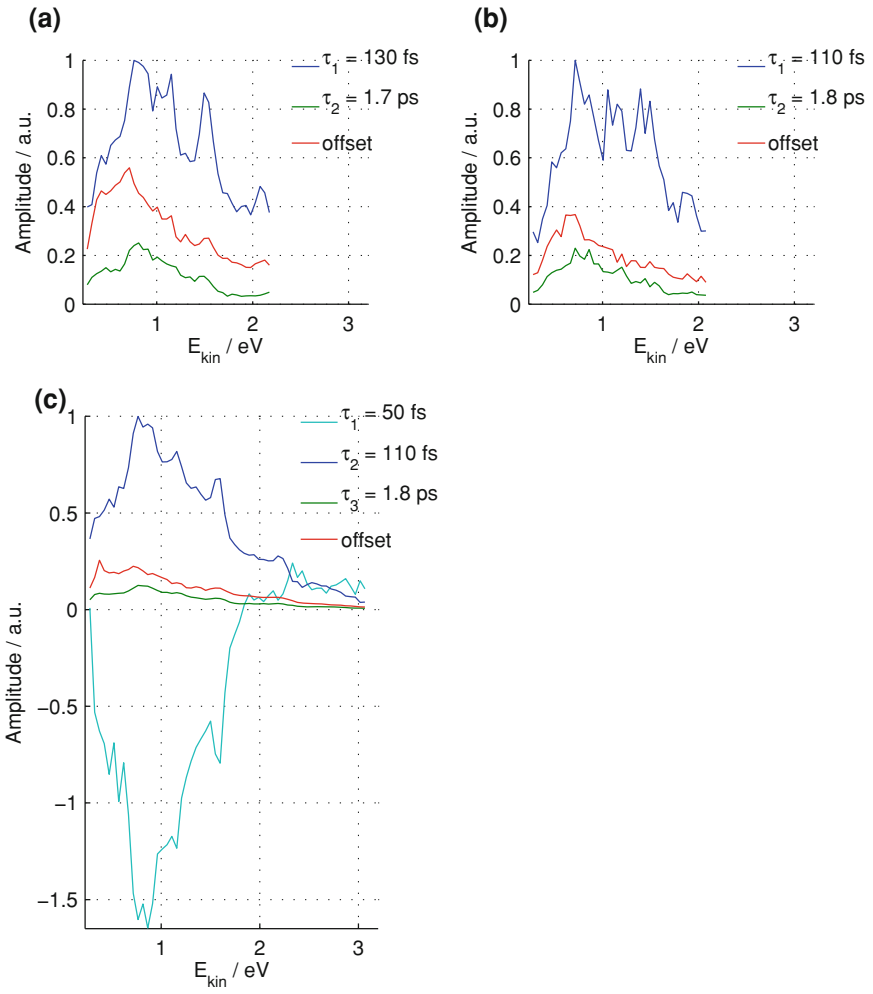

Fig. 8.7 DASs obtained from the global fits of the corresponding time-resolved photoelectron spectra in Fig. 8.6

8.3 Discussion

*8.3.1 Pseudo-*para*-vinylformyl[2.2]paracyclophane (PARA-VF)*

Upon excitation with $\lambda_p = 315\,\text{nm}$ the S_2 state is reached. Thus, the two time constants of 130 fs and 1.7 ps represent the decay of the S_2 and the S_1 state, respectively. The offset component is then assigned to the triplet state manifold. The most interesting finding from the reference experiment is that ISC from S_1 proceeds in less

than two ps. The high ISC rate indicates that the population of the $S_1(n, \pi^*)$ state is transferred to a triplet (π, π^*) state (likely T_3), according to El-Sayed's rules mentioned above. Since the time scale of ISC is an order of magnitude shorter than the reaction time for [2+2]cycloaddition in GEM-V (Chap. 7), we claim that ISC can compete with any reactive dynamics in the S_1 state of GEM-VF.

*8.3.2 Pseudo-*gem-*vinylformyl[2.2]paracyclophane (GEM-VF)*

As in PARA-VF, excitation of GEM-VF at $\lambda_p = 320\,\text{nm}$ populates the S_2 state. This allows for a similar assignment of the fitted decay times: the lifetime of the S_2 state in GEM-VF is 110 fs, whereas the S_1 state is depopulated in 1.8 ps. Importantly, the offset component assigned to the triplet state is also present in the data for GEM-VF. The finding that the S_1 lifetime is not reduced as compared to PARA-VF, leads to the conclusion that ISC competes very efficiently with the singlet PB reaction, making the latter a minor decay pathway in GEM-VF. From solution phase experiments we determined a lower bound for the quantum yield of the PB reaction in GEM-VF to $7 \pm 2\%$ (unpublished data). Since we do not observe any noticeable difference in the measured lifetimes of the singlet states in GEM-VF and PARA-VF, we conclude that the reaction predominantly takes place in the triplet state manifold. Most likely ISC occurs to $T_3(\pi, \pi^*)$ which can decay by IC to the reactive T_1 state. The presence of this reactive pathway in GEM-VF seems to disagree with the fact that the lifetime of the triplet state is more than one ns (the value cannot be reasonably extracted from the fit, since data was not recorded for time delays longer than 700 ps) in both PARA-VF and GEM-VF. However, it should be remembered that the PB reaction in the triplet state will lead to a triplet biradical that has to undergo ISC to decay to S_0, which is an inherently slow process that takes place on the order of ns. This scenario is sketched in Fig. 8.8. Thus, the reaction channel available in GEM-VF does not shorten the lifetime of the triplet state as compared to PARA-VF, such that a difference between the molecules could be observed in our experiment.

In the experiment with $\lambda_p = 256\,\text{nm}$ the pump pulse excites the $S_3(\pi, \pi^*)$ state, which, as mentioned in the discussion of the computational results, could lead to a cycloaddition reaction that resembles the concerted [2+2]cycloaddition leading to the dimerization of ethylene. Such a concerted reaction is interesting because the mechanism is conceptually different to the step-wise PB reaction involving a biradical ground state intermediate. The lifetime of the S_3 state is reflected in the first time constant of the fit, $\tau_1 = 50\,\text{fs}$. From the fit it is not possible to conclude whether S_3 decays to S_2 and S_1 in a sequential or a parallel process, since their DASs overlap, suppressing the regions of negative amplitude that would normally reveal the population order (Sect. 3.3.3, page 30). The last two time constants of 110 fs and 1.8 ps are assigned to the lifetimes of the S_2 and the S_1 state, respectively. These values are listed in Table 8.3 together with the values obtained from the experiments presented above. As in the interpretation of those experiments, the constant offset component is assigned to a triplet state. Thus, there is no indication of a concerted

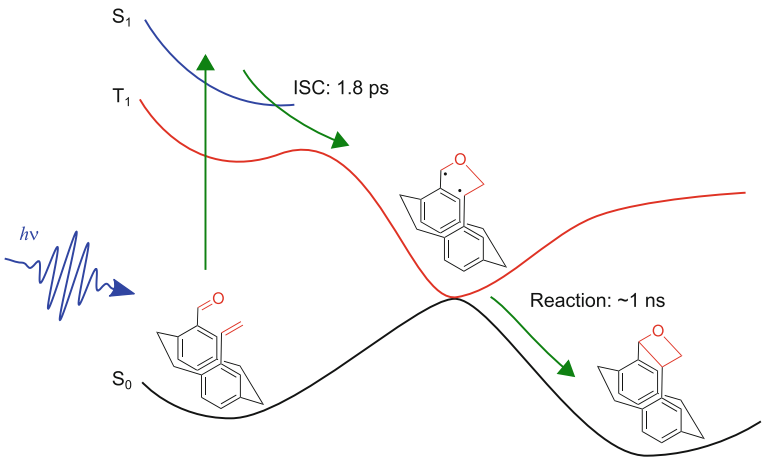

Fig. 8.8 Schematic illustration of the PB reaction dynamics in GEM-VF. Note that only the photoelectron spectra and lifetimes of the excited states could be inferred from the experimental results of this work. The illustration of the order in which the single bonds form is chosen based upon previous work on the PB reaction, as discussed on page 92

Table 8.3 Excited-state life times of GEM-VF and PARA-VF extracted through global fits of the time-resolved photoelectron spectra shown in Fig. 8.6

	S_3 (fs)	S_2 (fs)	S_1 (ps)
GEM-VF, $\lambda_p = 256$ nm	50	110	1.8
GEM-VF, $\lambda_p = 320$ nm	–	110	1.8
PARA-VF, $\lambda_p = 315$ nm	–	130	1.7

The corresponding DASs are shown in Fig. 8.7

photocycloaddition reaction following excitation of the S_3 state; it just decays to populate the lower lying states and eventually ends up in the triplet state manifold, as described above.

Finally, it is worth noting that the measured lifetimes of the S_2 and S_1 states in GEM-VF are close to identical in the $\lambda_p = 320$ nm and $\lambda_p = 256$ nm experiments. Interestingly, this means that the transition from S_1 to S_0 is not influenced by vibrational energy content to an extent that IC can compete with ISC, even though the reactive S_1/S_0 CI is energetically available. Following a Landau–Zener approach, one could expect the rate of $S_1 \rightarrow S_0$ population transfer by IC to increase with increasing vibrational energy content, since then the speed of the nuclei will increase. But as discussed previously (Sect. 2.1.4, page 11), it is not that simple; only movement along the branching space coordinates increases the rate of IC at a CI, and if the CI is sloped increased speed along the seam space coordinates can even decrease the rate of IC. Unfortunately, it cannot be assessed whether the CI corresponding to PB reaction in GEM-VF is sloped, since information about the topography of the PESs in the branching space is not available. What can be concluded, though, is that the

increased speed of the nuclei does not increase the rate of IC to an extent that allows it to efficiently compete with ISC.

8.4 Conclusion

With the aim of studying the excited-state dynamics of the Paternò-Büchi (PB) photocycloaddition between a formyl and a vinyl group we have performed TRPES experiments on a model system in which the two functional groups are connected to the [2.2]paracyclophane molecular scaffold in pseudo-*gem*-vinylformyl[2.2]paracyclophane (GEM-VF). Reference experiments on the pseudo-*para* isomer of GEM-VF (PARA-VF), in which the functional groups cannot react, have been conducted to study the influence of the paracyclophane scaffold on the lifetimes of the excited states. The measured singlet state lifetimes in GEM-VF and PARA-VF are nearly identical: the $S_2(\pi, \pi^*)$ state decays in $\sim$100 fs and the $S_1(n, \pi^*)$ state decays to the triplet state manifold in 1.7–1.8 ps. This leads to the conclusion that ISC competes efficiently with singlet state reaction, such that in GEM-VF the excited-state part of the PB reaction, formation of the O–C bond, takes place in the triplet state. The creation of the C–C bond leading to ring-closure and oxetane formation in the S_0 state has to be preceded by ISC, meaning that the time scale of the second part of the PB reaction in GEM-VF exceeds the range accessible in our experiments.

Note that, as opposed to the experiment on GEM-V (Chap. 7), we do not observe conformer-specific dynamics in this experiment. The reason is that both the anti-anti and anti-syn conformer end up in the triplet state manifold in which the formation of the O–C bond occurs. Since the lifetime of the triplet state ($\sim$1 ns) is long compared to the time scale of conformational change ($\sim$10 ps in GEM-V), the experiment cannot distinguish whether the formation of the O–C bond occurs immediately after ISC (in the anti-anti conformer) or is preceded by a conformational change (in the anti-syn conformer).

The most important conclusion to be drawn from this experiment is that the ISC rate exceeds the rate of singlet state reaction, such that the excited-state part of the PB reaction takes place in the triplet state manifold. This was already known to be the case in true bimolecular PB reactions between aromatic carbonyl compounds and alkenes in solution, in which the rate of ISC exceeds the rate of bimolecular collision controlled by diffusion. But it is interesting to realize that the reaction still occurs in the triplet state when the carbonyl and vinyl groups are in immediate vicinity already at the moment of excitation. The finding that ISC competes so efficiently with IC to the ground state can be speculated to be a general property of (aromatic) carbonyl compounds, in the sense that when interpreting results from fs time-resolved experiments on such compounds ISC should be taken into account more often.

References

1. Paterno, E., Chiefi, G.: Gazz. Chim. Ital. **39**, 341–361 (1909)
2. Büchi, G., Inman, C.G., Lipinsky, E.S.: J. Am. Chem. Soc. **76**, 4327–4331 (1954)
3. Griesbeck, A.G.: Oxetane formation: Intermolecular additions. In: Horspool, W. M., Song, P.-S., (eds.) CRC Handbook of Organic Photochemistry and Photobiology, Chap. 43, pp. 522–531. CRC Press Inc., Boca Raton (1995)
4. Bach, T.: Synthesis **5**, 683–703 (1998)
5. Abe, M.: J. Chin. Chem. Soc. **55**, 479–486 (2008)
6. Hoffmann, N.: Chem. Rev. **108**, 1052–1103 (2008)
7. Yang, N.-C., Loeschen, R.L., Mitchell, D.: J. Am. Chem. Soc. **89**, 5465–5466 (1967)
8. Zimmerman, H.E.: Angew. Chem. Int. Ed. Engl. **8**, 1–11 (1969)
9. Freilich, S.C., Peters, K.S.: J. Am. Chem. Soc. **103**, 6255–6257 (1981)
10. Freilich, S.C., Peters, K.S.: J. Am. Chem. Soc. **107**, 3819–3822 (1985)
11. Palmer, I.J., Ragazos, I.N., Bernardi, F., Olivucci, M., Robb, M.A.: J. Am. Chem. Soc. **116**, 2121–2132 (1994)
12. Kutateladze, A.G.: J. Am. Chem. Soc. **123**, 9279–9282 (2001)
13. Griesbeck, A.G., Mauder, H., Stadtmueller, S.: Acc. Chem. Res. **27**, 70–75 (1994)
14. Griesbeck, A.G., Abe, M., Bondock, S.: Acc. Chem. Res. **37**, 919–928 (2004)
15. Lee, S.-H.: J. Chem. Phys. **131**, 224309 (2009)
16. Scala, A.A., Diau, E.W.-G., Kim, Z.H., Zewail, A.H.: J. Chem. Phys. **108**, 7933–7936 (1998)
17. Gilbert, A., Baggott, J.: Essentials of Molecular Photochemistry. Blackwell Scientific Publications, Oxford (1991)
18. Turro, N.J., Ramamurthy, V., Scaiano, J.C.: Modern Molecular Photochemistry of Organic Molecules. University Science Books, Sausalito (2010)
19. Ramamurthy, V., Rao, B.N., Rao, V.P.: Solution photochemistry of thioketones. In: Horspool, W.M., Song, P.-S., (eds.) CRC Handbook of Organic Photochemistry and Photobiology, Chap. 63, pp. 775–789. CRC Press Inc., Boca Raton (1995)
20. Yang, Z., Heilbronner, E., Hopf, H., Ehrhardt, S., Hentschel, S.: J. Phys. Chem. **92**, 914–917 (1988)
21. Schon, C., Roth, W., Fischer, I., Pfister, J., Kaiser, C., Fink, R.F., Engels, B.: Phys. Chem. Chem. Phys. **12**, 9339–9346 (2010)
22. Schon, C., Roth, W., Fischer, I., Pfister, J., Fink, R.F., Engels, B.: Phys. Chem. Chem. Phys. **13**, 11076–11082 (2011)

Chapter 9
Probing Structural Dynamics by Interaction Between Chromophores

This chapter deals with the experimental results published in Ref. IV in which structural dynamics in the radical cation of 1,3-dibromopropane (DBP) was probed by exploiting the interaction between the bromine atoms. As such, this experiment illustrates a simpler, although not as general, way of probing conformational changes by interaction between chromophores than more involved techniques as for example 2D-IR. The experimental technique employed is time-resolved ion photofragmentation (TRPF) spectroscopy. Strictly speaking, this technique does not fall within the field of time-resolved photoionization and therefore the first section is devoted to a review of the pump probe scheme of TRPF. This is followed by a motivation of the experiment on DBP and a discussion of the obtained results. The experiments were performed using the Copenhagen setup (Sect. 6.1, page 65).

9.1 Time-Resolved Ion Photofragmentation Spectroscopy

Most gas phase femtosecond time-resolved studies published to date deal with molecular dynamics of neutrals and anions, and work on ultrafast dynamics of cations is rather limited [1–10]. In the latter experiments the pump pulse generates the cation by multiphoton ionization and absorption of the probe pulse induces increased fragmentation of the molecular ion, a scheme referred to as TRPF by Ho et al. [1]. Expressed in the general framework of Fig. 2.7 on page 18 the final state $\left|\Psi_f\right\rangle$ of a TRPF experiment is a (typically electronically) excited state of the cation. As such, TRPF experiments bear a large resemblance to transient absorption spectroscopy, except that in TRPF absorption is measured only indirectly through increased fragmentation of the ion. TRPF suffers from the same limitation as transient absorption experiments, namely that some electronic and/or nuclear configurations of the molecule can be dark to the probe, due to a forbidden optical transition to the final state.

An intriguing aspect of the TRPF experiment is how to perceive the wave packet $|\Psi(t)\rangle$ created in the cation state. The issue is illustrated in Fig. 9.1; the

R. Y. Brogaard, *Molecular Conformation and Organic Photochemistry*,
Springer Theses, DOI: 10.1007/978-3-642-29381-8_9,
© Springer-Verlag Berlin Heidelberg 2012

photoionization process induced by the pump pulse can populate more eigenstates of the cation than those contained within the coherent bandwidth of the laser pulse. Thus, it is not immediately clear how to extend the wave packet picture developed for neutral states to describe the case of a wave packet consisting of states in the ionization continuum. The theoretical framework of nuclear wave packets previously presented (Eq. 4.17, page 48) can shed some light on the issue. In that picture the pump pulse creates a series of nuclear wave packets $|\chi_{FE}(t)\rangle$ in the electronic state F of the cation (assuming F is the only state populated), corresponding to different kinetic energies E of the photoelectron. This can be envisioned as using a series of pump pulses with different center wavelengths, each creating their own wave packet, $|\Psi_E(t)\rangle = |\Phi_F\rangle\,|\chi_{FE}\rangle$. Figure 9.1 illustrates two such wave packets; corresponding to zero kinetic energy (red states, $|\Psi_0(t)\rangle$) and a finite kinetic energy of the photoelectron (green states, $|\Psi_E(t)\rangle$). Hence, in that picture a TRPF experiment probes not only one but several (possibly interfering) wave packets. In the following we will however ignore this complication and assume the cation wave packet to behave like a wave packet composed of neutral excited states.

Applying the simplified picture of the cation wave packet, Fig. 9.2 illustrates how molecular dynamics can be probed by TRPF analogously to the description of the TRPES experiment (Sect. 3.2, page 24). When the wave packet passes a region of the PES where the (linear or nonlinear) absorption cross section at the probing wavelength increases, sometimes called a 'dynamic resonance' [4, 6], absorption will lead to increased fragmentation of the molecular ion. Such increased fragmentation is expressed in the time-resolved mass spectrum of the cation which therefore is key to any TRPF experiment. The fragmentation can happen either directly, if the final state is dissociative, or in a statistical process as a consequence of excess internal energy. The positions of the dynamic resonances depend on the topography of the PES and the final state. As in any pump probe experiment the latter works as a template that, by changing the center wavelength of the probe pulse, can be tailored to probe different parts of the wave packet trajectories. The challenge is that in general very little is known about the excited states of the cation, often making the choice of probing wavelength somewhat arbitrary. In the present case the situation was different, since our choice of wavelength was guided by earlier experiments performed on DBP by Kötting et al. [11]. In fact, those experiments intrigued us to conduct the experiments described here. The reason was the fundamental problem of TRMS, namely that a fragment ion does not necessarily origin from ionization of the corresponding neutral. In other words, what was thought to be a TRMS experiment on a neutral species can turn out to be a TRPF experiment on a cation, which, as will be argued below, indeed seems to be the case in the experiment of Kötting et al. The most direct way of resolving the ambiguous origin of a fragment ion is by TRPES, since if the fragment ion is generated by ionization of a neutral species, there is a time-resolved photoelectron signal corresponding to the fragment ion signal. Thus, our TRPF experiments are supplemented with TRPES experiments and the absence of a time-resolved photoelectron signal is used to argue that the experiment does indeed probe dynamics in the cation.

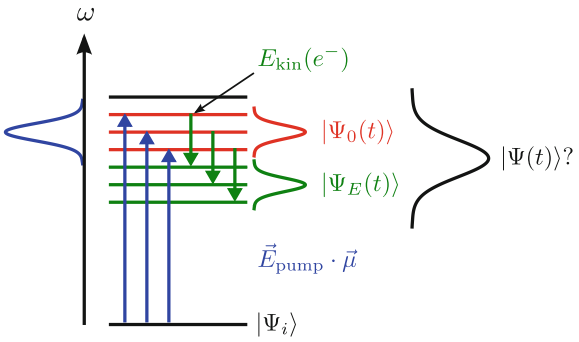

Fig. 9.1 Illustration of the problem of how to perceive a wave packet created by populating eigenstates of a cation in a photoionization process. Since the ejected electron can carry away kinetic energy (illustrated by the *green arrows*), the process can populate a spectrum of eigenstates (*red*, $E_{\mathrm{kin}} = 0$, and *green*, $E_{\mathrm{kin}} = E$) of the cation that is broader than the coherent bandwidth of the pump pulse (*blue*)

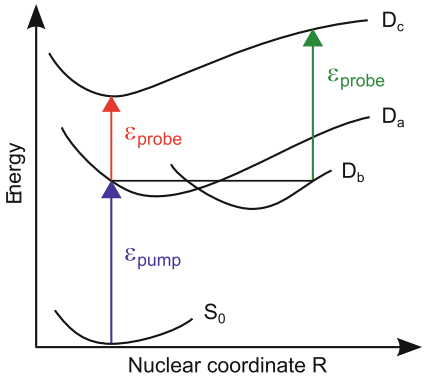

Fig. 9.2 Sketch illustrating how non-adiabatic dynamics in a cation can be probed using TRPF spectroscopy. The variables $\varepsilon_{\mathrm{pump}}$ and $\varepsilon_{\mathrm{probe}}$ indicate one or multiple photons of the pump and probe pulse, respectively. Excitation with the pump pulse prepares a wave packet initially resembling the D_a state. Motion along the nuclear coordinate R can induce a non-adiabatic transition to the D_b state. The choice of total probe photon energy (*red* or *green arrow*) determines the configuration(s) that can be probed, assuming the optical transition to D_c is allowed

9.2 Motivation

Excited-state dynamics in molecular cations is a promising research field, considering the myriad of examples of non-adiabatic effects giving rise to exciting ultrafast phenomena that have been observed in excited states of neutral molecules. The experiment presented in this chapter deals with the real-time probing of structural changes in an excited state of a molecular cation, taking place in the multichromophoric radical cation of DBP. Multichromophoric molecules (neutral as well as ionic) are

particularly well suited for investigations of structural dynamics, since the interaction between the chromophores can be used to probe the molecular conformation. The probing of conformational dynamics in DNA is a famous example (see e.g. Ref. [12] and references therein). As it turns out, compounds containing multiple chromophores are also well suited for studying excited-state cation dynamics. This is most clearly appreciated by employing the Koopmans picture in which the ionization process involves a single active electron and leaves the electronic configuration of the core unchanged. Consider the case in which the radical cation is created by the pump pulse in a REMPI process, in which the ionization occurs through an intermediate excited state in the neutral molecule. If this state involves an excitation of an electron from the HOMO, it will exhibit an ionization correlation to D_0. On the other hand, if the intermediate state is described by an excitation involving a chromophore that is not associated with the HOMO, it will exhibit an ionization correlation to an excited state D_x of the cation. This was illustrated in Fig. 3.1 on page 24. Formation of excited-state ions by REMPI involving intermediate excitations of different chromophores has been observed experimentally, e.g. in experiments on 2-Phenylethyl-*N,N*-dimethylamine [13]. At a wavelength of 400 nm the amine moiety is ionized, forming the cation in the ground state. When using 267 nm an electron is removed from the phenyl ring, forming the cation in an excited electronic state, because the ring is the chromophore involved in the intermediate state of the REMPI process [13].

As will be elaborated below, interaction between the two bromine atoms in DBP lifts the degeneracy of the lone pairs. This means that they can be considered different chromophores, making DBP well suited for investigations of excited-state cation dynamics. Using TRPF spectroscopy we aim to understand in detail the dynamics of the radical cation and unravel which photofragmentation channels are opened by absorption of the probe pulse.

9.3 Results and Discussion

9.3.1 Ground State Structural Aspects

Since structural dynamics is a major part of this work, we will start out by considering the four conformers of DBP shown in Fig. 9.3. The figure also shows the relative abundances of the conformers in a gas phase sample of DBP at 65°C (a temperature close to our experimental conditions) determined by electron diffraction [14]. The abundances reflect a stabilizing interaction between the bromine atoms competing with steric repulsion. The stabilizing interaction is greatly enhanced in the ground state radical cation, in which the gauche-gauche conformers dominate [15]. Since it was not possible to determine the distribution among the *g,g*-C_2 and the *g,g*-C_s conformer in the cation from the experimental results [15], we have calculated heats of formation (Fig. 9.3), which predict a stabilization of the *g,g*-C_s conformer by 18

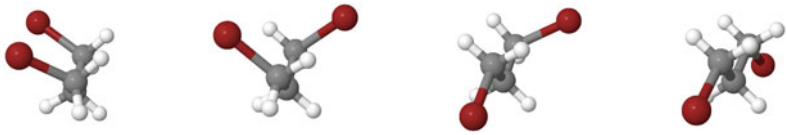

	g,g-C_s	*g,g*-C_2	*a,g*-C_1	*a,a*-C_{2v}
$\Delta H_f(S_0)$	0.2 (–)	0.0 (67 %)	0.0 (30 %)	0.1 (3 %)
$\Delta H_f(D_0)$	0.0	18	91	95

Fig. 9.3 Four conformers of DBP. Indicated below each conformer are the relative heats of formation in kJ/mol in the neutral (S_0) and cation ground state (D_0), as determined from calculations (G3//B3LYP [16]). The relative abundances of the conformers in S_0 (the *g,g*-C_s conformer was not present in detectable amounts) as determined from gas phase electron diffraction studies [14] are shown in parentheses

kJ/mol compared to the *g,g*-C_2 conformer. This shows that at equilibrium the *g,g*-C_s will be the only conformer present in a sample of ground state radical cations of DBP in the gas phase. Ab initio calculations reflect that ionization increases the interaction between the bromine atoms in the optimized geometry of *g,g*-C_2; the dihedral angle D(BrCCC) is 58° in S_0, whereas it is only 30° in D_0 [11]. This means that the removal of an electron can be expected to induce a conformational change in the resulting cation along a torsional vibration of the bromomethylene groups. In fact, the results discussed below do indeed show that this structural change is induced by ionization with the pump pulse and followed through induced fragmentation of the cation by the probe pulse.

9.3.2 Photoelectron Spectroscopy

Figure 9.4a shows the photoelectron spectrum obtained from photoionization of DBP using only the pump pulse (267 nm). When considering that the total energy of three photons of 267 nm is 13.9 eV and that the vertical IP of DBP is 10.1 eV [17], this should leave a maximum of $13.9 - 10.1 = 3.8$ eV as kinetic energy to the photoelectron. Closer inspection reveals a very weak onset of the photoelectron signal around 3.3 eV, agreeing reasonably well with the value of 3.8 eV, considering the background of photoelectrons generated by higher-order processes involving a larger number of photons. The spectrum is unstructured and extends over a wide range of energies, indicating that non-resonant ionization dominates. There is a maximum at 0.4 eV, though, which we assign to ionization of a (n,5d) Rydberg state excited resonantly during a three photon REMPI process, since the energy of two 267 nm photons matches the calculated excitation energy region of the (n,5d) Rydberg

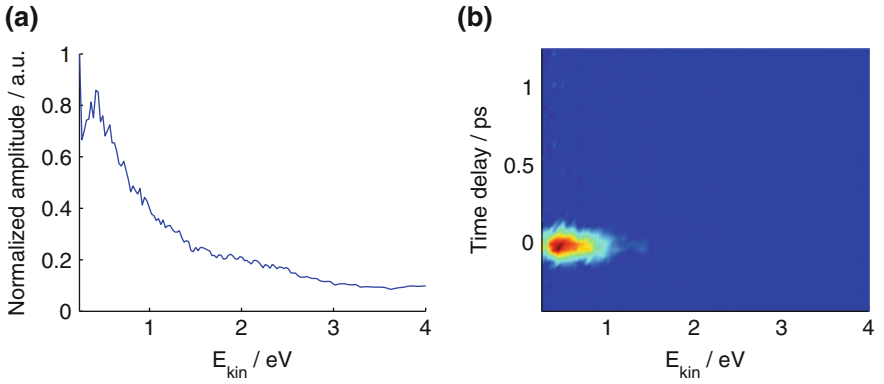

Fig. 9.4 **a** Photoelectron spectrum of DBP obtained from ionization with 267 nm only. **b** Time-resolved photoelectron spectrum (after subtraction of one-color signal) of DBP excited at $\lambda_p = 267$ nm and probed at $\lambda_e = 620$ nm

manifolds [11]. Considering the remarkable energy difference between this peak and the onset of the photoelectron spectrum, $3.3 - 0.4 = 2.9$ eV, we find it unlikely that the excess energy is deposited only in vibrational energy but take it to indicate that the Rydberg state is ionized to an excited electronic state of the cation. The assignment of the particular state is done based on discussions below.

The time-resolved photoelectron spectrum of DBP after subtraction of one-color signal is shown in Fig. 9.4b. The most important result is that the time-resolved signal and thus any dynamics involving neutral species is cross-correlation limited, which supports that the dynamics observed at longer delay times in the ion transients discussed below, is purely cation dynamics. As was the case for the one-color pump signal the time-resolved spectrum is broad and unstructured. It is noted that besides the pump–probe signal the spectrum will also contain contribution from a probe–pump signal, in which three photons of the probe pulse excites a repulsive (n, σ^*) state situated 6 eV above the ground state [11] that is ionized by the pump pulse. This process is also expected to give rise to a broad spectrum, due to the repulsive nature of the excited state. Thus, we do not find that further analysis aiming at disentangling the pump–probe from the probe–pump signal is justified.

9.3.3 Mass Spectrometry

The analysis of the TRMS data will focus on the temporal evolution of the ion signals corresponding to the parent and fragment ions shown in Fig. 9.5. Also shown in the figure are the components of the functions used to fit the signals. Besides the initial cross-correlation limited signal and a constant offset, the transients are composed of two components; an exponential rise/decay and a damped oscillation. The period

of the oscillation is 700 fs. The fits were made such that the damping time of the oscillation is the same as the exponential rise/decay time, which is 1.6 ps. We observe that there is a phase shift of π of the oscillation in the parent ion (202 amu) transient as compared to the oscillation in the 41 amu transient. As can be seen, the amplitude of the oscillatory signal is rather weak, which fits well with the TRPES results that indicate a low contribution from resonant processes giving rise to the dynamics.

In the following the two components of the experimental signals are interpreted, starting with the oscillatory part. We take the latter as a sign that the ionization induced by the pump pulse creates a wave packet in the cation state that spans a number of vibrational levels of a low frequency vibration, thereby starting a coherent motion along that coordinate. The vibrational period corresponds to a frequency of 48 cm^{-1}. The assignment of this vibration is facilitated by appreciating that, because of the ionic nature of Rydberg states, the presence of a Rydberg state with an associated PES that is practically parallel to that of the cation state excited in this experiment, is to be expected. With this is mind, we note that the frequency found in this experiment is remarkably close to the value of 45 cm^{-1} that was calculated for a torsional vibration of the bromomethylene groups in one of the (n,5p) Rydberg states of the *g,g*-C_2 conformer of DBP [11]. The nuclear motion along this coordinate, from here on called the bromotorsion, is illustrated in Fig. 9.6. QMD simulations predicted that excitation of that (n,5p) Rydberg state would lead to a wave packet moving along the bromotorsion coordinate [18], and it is very likely that this motion takes place in the cation state excited in this experiment. Indeed, high level ab initio calculations showed that the topography of the PES of the D_3 state along the bromotorsion coordinate is almost identical to the PES of the Rydberg state [11]. Thus, we assign the observed oscillatory behavior of the signal to the bromotorsion vibration initiated in the D_3 excited state of the cation. This is explained by the involvement of the Rydberg state as an intermediate state which, due to the strong ionization correlations of Rydberg states, preferentially populates D_3 in the ionization step of the REMPI process. The assignment is further supported when considering the photoelectron spectroscopy results that indicate the population of an excited state of the cation. Second, we have calculated the vibrational frequency (B3LYP/6-31+G(d)) of the bromotorsion vibration in the D_0 state to be 110 cm^{-1}, corresponding to a vibrational period of 300 fs, making it seem unlikely that the vibration takes place in D_0. As mentioned above, the reason that this motion can be monitored in the experiment is the presence of a dynamic resonance along the vibrational coordinate. The resonance induces an increased fragmentation of the ion due to absorption of (one or more photons of) the probe pulse. The position of the resonance is revealed from the phase of the oscillation in the transients; the maximum fragmentation is seen after one-half of the vibrational period. Thus, the resonance is situated close to the outer turning point of the vibrational coordinate. In this region of the PES, the bromine atoms are closer to each other (D(BrCCC) $\sim$ 30°) and interact in a way that enhances the probability of absorbing one or more photons of the probe pulse. This is sketched in Fig. 9.7. A similar phenomenon was observed in a TRPF experiment on the radical cation of CH_2I_2, in which a scissoring vibration of the iodine atoms could be monitored due to the fact that concerted elimination of

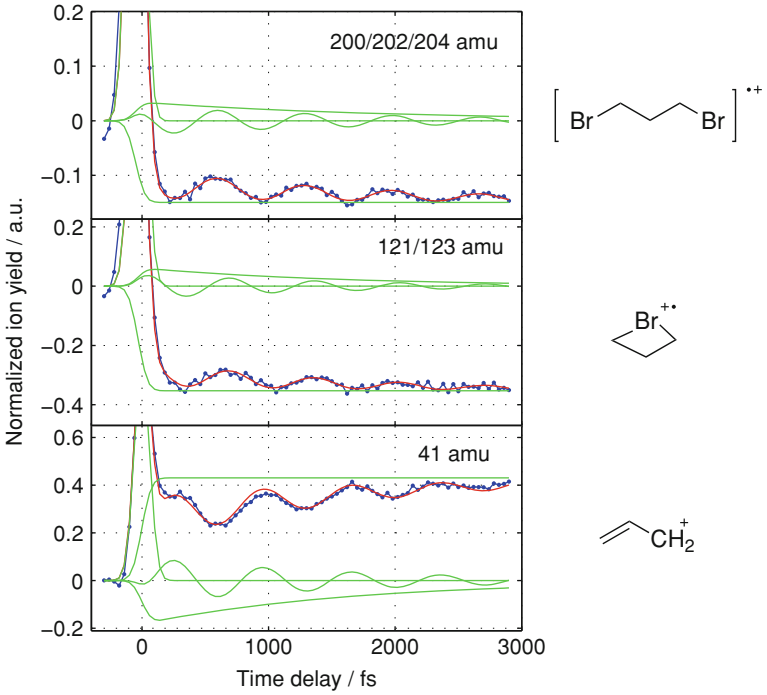

Fig. 9.5 Temporal evolution of selected signals (all normalized to a maximum amplitude of one) in the time-resolved mass spectrum of DBP excited at $\lambda_p = 267$ nm and probed at $\lambda_e = 620$ nm. Also shown in the figure are the components of the function used to fit the signals

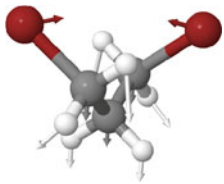

Fig. 9.6 Illustration of the nuclear motion in the bromotorsion vibration in the *g,g*-C_2 conformer of DBP

I_2^+ induced by the probe pulse preferentially occurred when the iodine atoms were close [5].

Turning to the second component in the fits of the transients, the decay/rise, we point out that since the damping time of the oscillations can be fitted to the same value as the decay/rise components, they are most likely related. We explain this by assigning the decay time to IC from the initially excited electronic state, D_3, to the ground state, D_0. The IC depopulates the D_3 state thereby damping the oscillations in the signal. In the D_0 state the minimum along the bromotorsion coordinate is located at $D(\mathrm{BrCCC}) = 30°$ as opposed to ~45° in D_3. Hence, IC from D_3 to D_0 will bring the bromine atoms closer together. This enhances the absorption cross section at the probing wavelength and thereby fragmentation, which is why the IC

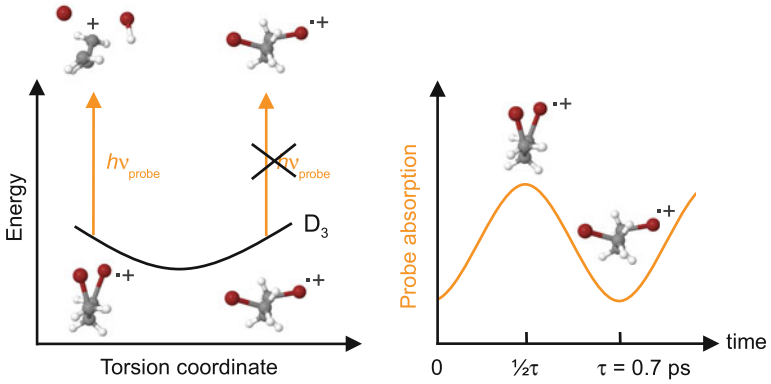

Fig. 9.7 Depiction of how the coherent vibration in the radical cation of DBP is followed in the TRPF experiment. The (linear or nonlinear) absorption cross section at the probing wavelength is modulated along the bromotorsion coordinate; when the bromine atoms are close the cross section is high, leading to an increased fragmentation of the parent ion (202 amu) to the fragment (41 amu). When the bromine atoms are further apart, the cross section, and thereby the extent of fragmentation, is lower

is seen as a rise in 41 amu and a corresponding decay in 202/121 amu. It is stressed that the IC to D_0 takes place in the *g,g*-C_2 conformation. This can be appreciated by considering that the barrier for the conformational change from *g,g*-C_2 to *g,g*-C_s in D_0 is 54 kJ/mol. The fact that the bromine atoms are closer in D_0 than in D_3, illustrates that the repulsion between them is larger in D_3, and therefore the barrier for conformational change is expected to be at least as high in D_3 as calculated for D_0. This means that when exciting the D_3 state the barrier for the conformational change cannot be crossed due to insufficient energy. Thus, IC from D_3 to D_0 has to take place in geometries similar to the *g,g*-C_2 conformation. Following IC, it is likely that the conformational change from *g,g*-C_s to *g,g*-C_2 takes place, but it will compete with the cleavage of the C–Br bond and both processes will be statistical in nature.

9.3.4 The Unifying Picture

Summing up the above, our interpretation of the results is as follows: the pump ionizes the molecule populating the D_3 excited state of the cation and initiating a coherent torsional vibration of the bromomethylene groups. The dephasing of the coherent motion is a result of the D_3 state population decaying by IC to the D_0 state. This scenario is sketched in Fig. 9.8. We note that our experimental data are very similar to those obtained by Kötting et al. on the same molecule [11], and therefore it seems likely that what they observed was indeed dynamics in the cation. It is important to keep in mind that while we used a probing wavelength that is almost identical to what

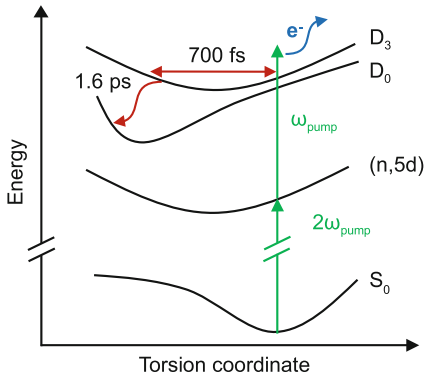

Fig. 9.8 Illustration of the molecular dynamics initiated in the D_3 excited state of the radical cation when DBP is ionized by the pump pulse (267 nm) through an intermediate (n,5d) Rydberg state

Kötting et al. used (620 and 615 nm, respectively), the center wavelengths of the pump pulses are quite different (267 and 308 nm, respectively). What both experiments have in common, though, is that the intermediate state involved in the REMPI process of the pump step is located within a Rydberg manifold; (n,5p) in their case and (n,5d) in our case. Since the PESs of the lowest excited states of the cation have very different topographies along the bromotorsion coordinate, depending on which lone pair the electron is removed from [11], the fact that the observed time scales are close to identical seems to imply that the D_3 state is populated in both experiments. This further implies that the intermediate Rydberg states involved in the REMPI process, have the same configuration of the ionic core, i.e. involves an excitation of an electron from the same lone pair. This might seem strangely coincidental, considering that the intermediate states are located within Rydberg manifolds of $4 \times 3 = 12$ (n,5p) and $4 \times 5 = 20$ (n,5d) energetically closely lying states, respectively. We believe that it is a consequence of Franck-Condon overlap; as shown in calculations by Kötting et al. the Rydberg PESs along the bromotorsion coordinate are almost identical to the corresponding (excited) states of the cation [11]. Thus, even though they are energetically close in the Franck-Condon region, their overlap with the vibrational wavefunction of the ground state will be very different and Franck-Condon factors will favour the same Rydberg manifold in both experiments, i.e. the set of states created by exciting the same lone pair electron into one of the three 5p and five 5d Rydberg orbitals, respectively. Thus, it seems that the excited-state dynamics in the cation of DBP is of more general character than appreciated at first sight. We predict that one would observe the same dynamics in an experiment in which the REMPI process of the pump step involves an (n,5s) Rydberg state as an intermediate state. In fact, a REMPI process involving any intermediate state that has a strong ionization correlation to the D_3 state will initiate the same cation dynamics.

9.4 Conclusion

This chapter describes time-resolved ion photofragmentation experiments on the multichromophoric radical cation of 1,3-dibromopropane (DBP), in which the interaction between the bromine atoms was exploited to probe the dynamics. By absorption of three photons of the pump pulse, the molecule is ionized through an intermediate (n,5d) Rydberg state. The strong ionization correlation of the Rydberg state means that the cation is formed in the excited electronic state D_3. The removal of an electron increases the interaction between the bromine atoms, and initiates a coherent torsional vibration in the D_3 state of the bromomethylene groups with a period of 700 fs. The D_3 state decays by IC to the D_0 state in 1.6 ps.

Finally, we emphasize that the property that makes DBP so well suited for investigations of structural and excited-state dynamics in the radical cation is the proximity of the two bromine atoms. The interaction between these two chromophores is crucial for probing the dynamics, demonstrating the applicability of a concept, that we believe can be used in a wide range of systems. Based on this, we anticipate structural and excited-state cation dynamics to occur in multichromophoric molecules in which ionization enhances an interaction between two chromophores that is already present in the neutral molecule, a criteria that can be used for choosing potential candidates for future experiments.

References

1. Ho, J.-W., Chen, W.-K., Cheng, P.-Y.: J. Chem. Phys. **131**, 134308 (2009)
2. Baumert, T., Röttgermann, C., Rothenfusser, C., Thalweiser, R., Weiss, V., Gerber, G.: Phys. Rev. Lett. **69**, 1512–1515 (1992)
3. Cardoza, D., Pearson, B.J., Baertschy, M., Weinacht, T.: J. Photochem. Photobiol. A **180**, 277–281 (2006)
4. Cardoza, D., Pearson, B.J., Weinacht, T.: J. Chem. Phys. **126**, 084308 (2007)
5. Geissler, D., Pearson, B.J., Weinacht, T.: J. Chem. Phys. **127**, 204305 (2007)
6. Pearson, B.J., Nichols, S.R., Weinacht, T.: J. Chem. Phys. **127**, 131101 (2007)
7. Loh, Z.-H., Leone, S.R.: J. Chem. Phys. **128**, 204302 (2008)
8. Yazawa, H., Shioyama, T., Hashimoto, H., Kannari, F., Itakura, R., Yamanouchi, K.: Appl. Phys. B Lasers Opt. **98**, 275–282 (2010)
9. Rosenberg, M., Minitti, M.P., Rusteika, N., Bisgaard, C.Z., Deb, S., Weber, P.M., Sølling, T.I.: J. Phys. Chem. A **114**, 7021–7025 (2010)
10. Plenge, J., Wirsing, A., Wagner-Drebenstedt, I., Halfpap, I., Kieling, B., Wassermann, B., Ruhl, E.: Phys. Chem. Chem. Phys. **13**, 8705–8714 (2011)
11. Kötting, C., Diau, E.W.-G., Sølling, T.I., Zewail, A.H.: J. Phys. Chem. A **106**, 7530–7546 (2002)
12. Lakowicz, J.R.: Principles of Fluorescence Spectroscopy, 3rd edn. Klyuwer Academix, Dordrecht (2006)
13. Cheng, W., Kuthirummal, N., Gosselin, J.L., Sølling, T.I., Weinkauf, R., Weber, P.M.: J. Phys. Chem. A **109**, 1920–1925 (2005)
14. Farup, P.E., Stølevik, R.: Acta. Chem. Scand. A **28a**, 680–692 (1974)
15. Hasegawa, A., Symons, M.C.R., Shiotani, M.: J. Chem. Soc. Perkin Trans. **2**, 657–665 (1989)

16. Baboul, A.G., Curtiss, L.A., Redfern, P.C., Raghavachari, K.: J. Chem. Phys. **110**, 7650–7657 (1999)
17. NIST Chemistry WebBook, NIST Standard Reference Database Number 69. http://webbook.nist.gov/chemistry
18. Brogaard, R.Y., Møller, K.B., Sølling, T.I.: J. Phys. Chem. A **112**, 10481–10486 (2008)

Part IV
Conclusion

Chapter 10
Summarizing Discussion

For most chemists the concept of the ground state reaction path as being the minimum-energy path from reactants to products along the potential energy surface (PES) is an essential part of their educational upbringing. Induced by optical excitations, photochemical reactions involve excited-state PESs. Thus, when it was found that conical intersections (CIs) are the photochemical reaction funnels that mediate efficient population transfer back to the ground state leading to reaction, minimum-energy CIs where thought to be the key regions of the PESs. This is indeed the scenario in cases where the PESs are initially far from each other in energy, and large-amplitude motions are required to access a region of intersection between two PESs where efficient population transfer to the ground state, and thereby reaction, takes place. Our experiment on the [2+2]cycloaddition published in Ref. II investigated dynamics of that type. But as opposed to the ground state transition state that is unique, numerous CIs are connected in an intersection seam that can extend over a large region of the PES. Thus, in cases where this is true and/or the excited states are close in energy already in the Franck-Condon region, large-amplitude motion is not crucial for mediating electronic population transfer, and the molecule does not necessarily make use of the (minimum-energy) CI. We observed such a behaviour in experiments on substituted cycloheptatrienes (not presented in the thesis) [1].

The two quite different cases of photodynamics described above illustrate the complex interplay between large-amplitude motions and ultrafast reactivity in photochemical reactions. The aim of this project has been to shed light on this interplay through a series of experimental and computational investigations each providing their own little piece of insight. It is the intention of this chapter to try to fit in these pieces in the greater picture and provide guidelines for where to look for new ones.

The experiments in this project were performed on a beam of cold molecules in the gas phase, avoiding the complicating influence of solvent interactions. Ultrafast dynamics of these molecules was studied using the technique of time-resolved photoionization. In this scheme an ultrashort optical pulse excites the sample and a second time-delayed optical pulse probes the initiated dynamics by photoionization. Since any state and molecular structure can be ionized no configurations are dark to

R. Y. Brogaard, *Molecular Conformation and Organic Photochemistry*,
Springer Theses, DOI: 10.1007/978-3-642-29381-8_10,
© Springer-Verlag Berlin Heidelberg 2012

the probe, making the technique extremely versatile. The dynamics of the isolated molecules were studied by detecting the ions and electrons generated in the ionization process, using time-resolved mass spectrometry (TRMS) and photoelectron spectroscopy (TRPES).

Probing wave packet motion One of the most intriguing aspects of fs time-resolved experiments is the ability to probe nuclear motion in real time through wave packet trajectories. In spectroscopy it is not the positions but the transient quantum state that is probed, and relating this state to nuclear positions can be a challenging task. Therefore a major effort was focused into understanding the relation between the experimental signal and the motion of the excited-state wave packet, mainly employing a theoretical approach. These efforts were substantiated in quantum dynamics simulations of time-resolved photoionization signals probing excited-state dynamics of acetone. The important outcome of these simulations was that the experimentally observed decay of a TRPES signal was not due to transfer of electronic population. On the contrary the decay reflected the wave packet moving out of the Franck-Condon region in a pyramidalization motion. Similar behaviour has been observed in other studies and stresses that the pursue of a close relation between theory and experiment is of utmost importance when interpreting data of TRMS and TRPES experiments.

In the acetone experiment it was only possible to follow the wave packet leaving the Franck-Condon region and subsequent motion in the pyramidalization coordinate was dark to the probe, complicating the interpretation of the experimental signal. The thesis also presented a time-resolved ion photofragmentation (TRPF) experiment in which the wave packet trajectory along a large-amplitude nuclear motion in an excited state of the radical cation of 1,3-dibromopropane was followed. In that case the relation between wave packet motion and experimental signal was easier to derive, as the vibration could be followed for several periods, making it possible to derive a vibrational frequency.

The influence of ground state conformation in photochemical reactions The major part of the experimental efforts were spent in the general quest to elucidate bimolecular photochemical reaction dynamics. Specifically, [2.2]paracyclophanes were used as molecular scaffolds onto which the reacting pair of functional groups was connected. In one experiment a [2+2]cycloaddition between two ethylene units was studied. The conclusion that fast reaction was observed only when the functional groups were situated in a reactive conformation already before light absorption, is in complete agreement with studies of the [2+2]cycloaddition leading to the mutagenic dimerization of adjacent thymine bases in DNA performed by Schreier et al. [2]. These experiments illustrate the importance of ground state conformation in photochemical reactions, and in fact it is the ground state conformation that protects DNA from this particular photodamage in the sense that reactive conformations of the bases are quite infrequent in the ground state [2].

Importance of triplet states in ultrafast photodynamics Proximity of the reacting units was also achieved in the study of the Paternò-Büchi reaction between a formyl and a vinyl group connected to the [2.2]paracyclophane scaffold. Our TRPES study

was the first fs time-resolved study of the reaction and showed that although the reaction partners were in close proximity already at light absorption, the singlet state reaction was very efficiently outcompeted by inter-system crossing. Thus, the Paternò-Büchi reaction primarily took place in the triplet manifold.

10.1 Future Research

It is my hope that the findings of this project will bring us one step further on the road toward the ultimate goal of obtaining a general understanding of what dynamics to expect from a given molecule, based on electronic characteristics, molecular geometry and ground-state vs. excited-state equilibrium conformation. In this context the premier purpose is to propose directions and pieces of advice for future research, based on the experiences of this project. This section will chart a few such directions and highlight a recent conceptual development by the Stolow group that I find particularly important.

The dynamophore Recently, Schalk et al. [3] introduced a significant extension of the conceptual framework of photochemical reaction dynamics; the *dynamophore*. Analogously to the concept of a chromophore designating the localized part of a molecule absorbing light, the dynamophore describes the part of the molecule involved in the excited-state dynamics initiated by light absorption. Ongoing research is focused on the characterization of a number of dynamophores, providing a concept that promises to be just as essential and intuitive in the comprehension of (ultrafast) photochemical dynamics as the notion of functional groups is to organic chemistry.

The pursue of a closer relation between theory and experiment The findings from this project and other works in the field stress that simulations of the signals are crucial to comprehend and make even qualitatively correct interpretations of results from time-resolved photoionization experiments. The theoretical field has now advanced to a point where it is possible to simulate such time-resolved signals energy- and even angle-resolved. But simpler approaches like the one presented in this project are also capable of providing valuable information while being more accessible to the experimentalist, and should therefore be pursued in connection to every experiment.

Bimolecular photochemical reaction dynamics The [2.2]paracyclophane turned out to be a useful scaffold on which pseudobimolecular photochemical reactions can be studied by attaching a functional group to each of the two benzene rings. Thanks to the synthetic skills of the Hopf group in Braunschweig the list of reactions that potentially can be studied this way is long, and due to the practical experience on sample handling obtained in this project future TRPES experiments can be performed almost routinely. An important experience of this project is that the products of the reactions were not detected in the TRPES experiments. Thus, future research along this direction will benefit greatly from time-resolved IR experiments in which the

products and bond formations can be unambiguously detected through characteristic bands in the IR spectrum.

In a more ambitious perspective the molecular scaffold strategy is only a step on the way towards the ultimate goal of making fs time-resolved studies of bimolecular photochemical reactions. The molecular scaffold strategy does not provide the ideal picture in the sense that the scaffold imposes forces on the reactants that would not be present in a prototype reaction between two bare reactants. In that perspective the strategy proposed by Scherer et al. [4] of prearranging the reactants in a van der Waals cluster is closer to the ideal situation, since van der Waals interactions are much weaker than covalent chemical bonds. Scherer et al. photodissociated one component of the van der Waals complex, causing a collision of the co-reagents in a well-defined orientation. It is not immediately obvious how to extend this approach to photochemical reactions, but one could envision a van der Waals component that by photodissociation generates an electronically excited species colliding with the other van der Waals component.

Real-time probing of structural dynamics by interaction between chromophores The TRPF experiment on 1,3-dibromopropane exploited the structural dependence of the interaction between the bromine chromophores to probe the large-amplitude motion, an approach we believe can be extended to other molecules, neutrals as well as ions, as a way of probing structural dynamics. Thus, we just initiated a project investigating the photodissociation of 1,2-dithiane

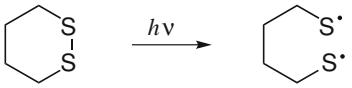

with the aim of mapping out the ring opening process through the interaction between the sulfur atoms.

References

1. Schalk, O., Boguslavskiy, A.E., Schuurman, M., Stolow, A., Brogaard, R.Y., Unterreiner, A.-N., Wrona-Piotrowicz, A., Werstiuk, N.H.: 2011, in preparation
2. Schreier, W.J., Schrader, T.E., Koller, F.O., Gilch, P., Crespo-Hernández, C.E., Swaminathan, V.N., Carell, T., Zinth, W., Kohler, B.: Science **315**, 625–629 (2007)
3. Schalk, O., Boguslavskiy, A.E., Stolow, A., Schuurman, M.S.: J. Am. Chem. Soc. **133**, 16451–16458 (2011)
4. Scherer, N.F., Sipes, C., Bernstein, R.B., Zewail, A.H.: J. Chem. Phys. **92**, 5239–5259 (1990)

Index

R. Y. Brogaard, *Molecular Conformation and Organic Photochemistry*, Springer Theses, DOI: 10.1007/978-3-642-29381-8,

© Springer-Verlag Berlin Heidelberg 2012